EPFL

Thèse n° 8578

Robotic manipulation to investigate the physical principles of biological self-organization

Présentée le 20 mai 2022

Faculté des sciences et techniques de l'ingénieur
Laboratoire de Systèmes MicroBioRobotiques
Programme doctoral en microsystèmes et microélectronique

pour l'obtention du grade de Docteur ès Sciences

par

Fazil Emre USLU

Acceptée sur proposition du jury

Prof. H. Shea, président du jury
Prof. M. S. Sakar, directeur de thèse
Prof. S. Hauert, rapporteuse
Prof. D. Cappelleri, rapporteur
Prof. S. Schurle-Finke, rapporteuse

École polytechnique fédérale de Lausanne

2022

An unexamined life is not worth living.

— Socrates

Science is the genuine guide in life.

— Mustafa Kemal Atatürk

Acknowledgements

I feel extremely lucky to had **Prof. Mahmut Selman Sakar** as my supervisor. He is a pure science-passionate, and always open to any discussion about research ideas or technical challenges and help, in case I needed. He helped me to intellectually evolve by discussions and sharing the latest scientific news. He continuously supported me in any stage of my studies. The support was not only scientific but also personal if I needed. I would like to express my gratitude to my collaborators. I collaborated with **Prof. Brendon Baker**, **Prof. Nikolaos Bouklas** and **Dr. Christopher Davidson** to realize the magnetic micro actuator technology. They supplied any support or material I needed immediately, and helped me to improve our research with nurturing discussion. For my second project, it would be impossible to explore how the ant self-organize to transport broods without the collaboration with **Dr. Sean McGregor**. He is not only biologist but also he has amazing technical skills. He is super hard-working, great communicator, and excellent teammate. I express my gratitude to **Dr. Erik Mailand** for his contribution to my work. He is my friend as well, with whom I had great time to do sport, talk about life and philosophy.

I express my gratitude to jury members of my thesis, **Prof. Herbert Shea**, **Prof. Simone Schuerle-Finke**, **Prof. Sabine Hauert**, and **Prof. David Cappelleri**. Their valuable questions and feedback helped me tremendously to improve my thesis. I would like to thank my lab mates and friends for their invaluable support in terms of research and personal life. **Dr. Murat Kaynak** was my roommate and close friend. We had great times and he supported me in all aspects of life, which is invaluable and not going to be forgotten. I thank **Dr. Raquel Parreira** for her academic support and accompanying for doing sport and dancing. I would like to thank **Dr. Lucio Pancaldi** for his academic support and joining me to steal other lab

mate' burgers at Zoo Burger retreats. I express my gratitude to **Ece Ozelci** for her friendship, sharing good music and patience when I had to overrun her microscope reservation. I would like to express my gratitude to **Matthias Ruegg** for his academic and personal support. I thank **Ioanna Paniara**, **Dr. Amit Dolev**, **Laura Hermans** and **Sourabh Monnappa** for their support.

I would like to thank **Dr. Muhammed Fatih Ballı** and **Dr. Recep Gül** for their support in every aspect of life, dinners and great talks on diverse topic. I especially thank them to let me realize how living is valuable and beautiful after they directed us to complete deadly hikes in the Alps. I cannot forget **Dr. Ballı** while courageously walking in 1 m of snow at the hillside of a mountain at 2042 m and **Dr. Gül** while trying to call rescue forces next to a huge rock under stormy weather at the mountain. I thank **Dr. Hüseyin Barış Atakan** for enjoyable lunches and his support. I thank **Ece Yıldız**, **Furkan Ayhan**, **Mustafa Kangül**, **Ömer Özdemir** and **Özge Uysal** for their friendship and enjoyable events.

I would like to thank my friends **Barış Özkaranfil**, **Çağan Ürküp**, **Kaan Telciler**, **Kemal Emrecan Şahin**, and **Ömer Kırnap** for their continuous support in any aspect, starting from bachelor years. Even though they were not living here, they were always with me via digital communication.

I am immensely lucky to have awesome parents and brother. I would like to express my infinite gratitude to **Şifa Uslu**, **Mustafa Uslu**, and **Muhammed Ali Uslu** for their continuous and unconditional support. Even though we were far during the Ph.D. period, I always felt them next to me, supporting me. I believe that a healthy and happy family life is an important factor for growing a successful kid. If I have achieved any bit of success until today, they are one of the main driver of this success.

Last but most importantly, I was honestly not imagining that I was about to live the most special times of my life during my Ph.D. period. First, I met with my love, **Laura Bonnafous**. She is a successful, strong and full-of-love woman. I tremendously enjoy anything I do with her, from a glass of wine at our balcony to going to travels, which we generally plan couple of days before going. She continuously and unconditionally support me in any aspect of our life. She is one of the main drivers of my success, if I could have achieved any. Then, we got our diamond, fıstığım, **Salome Nil Bonnafous** into our life. She is, of course, the cutest baby

of the world. Her existence and any little gesture of her is one of the most valuable features of my life. I am looking forward to happily live the rest of our life in the years ahead. Finally, I would like to send my love and gratitude to happy and always-hungry beauty, **Victoire**. We do not forget you. I miss our walks, eating and sleeping together.

Fazıl Emre Uslu

May 2022

Lausanne

Abstract

Self-organization is the spontaneous formation of ordered patterns and networks from a population of comparatively simple elements or individuals with no prior information on neither the formation process nor the final organization. While the construction of tissues and organs is driven by the collective action of many eukaryotic cells, at a higher scale, social insects govern massive colonies via cooperative group behavior. In biological self-organization, unlike inanimate matter, interaction rules of elements are not constant but generally evolve in time and space with a history-dependent fashion. Recent technological advances in molecular biology, genetics, microscopy, and quantitative analysis have made it possible to follow the development of tissues, organs, and entire embryos at the single-cell level with high temporal resolution. Automated video tracking systems based on identification labels allow tracking of all members in insect colonies to identify individual interactions and patterns of social organization. These studies have shown that individuals must allocate themselves to actions or tasks in a dynamic manner following simple rules that incorporate local stimuli received directly from the environment and from interactions with other individuals. Majority of the available platforms provide observation only and does not allow manipulation of conditions for probing the self-organizing systems. Application of spatiotemporally resolved physical stimuli to individuals will reveal a more complete understanding of biological self-organization.

In this thesis, I have developed robotic manipulation platforms along with computational models to investigate the principles of self-organization in biological systems. I have worked on two complimentary experimental models at different scales to prove the generality of my approach. The first robotic manipulation platform explores the transmission and transduction of mechanical signals within a connected fiber network, and associated cellular responses. I

developed a biocompatible magnetic microactuator and a magnetic control system to apply physiologically relevant traction forces to cells cultured on fibrous matrices. Along with the experimental platform, I have developed a finite element-modeling framework that simulates stresses on a digital copy of the fiber network. The second robotic manipulation platform controls the temperature on the nest floor of ant colonies. The system is integrated with a real-time tracking system that is capable of following interactions among hundreds of individuals. The ant colony is stimulated to transport their brood by changing the temperature of next floor in a spatially patterned way. We explored how ants processed thermal signals, coordinate transport of brood, and interacted with one another.

Key words: Self-organization, Robotics, Mechanobiology, Micromanipulation, Thermoregulation, Finite Element Modeling

Résumé

L'auto-organisation est la formation spontanée de modèles et de réseaux ordonnés à partir d'une population d'éléments relativement simples ou d'individus sans information préalable sur ni le processus de formation ni l'organisation finale. Alors que la construction des tissus et des organes est entraîné par l'action collective de nombreuses cellules eucaryotes, à plus grande échelle, des insectes sociaux gouvernent des colonies massives via un comportement de groupe coopératif. Dans l'auto-organisation biologique, contrairement à la matière inanimée, les règles d'interaction des éléments ne sont pas constantes mais évoluent généralement dans le temps et l'espace avec une mode dépendante de l'histoire. Les avancées technologiques récentes dans le domaine de biologie moléculaire, la génétique, la microscopie et l'analyse quantitative ont permis de suivre développement de tissus, d'organes et d'embryons entiers au niveau d'une seule cellule avec une haute résolution temporel. Des systèmes de suivi vidéo automatisés basés sur des étiquettes d'identification permettent de suivre tous les membres des colonies d'insectes pour identifier les interactions individuelles et les modèles d'organisation sociale. Ces études ont montré que les individus doivent se consacrer à des actions ou à des taches de manière dynamique en suivant des règles simples qui intègrent des stimules locaux reçus directement de l'environnement et des interactions avec d'autres individus. La majorité des plateformes actuellement disponible fournissent uniquement l'observation et ne permettent pas la manipulation des conditions de sondage les systèmes auto-organisés. L'application de stimules physiques résolus spatio-temporellement aux individus révéleront une compréhension plus complète de l'auto-organisation biologique.

Dans cette thèse, j'ai développé des plateformes de manipulation robotique ainsi que des modèles pour étudier les principes d'auto-organisation dans les systèmes biologiques. J'ai travaillé sur deux modèles expérimentaux complémentaires à différentes échelles pour prouver la généralité de mes approches. La première plateforme de manipulation robotique explore la transmission et la transduction des signaux mécaniques au sein d'un réseau de fibre connectées et des réponses cellulaires associées. Je développé un microactionneur magnétique biocompatible et un système de contrôle magnétique conçu pour appliquer des forces de traction physiologiquement pertinentes aux cellules cultivées sur des matrices fibreuses. Avec telle plateforme expérimentale, j'ai ainsi développé un cadre de modélisation par éléments finis qui simule les contraintes sur une représentation digitale du réseau fibreuse. La deuxième plateforme de manipulation robotique contrôle la température sur le sol du nid des colonies de fourmis. Le système est intégré à un système visuel de suivi capable de suivre les interactions entre des centaines d'individus à temps réel. La colonie de fourmis est stimulée pour transporter son couvain en changeant la température de la prochaine sol d'une manière spatialement modelée. Nous avons exploré comment les fourmis traitaient les signaux thermiques, coordonnaient le transport du couvain et interagissaient les uns avec les autres.

Mots clés : Auto-organisation, Robotique, Mécanobiologie, Micromanipulation, Thermorégulation, Modélisation éléments finis

Contents

List of Figures

List of Tables

1 Introduction

1.1 Problem Statement

Biological systems exhibit large-scale self-organized dynamics and structures which enable them to possess survival advantages and perform the functions of life. Self-organization is the spontaneous formation of ordered patterns and structures from a population of elements that have no or minimal patterns. Greek philosopher Aristotle wrote in Metaphysics "in the case of all things ... in which the totality is not, as it were, a mere heap, but the whole is something besides the parts, there is a cause ...". Emergence of patterns is also observed in non-living matter. For example, snowflakes and ripples self-form from water molecules and sand, respectively. However, living matter has unique features. Notably, in a biological system, individual agents are freed from the rigid constraints of thermodynamic equilibrium because their constituent elements are 'active', converting energy into force and motion to maintain the agent out of equilibrium. This property makes them context-dependent; i.e., they may behave differently depending on the resources, neighbors, or internal state. In addition, the behavior of living systems is influenced by not only the current conditions but also preceding events. Stigmergy is a mechanism of indirect coordination between agents through the environment. The principle is that the trace left in the environment by an individual action stimulates the performance of a succeeding action by the same or different agent. Thus, in biological self-

organization, interaction rules of elements are not constant but generally evolve in time and space with a history-dependent nature.

Self-organization in life sciences has been studied at multiple scales, from the assembly of intracellular protein networks to cells combining to create highly structured tissues to insect collective behavior (Figure 1.1). What these diverse systems hold in common is the proximate means by which they acquire order and structure. In all these systems, pattern at the global level emerges solely from interactions among lower-level components. Remarkably, even very complex structures result from the iteration of surprisingly simple behaviors performed by individuals relying on only local information. At the cellular level, structures with sophisticated features can emerge from simple starting points. For example, both eukaryotic embryos and prokaryotic biofilms arise from single founder cells. In both cases, development via cell division produces three-dimensional (3D) collections of cells encased in extracellular matrices (ECM). Despite a common origin, descendant cells in both systems differ in spatial positions, nutrient access, signaling gradients, and states of mechanical stress. At a larger scale, collective dynamics allow super-organisms to function in ways that a single organism cannot, by virtue of their emergent size, shape, physiology and behaviour. For example, ants link their bodies to form rafts to survive floods, assemble pulling chains to move food items, and form bivouacs and towers, as well as bridges and ladders to traverse rough terrain. European honeybee swarms form clusters that maintain a stable structure that handles both static gravity and dynamic shaking instantiated by wind and predators.

The study of the principles of biological self-organization is instrumental to understand nature and control natural processes towards medical solutions. Furthermore, this line of research inspires advancements in materials science, robotics, social sciences, environmental science, and computer science. Not surprisingly, researchers from various disciplines investigated the problem using empirical and theoretical models. One of the most extensively studied experimental model system is epithelia. Epithelial sheets exhibit complex dynamic behaviours that are not observed in single cells, neither can they be simply predicted from the observation of isolated cells. We now know that emergent mesoscale states of epithelial monolayers such

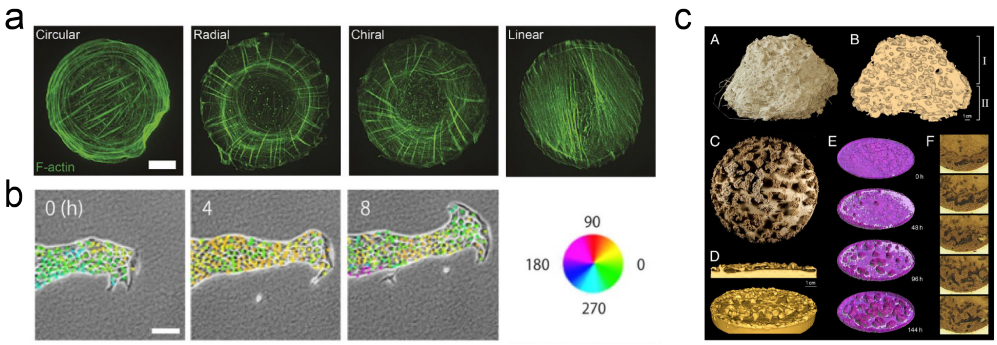

Figure 1.1 – Self-organization in nature. a) Actin fibers are reorganizing and different actin patterns emerge inside the cell cytoplasm [1]. Scale bar, 10 µm b) MDCK cells are collectively migrating. The colors are depicting the migration direction of each cell [2]. Scale bar, 100 µm. c) Stigmergic construction of ant nest is depicted. The evolution of the pillars inside the nest and 3D image reconstruction of evolution is presented [3].

as jamming, topological defects, and waves can be predicted by a set of physical quantities including force, density, shape, adhesion, and self-propulsion. Here, I would like to highlight the importance of technological advancements that made these discoveries possible as they are very relevant for the objectives of the thesis.

Microtechnology. Microfabricated substrates recapitulate physiologically relevant signals and architectures to accurately mimic tissue microenvironment. In the context of epithelial cell culture, cleanroom based subtractive manufacturing and soft lithographic techniques have been extensively used. For example, 2D substrates are patterned with adhesive or non-adhesive proteins using microcontact printing to control the geometry and confinement of epithelial layers. New boundaries are introduced using controlled removal of microfabricated obstructions or stamps. Finally, nanoscale or microscale topographical features and stiffness gradients are included using UV patterning, microfluidics, and dip-pen lithography.

Time-lapse imaging and traction force microscopy. Active dynamics and forces at the cell and tissue level can be measured by combining optical imaging and deformation of substrates with well-defined mechanical properties. Fully motorized microscopes allow continuous imaging of epithelial cells on engineered substrates. The synthetic substrate used to culture the cells can also act as a force sensor to measure the traction forces that cells exert on the

substrate. To this end, fiducial markers (i.e., fluorescent particles) are embedded inside linearly elastic gels or elastomers with well-characterized mechanical properties. Local deformations of the substrate with respect to the resting state can then be measured to quantify the force fields acting on the material. Moreover, tissue stress and traction forces are linked and by applying specific rheological models, intercellular stress in 2D epithelial sheets can be deduced from the same data.

Theoretical modelling. Agent-based models and continuum models have been widely used to understand the mechanics of epithelial dynamics. In agent-based models such as cellular Potts model or vertex model, the individual agents are explicitly simulated using geometric descriptors. Cell position and velocity, local cell–cell adhesion strength and cell shape serve as the parameters of the model. Continuum models capture bulk shape and movements of many cells based on a continuum description of elasticity and energy, and complement the calculations of the agent-based models.

As the research on epithelia has shown, the combination of these three pillars (i.e., microtechnology, quantitative imaging, and theoretical modeling) has the potential to unlock the mystery of biological self-organization. I postulate that there is a fourth pillar that has been missing in almost all of these studies: robot-assisted manipulation. While observing, quantifying, and modelling collective behavior within an engineered environment is essential to extract basic principles, controlled application of local stimuli would reveal additional information that is otherwise inaccessible. There are a number of single cell manipulation techniques that involve the use of optical tweezers, magnetic tweezers, and atomic force microscope (AFM). However, the application of local forces within a group of cells is a different challenge that requires novel technological solutions. With the same logic, the study of self-organization within insect colonies requires proper equipment that would allow continuous monitoring, a manipulation system that is capable of applying local stimuli without disrupting the order, and relevant models based on network theory. The emphasis is on robot-assisted manipulation because repeatability and precision are critical factors for the analysis of complex systems. A completely different collective state may emerge if a slightly different signal is applied.

1.2 General Objectives and Approach

The overall objective of this thesis is to introduce a methodology to generate and transmit physiologically relevant physical signals within a group of interacting biological agents in a well-controlled and continuously monitored environment. To this end, I developed two unique robotic platforms operating at two different size scales to (i) demonstrate the universality of the technological approach and (ii) investigate similarities and differences between organization principles. The physical stimulus must be chosen in a way that it can be seamlessly applied and removed, the characteristics of the signal are physiologically relevant, and the biological sensing mechanism is relatively well-studied. Notably, the physical signal must be isolated from any indirect effect, to avoid stimulating multiple sensory pathways. The system must be well-calibrated and engineered to stay stable over days despite continuous operation under physiological conditions (with regulated temperature and humidity).

The common features of the two platforms are:

- All the individual members of the collective are observable at all times.
- All agents are capable of detecting the applied signal.
- The signal is applied locally.
- Both short-term (seconds) and long-term (days to weeks) stimulation are feasible.
- Computational models aid the processing of the data.

It has been shown that cells have ion channel proteins such as Piezo1 (2021 Nobel Prize in Physiology or Medicine) and receptors such as integrins and cadherins that respond to mechanical loading. The field of mechanobiology has been growing rapidly, and a detailed understanding of the cellular mechanotransduction process has been emerging. The first system is built to ask the following scientific questions. What is the exact role of cellular traction forces on multicellular organization within extracellular matrices? Can forces applied by resident cells serve as communication signals? What are the specification of the forces that

the cells can perceive and process through matrix fibers (i.e., amplitude, duration, frequency, etc.)? Can we instruct cells to cluster or disperse by modulating the distribution of stress within the matrix? How does the transmission and cellular processing of mechanical loading depend on the mechanical properties and architecture of the matrix?

Ants are social insects that have been serving as an empirical model for research in the domains of social behavior and self-organization. They are equipped with sensors to detect changes in ambient temperature, and a number of metabolic and developmental processes are tightly regulated by ambient temperature. Changing the temperature on the next floor is non-invasive and does not interrupt physical organization of the nest. The second system is built to ask the following scientific questions. How do ants react to local temperature changes within their nests? Do they maintain social and spatial networks while reacting to spatiotemporal variations in temperature, and how? Would it be possible to re-wire the network architecture (i.e., reorganize the colony) through physical stimulation?

1.3 Organization of the Thesis

The thesis has two major parts. Chapters 2 and 4 summarize the technical context that is required to appreciate the novelty and impact of the platforms presented in Chapter 3 and 5. In Chapter 3, I introduce a robotic micromanipulation platform that is designed to apply traction forces to cells through an engineered synthetic ECM with tunable architecture and mechanics. To this end, a cell-sized magnetic microactuator is incorporated to an electrospun fibrous web on which cells can be cultured. Precise rotation of the microactuator by a custom-design magnetic control system imitates the matrix deformation instantiated by cellular contractility. A one-to-one digital replica of the actuated substrate calculates the dynamic stresses applied to the cells. The utility of the platform is showcased through several demonstrations including intracellular calcium signaling and cell migration analysis.

Chapter 5 presents the second robotic manipulation platform that is capable of generating spatially patterned thermal signals on the nest surface. The platform consists of Peltier

elements, power and control electronics, and a cooling system, all integrated with a tracking system. The tracking system visually monitors the ants through the transparent ceiling of the nest day and night. Ants carry robotic tags so that individual identity is preserved in the tracking data. We observed that ants would like to keep their brood at certain temperatures, and this preference could be used to initiate brood translocation events. The rest of chapter presents data on task allocation, communication, collective vs individual decision making, social and spatial organization, and redundancy in an ant colony. In Chapter 6, I discuss the implications of our original findings and present the future outlook for the methodology.

2 Background I - Mechanobiology of collective cell behaviours

Mammalian cells coordinate their state and action during multicellular organizational events such as morphogenesis and cancer progression by interacting with each other and the surrounding extracellular matrix. The interaction mechanisms are governed by mechanosensitive adhesion complexes at the cell–substrate interface and cell–cell junctions, which respond to but also further transmit physical signals. Recent studies have shown that the physical properties of the cellular environment, which include matrix stiffness, topography, geometry and the application of external forces, can alter tissue architecture and cell-generated forces. In the context of this thesis, the relevant studies can be placed in one of the two categories: (i) cells cultured on flat continuous substrates such as plastic dishes and deformable elastomers, and (ii) cells cultured on or inside fibrous substrates such as collagen gels and synthetic fiber networks. This distinction is important because force transmitted through a discrete fibrous network may propagate long-distances, cells show completely different phenotype and collective behaviors within fibrous gels, and fiber remodeling has the potential to serve as the organizing feature as information could be written on and read from the state of the matrix (e.g., fiber alignment, stiffening etc.). The last feature is related to the concept of stigmergy, an important aspect of biological self-organization.

2.1 Single cell force spectroscopy

Individual cells are the subunits of the multicellular tissue. As the interactions among subunits are the main driver of self-organization, it is crucial to identify the ways cells perceive, process, and respond to physical stimuli. Different manipulation techniques have been devised over the years to apply mechanical stimuli to individual cells at different scales. The specification is to imitate the forces cells experience within the tissue. First attempts to apply mechanical forces involved indenting adherent cells with glass capillaries [4]. Atomic force microscopy (AFM) probe serves as an advanced indentation tool that essentially does the same job with significantly higher position and sensing resolution [5].Micropipette aspiration is another technique commonly used to mechanically manipulate individual cell. Local pressure is controlled to apply pulling forces on the membrane [6]. The data that is collected using this

technique has played an important role to study cortical tension.

Magnetic manipulation is a wireless alternative to microindentation and aspiration techniques. Seminal work by Crick and Hughes showed the feasibility of introducing magnetic beads into the cytoplasm of living cells [7]. Actuation of encapsulated beads using permanent magnets or electromagnets leads to the application of internal forces. This method is used to measure the mechanical properties of single cells and mechanotransduction process [8], [9].Instead of plating cells on a flat substrate, they can be cultured on flexible pillars. Magnetized pillars provide a wireless method to apply local forces directly on focal adhesion complexes [10]. External magnetic field bends the pillars in a spatially controlled way, deforming the cells that are attached to those pillar in the process.

Optical manipulation is another way to wireless stimulate cells. Analogous to magnetic manipulation, beads with proper refractive indices can be trapped and manipulated by optical tweezers [11], [12]. More recently, Liu et al. devised a surface covered with nanoscale particles that consist of a thermoresponsive polymer and gold nanoparticles [13]. Cells adhere to those particles with their mechanosensitive receptor proteins. Application of near infrared light heats up the polymer and contraction of the polymer applies very localized mechanical loading to individual receptors. Similarly, actuatable substrates have been synthesized from thermoresponsive polymers and gold nanoparticles on which cells can be cultured and mechanically loaded [14].

2.2 Cell-cell interactions on flat continuous substrates

Cells cultured on rigid substrates cannot transmit forces to one another without making physical contact. Therefore, we do not expect mechanical communication to play a role in the social behavior of cells that do not touch each other. Fibroblast cells confronting each other on a culture dish retract their protrusions and change direction on contact. This phenomena, which is called 'contact inhibition' by Abercrombie more than 50 years ago [15], explains many features of the behaviour of fibroblasts both in tissue culture. Later work provided

examples of contact inhibition of locomotion with neural crest cells in vivo [16]. Vedel et al. demonstrated that the local cell density regulates speed, directionality, and displacement of individual fibroblast cells [17]. Notably, the complex collective dynamics could be captured by a relatively simple mathematical model based on experimentally identified cellular traffic rules (Figure 2.1a).

Seminal work has shown that cells feel and respond to the mechanical properties of their substrate by generating intracellular biochemical signals [18]. These signals control multiple aspects of cell behavior including migration and differentiation. Indeed, soft matrices that mimic brain are neurogenic, stiffer matrices that mimic muscle are myogenic, and comparatively rigid matrices that mimic collagenous bone prove osteogenic. A number of proteins and signaling pathways are involved in mechanotransduction including receptor proteins, cytoskeleton tension, transciption factors such as YAP/TAZ, and RhoGTPase activity. Cells have the ability to follow gradients of extracellular matrix stiffness, a type of directed migration called durotaxis. Stiffness gradients have been shown to drive collective migration of neural crest cells in Xenopus laevis embryos [19].

Certain cell types such as epithelial cells organize in sheets and clusters through tight junctions. With introduction of traction force microscopy, it has become possible to measure not only velocity and deformation fields but also tractions and intercellular stresses. Force mapping has unveiled phenomenological principles of cell organization such as the alignment of the cell body with the direction of maximum stress. This phenomenon, called plithotaxis, implies that cells organize in sheets so as to minimize intercellular shear stress [20]. Plithotaxis provides a mechanism for cells to migrate collectively in a preferred mechanical direction. Another emergent phenomenon in cell monolayers is their ability to propagate mechanical waves. In response to a sudden change in boundary conditions, the cells at the monolayer edge spreads and migrates towards the freely available substrate, whereas the trailing cells remain static. With time, every cell row becomes progressively engaged in collective motion following a wave of deformation and force generation. Recent work has shown that collective cell durotaxis emerges from long-range intercellular force transmission in epithelial monolayers [21].

The line of work that is methodologically very relevant to this thesis concerns with cardiac cells [22]. Cardiac cells cultured on a deformable substrate mechanically interact with each other where their contractions become synchronized. This coupling decreases with increasing distance between them and the substrate stiffness. Notably, an isolated cardiac cell can be trained to beat at a given frequency by mechanically stimulating the underlying substrate. In this demonstration, deformations were induced using an oscillatory mechanical probe that mimics the contractions generated by a beating cardiac cell (Figure 2.1b). We followed a similar methodology to actuate a fibrous substrate. However, instead of a tethered probe, we used an untethered magnetic microactuator. The reasons will be enlisted in the beginning of the next chapter.

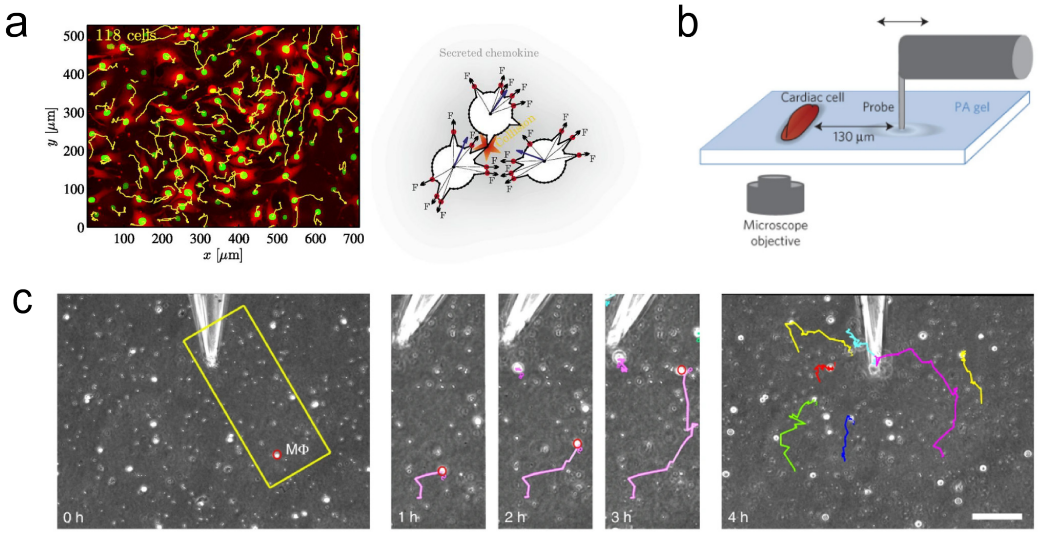

Figure 2.1 – Mechanical communication among cells. a) Collective motion of a group of fibroblasts on a culture plate. Yellow line shows the trajectories, while red and green represents the cytosol and the nucleus, respectively (Left). Dynamic and stochastic formation of pseudopodia is presented during collective motion as a schematic (Right). Figure adapted from [17]. b) Schematic showing the mechanical entrainment of a cardiac cell by deformation applied by a probe. Figure adapted from [22]. c) Local deformation of a collagen gel with a pipette attracts macrophages to the loaded area. The trajectories of macrophages are shown with colored lines. Figure adapted from [23]. Scale bar, 100 μm.

2.3 Cell-cell interactions within fibrous substrates

Extracellular matrix plays an important role in the transmission and storage of physical signals. Recent work has shown that forces applied by fibroblasts can be transmitted for long distances inside fibrous matrices and attract neighboring macrophages [23]. Application of tension using a pipette initiates this type of mechanical communication in a collagen gel (Figure 2.1c). Mesenchymal cells aggregate and form clusters by applying traction forces and remodeling the surrounding matrix. These microscale clusters act as actuators that collectively deform tissues to define macroscale shape [24]. Figure 2.2a shows an in vitro demonstration of this morphogenesis process. While the final 3D configuration is a result of the initial distribution of cells as actuators, the dynamic mechanical properties of the ECM also governs the self-organization of tissue morphology. Since the bulk moduli of ECM fibres is much higher than the modulus of the network, the architecture of the network plays a crucial role on the transmission of forces and mechanosensing.

Experiments with mesenchymal cells plated on synthetic fibre networks have shown that, the degree of connectivity of the network and the stiffness of individual fibres control the proliferation and spreading rates [25]. Cells recruit the nearby fibres, which leads to an increase in local density and stiffness of the corresponding fibres, and suggested that there is a feedback mechanism between the recruitment of fibres and cell signaling (Figure 2.2b-c). This work is very relevant to this thesis as we based our actuation methodology on synthetic fiber networks.

For fibroblasts cultured on linearly elastic gels, the range of interaction is translated into one cell diameter [26], while for cardiac cells its range is expanded to few cell diameters [27]. The interaction range is significantly longer in the case of the native ECM. There are various reasons behind this increased range. One of the main components of ECM is collagen fibers. Fibrous gels are highly non-linear [28]–[31] and most of their constituents exhibit strain stiffening behavior and compression softening. Furthermore, the structure of the fibrous matrix define the way the material bears and transmits load generated by the native cells and the environment. The composition and architecture of the ECM can be quite dynamic as cells

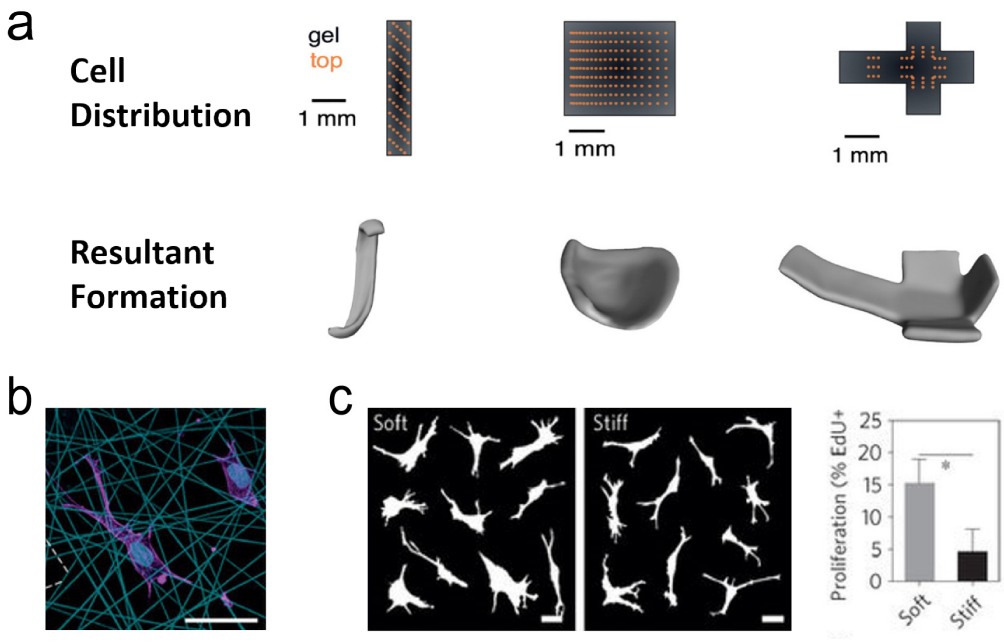

Figure 2.2 – Multicellular self-organization inside fibrous matrices. a) Folding of tissues with prescribed 3D shapes by patterning contractile cell clusters. Figure adapted from [24]. b) Cells cultured on an engineered synthetic fibre network. Scale bar, 100 µm. c) The role of fibre stiffness on cell spreading and proliferation. Scale bar, 50 µm. Figure adapted from [25].

can remodel matrix fibers via mechanical and chemical processes.

Three-dimensional microtissues can be grown between elastic pillar that serve as force sensors [32]. These pillar can be externally loaded using magnetic actuation [33] or the tissue can be surgically perturbed using robotic micromanipulators [34], [35]. Therefore, the overall platform offers to systematically investigate self-organization of cells embedded inside a collagen gel under tissue-scale stresses.

2.3.1 Computational modelling of force transmission

Along with experimental studies, extensive theoretical and computational modelling has been performed to understand the transmission of forces within fibrillar networks [36]–[38]. Most of the computational studies focused on the following question. How do mechanical forces generated by a single cell propagate to a distance that is far away from the cell? Cells

are modeled as contracting active elements. As a methodology to apply mechanical forces, particular location of the network corresponding to the location of the cell is extracted and displacement boundary conditions are applied to the nodes where the cell edge coincides with the fibre network [36]. Region of influence of a cell is determined by the level of contractility, shape of the cell, and stretching-bending energy ratio of fibres. With this computational framework, it has been shown that highly contractile and elongated cells generate forces that are transmitted to a distance that is ten times larger than the cell size.

Another approach of imitating cells is to put contractile elements in the fibre network, which is used to study the static amplification of stresses during the transmission of forces [39]. Three main phases are identified; a linear regime during generation of small forces, an intermediate non-linear regime, and a saturated regime at larger forces when the network is converted to a collection of tensed, inextensible ropes. In the aforementioned studies, the cells are modeled as displacing boundary conditions. To elaborate the cell scale mechanosensing, cellular protrusions are modelled in detail and mechanical interaction of cell and surrounding ECM is studied [40]. The computational model pointed out that the structure and amount of the protrusion of the cancer cells are related to their invasiveness.

3 Engineered Extracellular Matrices with Integrated Wireless Microactuators to Study Mechanobiology

Mechanobiology explores how forces regulate cell behaviors and what molecular machinery are responsible for the sensing, transduction, and modulation of mechanical cues. To this end, probing of cells cultured on planar substrates has served as a primary experimental setting for many decades. However, native extracellular matrices (ECMs) consist of fibrous protein assemblies where the physical properties spanning from the individual fiber to the network architecture can influence the transmission of forces to and from the cells. Here, a robotic manipulation platform that allows wireless, localized, and programmable deformation of an engineered fibrous ECM is introduced. A finite-element-based digital twin of the fiber network calibrated against measured local and global parameters enables the calculation of deformations and stresses generated by different magnetic actuation schemes across a range of network properties. Physiologically relevant mechanical forces are applied to cells cultured on the fiber network, statically or dynamically, revealing insights into the effects of matrix-borne forces and deformations as well as force-mediated matrix remodeling on cell migration and intracellular signaling. These capabilities are not matched by any existing approach, and this versatile platform has the potential to uncover fundamental mechanisms of mechanobiology in settings with greater relevance to living tissues.

This chapter is adapted from the following article [41]:

Uslu, F.E., Davidson C.D., Mailand E., Bouklas N., Baker B.M., Sakar, M. S. (2021). "*Engineered Extracellular Matrices with Integrated Wireless Microactuators to Study Mechanobiology*", Advanced Materials, 33, 2102641.

Author contribution

F. E. Uslu designed the experiments together with the senior author, performed the experiments and analyzed the data, and developed the digital twin. Fiber networks are provided by the Baker Lab.

3.1 Introduction

Many cells reside within complex 3D ECMs consisting of an interconnected network of micrometer-thick fibers. The filamentous architecture of the ECM and resulting mechanicalproperties have a direct influence on numerous biological processes, including those related to homeostasis, pathology, and regeneration [42]–[45]. Throughout these processes, cells probe and respond to the mechanical properties of the ECM using contractile forces and assemblies of mechanosensitive proteins [46]–[49]. Furthermore, discrete network architecture and nonlinear mechanics generate a spatially inhomogeneous and temporally dynamic reaction to the action of external and internal loads, including hydrostatic pressure, shear stress, and contractility of neighboring or distant cells [50], [51]. To dissect all of this complexity, fibrous matrices engineered from natural or synthetic materials have served as in vitro mechanobiology platforms. These platforms recapitulate the structural and mechanical properties of native tissue ECMs [52]. In particular, electrospun dextran fiber networks are particularly suited for this purpose given their tunable architecture (density, alignment, diameter), mechanics (stiffness, degradability), and surface chemistry [25]. Experiments using this tunable material platform have revealed that cells probe and respond to mechanics in fibrous matrices by recruiting nearby fibers, a mechanism that has profound impact on cell migration, proliferation, and the assembly of multicellular structures such as vascular networks [25], [53], [54].

Controlled mechanical micromanipulation of cells has played an instrumental role in the discovery of proteins and signaling pathways that sense mechanical signals and translate them into biochemical responses [55]. Adherent and suspended cells have been mechanically stimulated using magnetic and optical tweezers, aspiration micropipettes, microfluidics, and indentation probes [4], [5], [12], [56]–[63]. Alternatively, tensile forces can be applied to cultured cells on mechanically active substrates such as stretchable polymer sheets, actuated pillar arrays and photothermal hydrogels [10], [13], [14], [64]–[71]. Similar manipulation techniques have been explored to wirelessly characterize the mechanical properties of tissues.

Magnetically and thermally responsive probes have been encapsulated inside embryonic tissues or reconstituted collagen matrices for the characterization of tissue stiffness [72]–[75]. Implementation of a spatiotemporally controlled actuation paradigm capable of generating physiologically relevant forces within engineered fibrillar microenvironments would open new avenues to study the mechanics of cell-ECM interactions and how these interactions lead to the emergence of self-organization during development, and aberrant re-organization in the course of conditions such as fibrosis and metastasis.

The study of mechanobiology through ECM using untethered actuators presents two important challenges. On one hand, to recapitulate the fiber recruitment process that leads to multicellular organization, relatively large local deformations must be generated and sustained over long periods of time, lasting hours or even days. On the other hand, cells respond to dynamic mechanical stimulation within microseconds to minutes through calcium signaling, changes in focal adhesions or cell-cell junctions, remodeling of actomyosin cytoskeleton, and nuclear translocation of transcriptional regulators such as Yes-associated protein (YAP) and myocardin related transcription factor-A (MRTF-A) [76]–[80]. Here, we present a technology to mechanically interface with cells cultured on a tunable fibrous substrate while simultaneously monitoring the cellular responses and force-mediated changes in network architecture in real-time.

3.2 Actuation of fiber network via magnetic microactuators

We addressed all the aforementioned challenges using magnetically responsive microactuators (μ-actuators) integrated into matrices with cell-scale precision using robotic micromanipulation (Figure 3.1a). We have also developed a digital twin of the experimental specimen through imaging, computer vision, multiscale mechanical characterization, and finite element modeling of discrete fiber networks, enabling virtual testing of actuation schemes and quantification of mechanical stresses from empirical data.

The transport and assembly of the μ-actuators were performed using a dexterous motorized

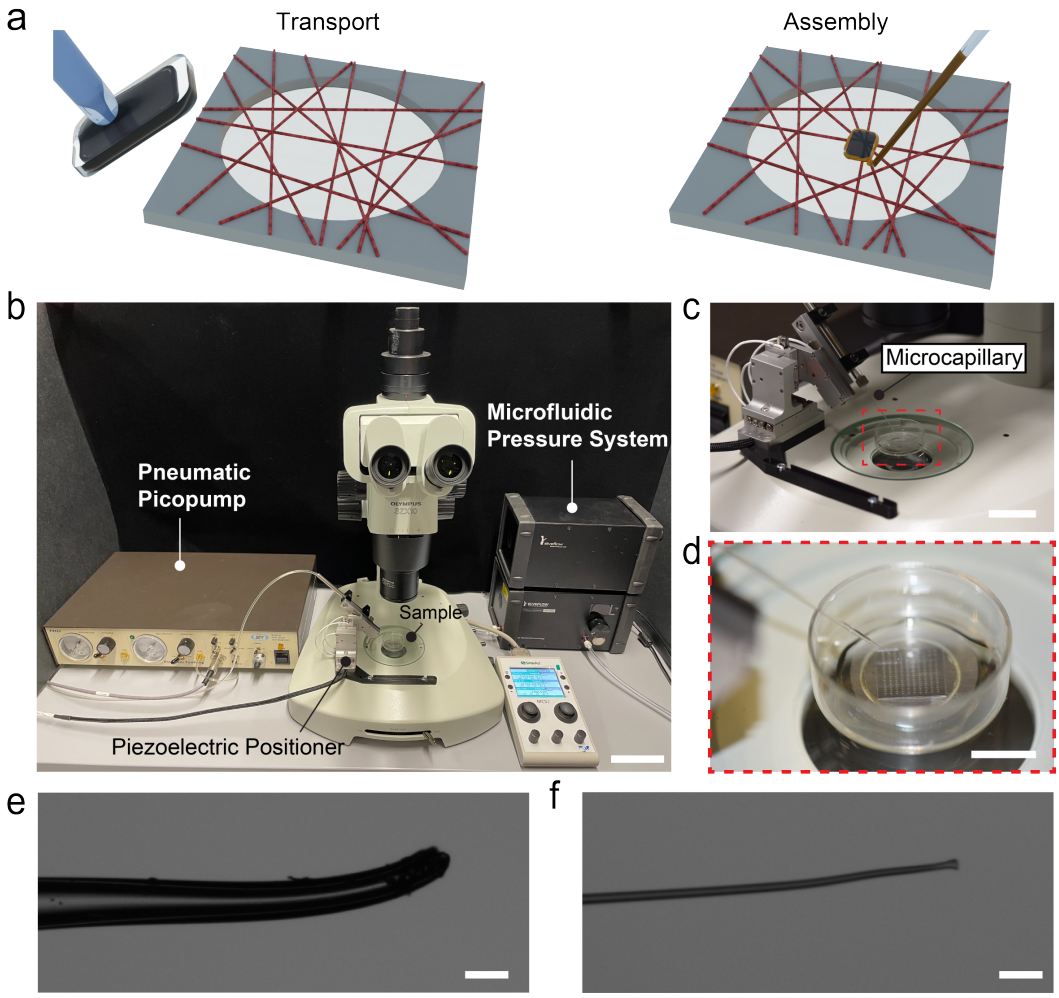

Figure 3.1 – Robot-assisted microassembly of µ-actuators. a) Schematics illustrating the positioning and assembly of magnetic microactuators (black block). Red beams represent DexMA fibers. DexMA is electrospun onto microfabricated substrates (shown in gray) to define networks of suspended fibers.b) A microfluidic pressure control system regulates pressure during the transport of the µ-actuator. A pneumatic picopump is used to controllably inject UV curable glue around the µ-actuator. The position of the capillaries are controlled by a 4-DOF piezoelectric positioner. Scale bar, 10 cm. c) A close-up view of the manipulator along with the capillary adapter. Scale bar, 3.5 cm. d) Wells containing fiber networks (n = 100) are within the yellow circle inside the Petri dish. Scale bar, 1 cm. Microcapillaries that are pulled and forged for the (e) transport of µ-actuators and (f) injection of glue material. Scale bars, 50 µm.

micromanipulation system and two different end effectors (Figure 3.1b-f). Both tools were pulled and forged from glass microcapillaries according to the size and geometry of the µ-actuator. The first end-effector is an aspiration micropipette connected to a microfluidic pressure system that provided dexterous transport and precise positioning of the µ-actuators

at the desired locations on the fiber network. The second end-effector consisted of a microinjection pipette connected to a pneumatic picopump for precise delivery of a biocompatible adhesive around the μ-actuator.

3.2.1 Fabrication and assembly of μ-actuators

Magnetic microactuators were fabricated from an electrodeposited nickel foil (Goodfellow, UK) using laser micromachining (DB Products, France). The nickel microactuators were dip-coated with in uncured PDMS and cured at 60o C for 6 h to protect actuators from oxidization and for ease of transport. PDMS-coated nickel microstructures were transferred to the target locations on DexMA fiber networks using a custom-made aspiration micropipette. Microcapillaries (CM Scientific, UK) were shaped using a micropipette puller (Sutter Instruments, USA) and microforge device (Narishige, USA). The tip of the micropipette has an inner diameter of 30 μm with a tilt angle of 25° to ensure application of firm suction to the microactuator (Figure 3.1b-f). The micropipette was connected to a microfluidic pressure pump (ElveFlow, France) for the pick-up and release of the microactuator, and a piezoelectric xyz positioner (SmarAct, Germany), for control of the position of the pipette tip in 3D. After contacting the microactuator with the pipette tip, 700 mbar negative pressure was applied and maintained until translation to the target location where the microactuator was released with the application of 50 mbar positive pressure. Microinjection pipettes with an inner diameter of 5 μm at the tip were fabricated using the same approach (Figure 3.1f). A UV curable glue (Norland Products, USA) was injected around the microactuators using a pneumatic picopump (World Precision Instruments, USA) and the same xyz positioner. The injected glue around the laser cut nickel was locally polymerized using a digital micromirror device (Andor, Oxford Instruments, UK) connected to a UV light source (CoolLED, UK). The adhesive ensured robust attachment of the μ-actuator to the neighboring fibers for the effective transmission of forces.With this methodology, μ-actuator(s) could be assembled at prescribed locations at defined orientations within a matrix (Figure 3.2). We did not measure any slack on the fiber networks due to the weight of the actuator or glue (Figure 3.3).

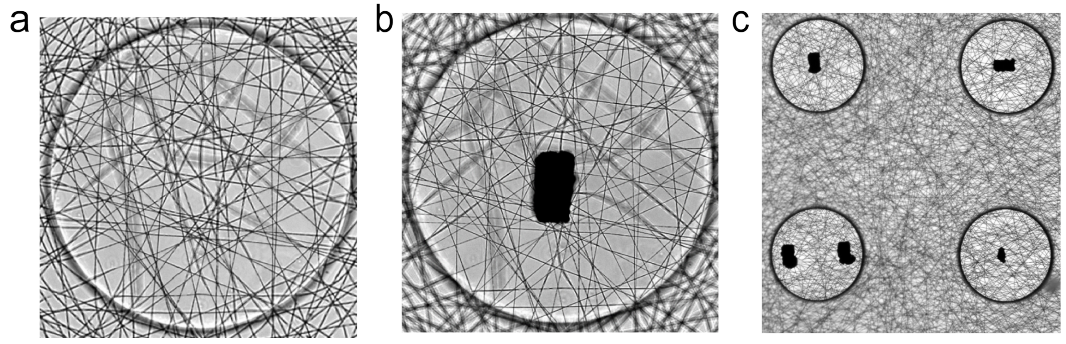

Figure 3.2 – Precise assembly of single/multiple µ-actuators. a) Phase-contrast images of a fiber network before the incorporation of a µ-actuator.b) Phase-contrast images of a fiber network after the incorporation of a µ-actuator. c) Single or multiple µ-actuators can be assembled onto the fibers at user-defined locations with desired orientations. The long side of the actuator can be as small as 50 µm.

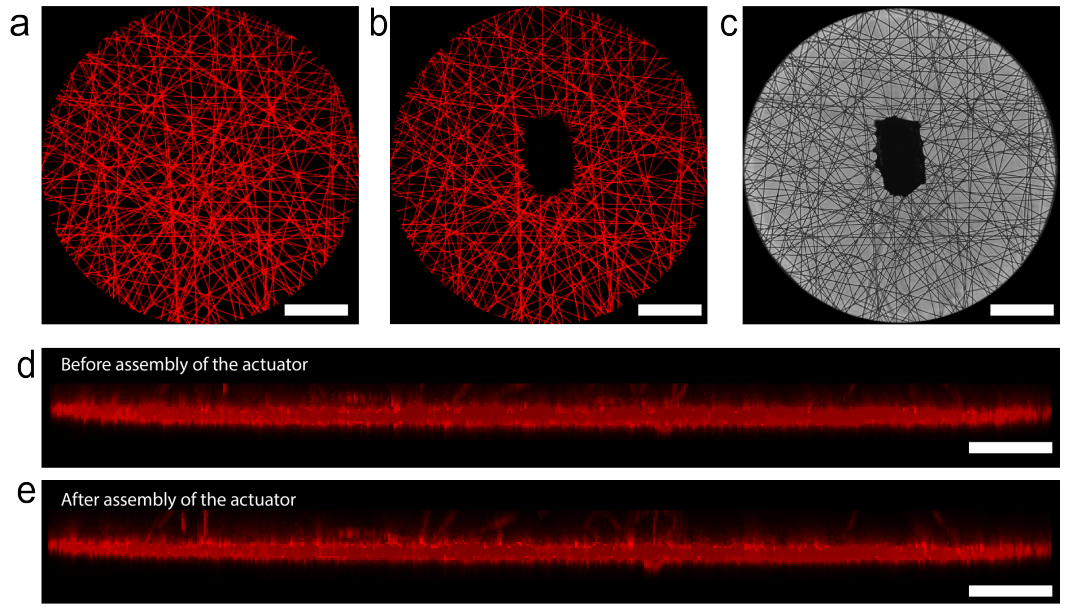

Figure 3.3 – The effect of weight on the state of the fiber network. Top-down view of the fiber network before (a) and after (b) the assembly of the µ-actuator. The fibers were fluorescently labeled in red. Scale bar, 100 µm. c) Bright-field image of the fiber network after the assembly. Scale bar, 100 µm. Side view of the fiber network before (d) and after (e) the assembly of µ-actuator. Scale bar, 50 µm. Side view is generated by sectioning the 3D reconstruction of the fiber network, which is formed from the 2D confocal scans.

3.3 Magnetic actuation platform

Matrices were generated from electrospinning methacrylated dextran (DexMA), which produces fibers that are resistant to non-specific protein adsorption. Fiber networks were de-

posited on a surface-functionalized array of microfabricated PDMS elastomer wells such that fibers were suspended across the wells. Fibers that resided outside the wells firmly attached to the elastomer surface, therefore, rigid boundaries were defined by the well perimeter. Networks were placed in a controlled humidity environment and provided sufficient moisture before light exposure to fuse or 'weld' all juxtaposed fibers. The platform allows execution of tens of experiments in parallel with user-defined initial conditions. Once the integration of the μ-actuator was completed, the substrate was submerged in culture media. The magnetic manipulation system consists of an array of eight permanent magnets spatially arranged to maximize the magnetic torque. A custom-design chamber that sits around the actuator ensures maintenance of physiological conditions (Figure 3.4). The magnetic field is uniform over 4.5x4.5 mm2 area on the plane that coincides with the sample, thus, the system only applies torque to magnetic structures that are within the workspace (Figure 3.5). We recorded the motion of μ-actuators located in the outermost wells during rotation of the external field and verified that the actuators did not move towards the permanent magnets. The magnetic field strength was kept at 40 mT in the center of the chamber while the system modulated the orientation of the magnetic field by precisely rotating the array using a piezoelectric motor with nanometric resolution. As a result, the system could hold the actuator at the desired orientation indefinitely during which the motor was turned off, enabling long-term time-lapse experiments. At the same time, the system operates at an angular velocity ranging from 0.0001 to 9.425 rad/sec, providing tunable strain rates with high resolution for the application of static or cyclic mechanical loading.

3.3.1 Magnetic control system

The circular magnetic control system consists of eight cube-shaped NdFeB permanent magnets (HKCM Engineering, Germany) with a volume of 1 cm3 and flux density of 1.43 T. The magnetic field strength in the workspace was measured using a Hall sensor (Hirst, UK) that was attached to a piezoelectric xyz positioner (SmarAct, Germany). The array was attached to rotational piezo stage (Physik Instrumente, Germany) with 0.02 resolution via a 3D printed

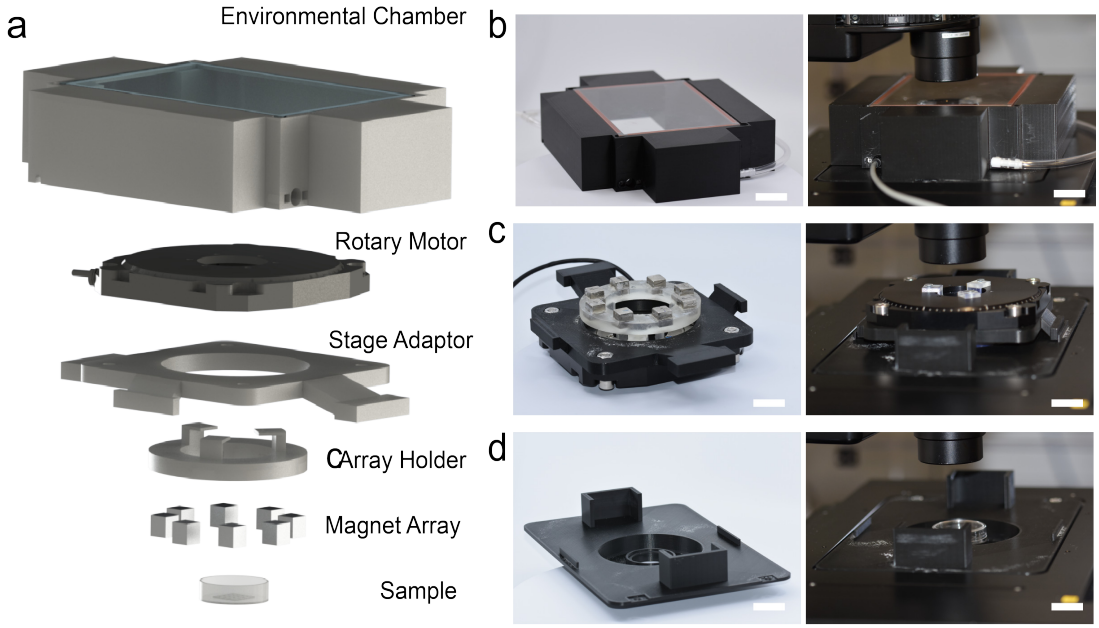

Figure 3.4 – Magnetic manipulation system. a) The uniform magnetic field is generated using a magnet array that is embedded into an array holder. The orientation of the µ-actuator is determined by the magnet array that is controlled by a rotary piezo motor. Environmental chamber maintains physiological temperature, pH and humidity inside the workspace.b) Environmental chamber for maintaining physiological conditions during cell culture. (Right) Once the sample is placed in the middle of the manipulation platform, the environmental chamber seals the workspace. c) The assembly of magnet array on the rotary motor. The nested manipulator secured on the microscope stage.d) Stage adapter part specifically designed for holding the magnet array on a motorized inverted microscope. The view of the adapter mounted on the microscope stage (right). d) f) Scale bars, 2 cm.

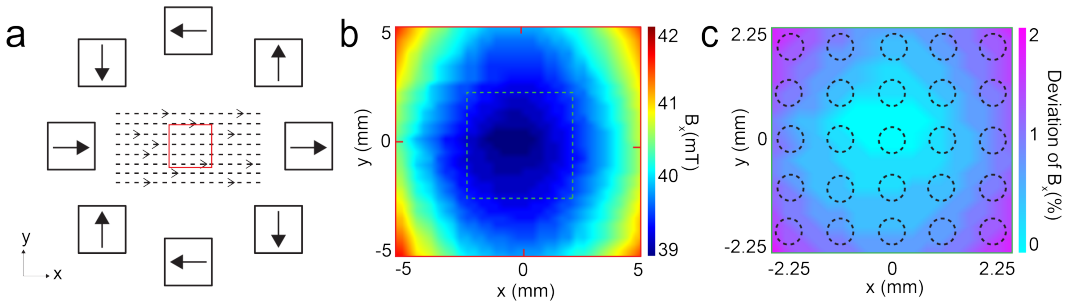

Figure 3.5 – Uniform magnetic field. a) Schematics showing the arrangement of the magnets within the array and the distribution of the magnetic field at the plane of the fiber networks. Red square denotes the area in which the fiber networks are located. b) Heat map of the recorded magnetic flux density inside the workspace. Highlighted area (dashed lines) contains a 5x5 grid of fiber networks from which the data is collected. c) Measured deviation in the x component of the magnetic flux density proves the homogeneity of the magnetic field.

adapter (Formlabs, USA). A 3D printed environmental chamber was assembled on the stage for time-lapse experiments. The motion of the stage was controlled using the GUI of a built-in MATLAB program. The program allows programmable actuation modes including rotation to a given position with a set angular speed and oscillations around a given position over a user-defined period.

3.4 Digital twin

We generated a digital twin of the physical experiment by computationally reconstructing the fiber topology and mechanics, and the motion of the actuator.

3.4.1 Topology reconstruction using image processing

Fluorescent images of the fibers were taken using a laser scanning confocal microscope (LSM700 Upright Confocal Microscope, Zeiss Germany) to image rhodamine fluorescence at 555 nm. Microscope images were binarized based on the intensity of pixels using a numerical implementation of Bresenham's line algorithm in MATLAB. Nodes and elements were converted into a sketch of lines using a CAD software (CATIA).

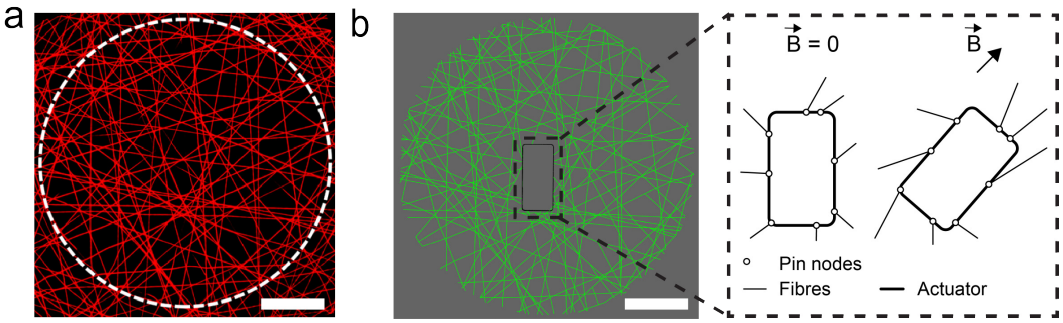

Figure 3.6 – Reconstructing the fiber network topology. a) A high-resolution fluorescence image of the fiber network that is used to generate the digital twin. b) A one-to-one digital replicate of the fiber network that is shown in (a). The discrete fiber network model is used to simulate the deformation according to the actuation signal. Pin nodes are generated between the fibers and the μ-actuator that are free to rotate. Scale bars, 100 μm.

We assumed that all fibers were on the same plane and an apparent intersection of fibers on

the 2D projection of the volumetric image stack constituted a permanent interfiber crosslink. With these assumptions, the image was processed to generate a list of nodes and links, which together represented the network topology. The links showed how nodes were connected to each other in each well, including the connections to the wall, which was segmented according to the arrangement of fibers crossing the barrier. The boundary conditions at the wall positions were considered to be fixed. A computational model was then created by interconnecting linearly elastic Timoshenko beam elements conforming with the topology of links (Figure 3.6), while accounting for finite deformations in 3D space. The average diameter of the fibers was measured as 1.8 μm from microscope images and we set the diameter of all the beam elements as such in the model. Experimentally, the matrix was imaged after integrating the μ-actuator, to define its exact position and orientation within the digital twin. A new set of nodes was created around the contour of the μ-actuator at connection points to the fibers, and a rigid plate of identical geometry to the μ-actuator was pinned to the network at those points as it influence the deformation via actution (Figure 3.7). Finally, actuation was modelled by imposing either displacement or torque of the rigid plate.

3.4.2 Finite element implementation

The digital twin consists of a constrained network of beams that is a one-to-one topological replica of the experimental specimen. We considered only a single layer of fibers in our virtual reconstruction while matrices had three to five layers of fibers due to the layering inherent to electrospinning – however, matrices were briefly exposed to humidity to weld points of interfiber contact, as described previously [25]. As such, all apparent intersections of fibers from a 2D projection of the network were considered rigid interfaces.

Finite element simulations were performed using a commercial software (Abaqus) and the Explicit/Dynamic solver to resolve multi-body contact between adjacent deforming fibers and rigid objects. The inputs to the computational model were the experimentally measured value of the Young's modulus of the fibers and the angular displacement of the microactuator. The fibers were modeled as linear elastic Timoshenko beam elements (B31) while accounting for

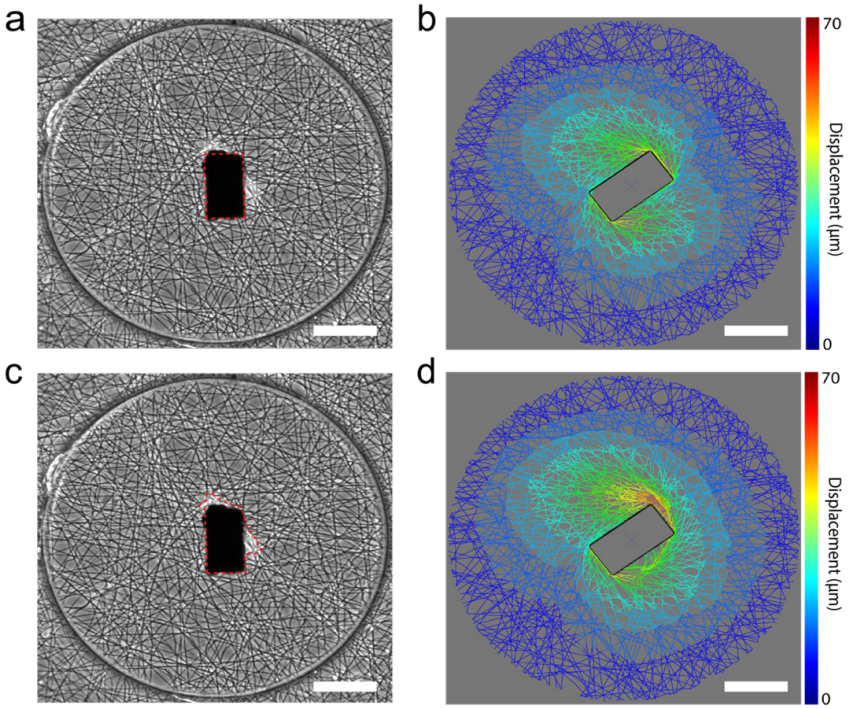

Figure 3.7 – The effect of glue spreading on force tranmission. a) Bright-field image of fiber network. Red dashed line is used as the boundary conditions in the simulation shown in (b). b) Displacement map that corresponds to the condition where we used the boundaries of the acuator. c) Bright-field image of the fiber network. Red dashed line, which traces the contours of the UV curable glue, is used as the boundary condition. d) Displacement map of the network that corresponds to the boundary condition given in (c). Scale bars, 100 μm.

finite deformations. Both the microactuator and the microindenter were defined as rigid shell elements with a reference point in the middle. The ratio of kinetic to total energy of the system was kept to less than 0.01 through mass scaling to ensure that simulations were performed in quasi-static equilibrium. Fibers were discretized using a mesh that corresponds to beam elements of 4 μm in length.

With the use of correct constitutive equations appropriate for the range of local fiber deformations, the computational model is expected to accurately estimate the mechanical stresses, effectively realizing traction force microscopy on a fibrous substrate. Nanoindentation of hydrated single DexMA fibers using atomic force microscopy showed that constitutive behavior of individual fibers can be captured through isotropic linear elasticity with a Young's modulus of 22±5.53 MPa (Figure 3.8a-b). The simulations were run based on the empirical mean value

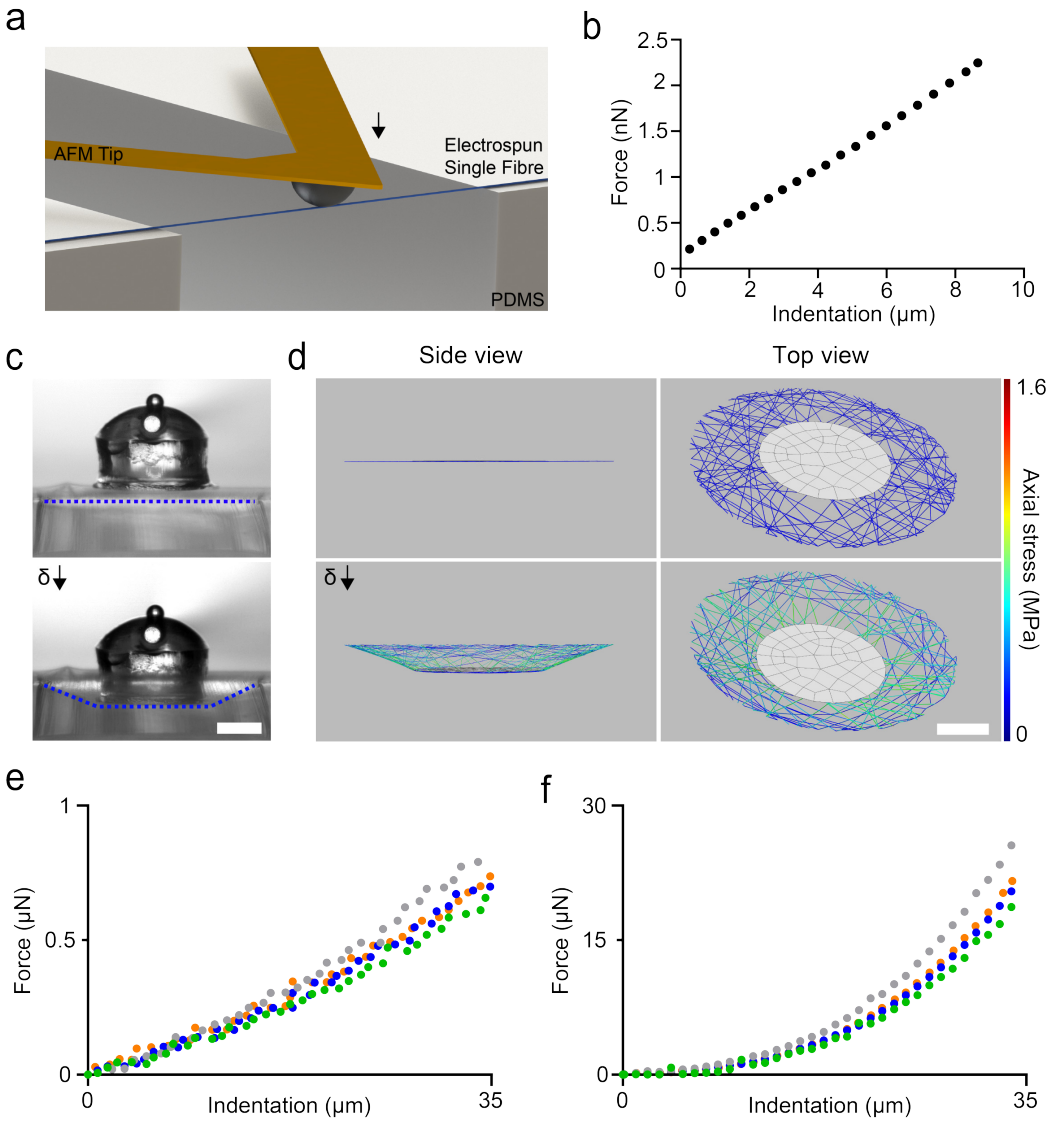

Figure 3.8 – Mechanical characterization and model validation. a) Three-point bending tests are performed on single fibers using atomic force microscopy. b) A representative force vs deflection curve. The Young's modulus of the fibers is calculated from these measurements. c) Micrographs from a a bulk indentation experiment. The cylinder with a dome-shaped cap is the indenter and the dashed lines (blue) highlight the deformation of the fiber network. d) The indentation of the digital twin of the sample shown in (c) with identical conditions (i.e. indenter size and indentation depth). Empirical (e) and simulated (f) force values from the indentation trials for four different fiber networks in their hydrated state. Scale bars, 100 μm.

of the Young's modulus while Poisson's ratio was taken as 0.49, assuming incompressibility of the fibers. To experimentally validate the in silico force calculations, we performed microindentation of fiber networks (Figure 3.8c, **Movie S1**). In tandem, the digital copy of the

discrete network was mechanically loaded using a model of the rigid indenter with the same dimensions, assuming no friction at the contact area (Figure 3.8d). The fiber network can be approximated as a thin linearly elastic perforated membrane at the continuum level, and as such, geometric nonlinearities are expected to arise when the specimen is significantly indented. The nonlinear response was evident in the shape of the force-indentation curves (Figure 3.8e-f).

The fibers swelled upon hydration, where the diameter increased by 60 % from 1.12 ± 0.15 µm to 1.8 ± 0.2 µm. The associated volumetric expansion has two important consequences for the network mechanics: a reduction in the Young's modulus of the fibers and fiber buckling due to the constraints around the network (Figure 3.9). We performed additional indentation tests in air to quantify the effect of fiber swelling on network mechanics (Figure 3.10). The measured forces were two orders of magnitude higher than the values recorded on hydrated samples (Figure 3.8e). This discrepancy may arise from two major differences between the physical matrix and theoretical model.

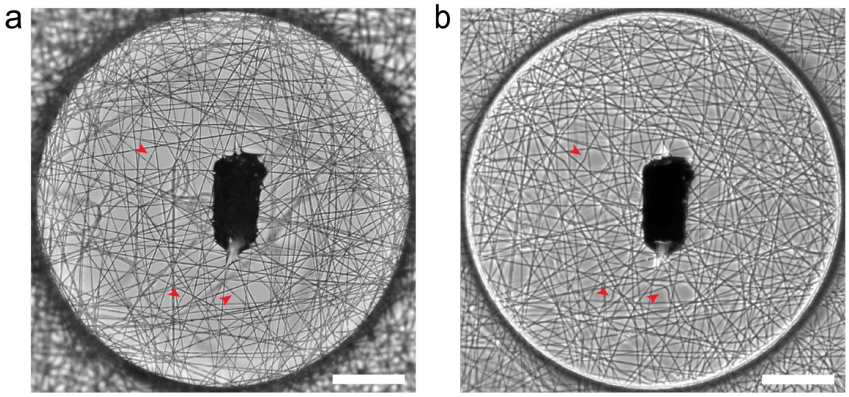

Figure 3.9 – The effect of swelling and hydration on fiber mechanics. A fiber network in the (a) dry and (b) hydrated state. The red arrows point to three representative fibers where expansion with swelling leads to buckling. There are many more fibers in a given network that show mechanical instabilities after hydration. Scale bars, 100 µm.

First, we created the computational model based on the non-swollen state of the network (capturing network connectivity and fiber topology) due to the difficulty of modelling buckled fibers. A network with links that do not bear loads is expected to be softer compared to a network in which all the fibers are tight at the initial state. In addition, the connectivity of the

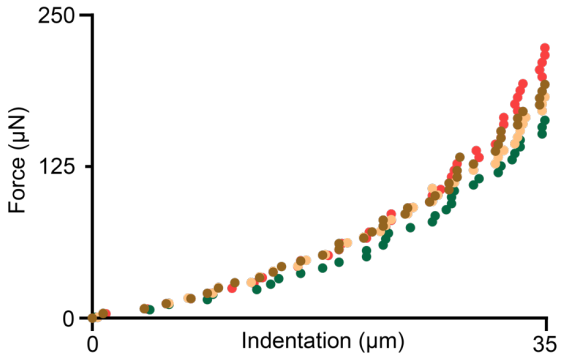

Figure 3.10 – Indentation tests on fiber networks in air. Four different fiber networks are tested using a 250 µm indenter.

network is higher in the model because we projected multiple layers of fibers into a single plane and assumed that all apparent intersections of fibers are welded crosslinks. As expected, the simulated network stiffness was higher than the stiffness measured from hydrated samples (Figure 3.8f).

3.4.3 Validation of the computational model

We have used linear elastic model while enabling large deformations on single fibers. AFM measurements of single fibers showed a pure elastic behavior. As a confirmation of the elasticity of the fiber network, we have performed two different stress relaxation tests on the networks: bulk microindentation test and local actuation test. We performed microindentation of the fibre network for extended durations. Differing from the test shown in Figure 3.8e, the indenter was kept at 300 µm indentation (the diameter of the sample is 500 µm) for 30 minutes while recording the stress (Figure 3.11a). We recorded a maximum of 10% decrease in stress at the end of the test. Compared to the stress relaxation reported on collagen gels and native tissue samples, this level of relaxation is very low (Figure 3.11b, reproduced from [81]). Collagen gels completely relax the stress within the same time period. There are method to introduce stress relaxation into synthetic fibers.

We intentionally worked with a linearly elastic material to first address the nonlinearities

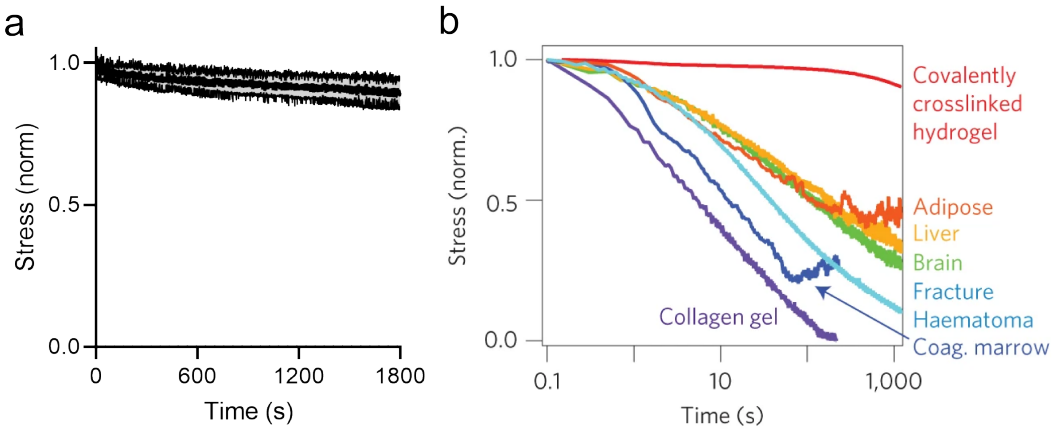

Figure 3.11 – Stress relaxation in the synthetic fiber network and natural ECMs. a) The results of the stress relaxation experiment from three different samples. b) Stress relaxation tests of a crosslinked hydrogel (polyacrylamide), a collagen gel, an initial fracture hematoma (human), and various tissues (rat) at a strain of 15%. Stress is normalized by the initial stress. Adapted from [81] for convenience.

raised by the structure. Such a system also serves as a benchmark to study which effects require the existence of stress relaxation in the ECM. In our future work, we will update the material properties as well as the constitutive relations used in modelling to make the overall platform more biomimetic.

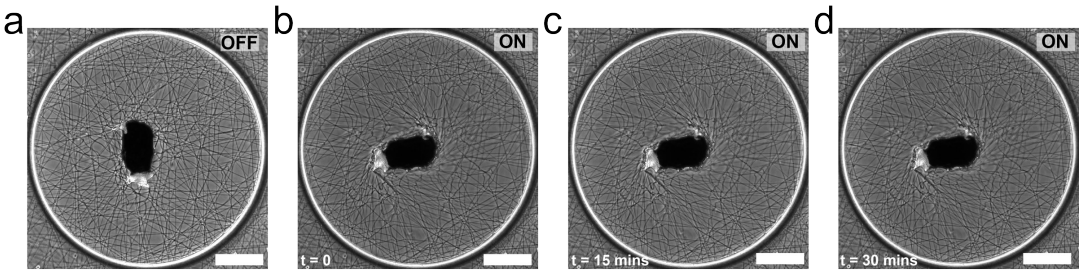

Figure 3.12 – Long-term magnetic actuation. Bright-field images of a fiber network before and during actuation. Scale bars, 100 µm.

In the second stress relaxation test, we used a magnetic microactuator to load the network (Figure 3.12). We kept the actuator at a maximum rotation angle for 30 minutes. We did not record any further rotation at that given torque, which would indicate relaxation of stress on the network. Taken together, we can safely ignore the effect of viscous dissipation in the current version of our model.

3.4.4 Magnetic torque calculation

We computed the magnetic torque acting on the soft magnetic actuator by modeling its shape as ellipsoid. The magnetic torque that tends to align the long dimension of the body with the applied field is given by:

$$\boldsymbol{T} = \mu_0 \upsilon(\boldsymbol{M} \boldsymbol{x} \boldsymbol{H}) \tag{3.1}$$

where the body lies in an external field with a value $\boldsymbol{H}$ at the body's center of mass and the field magnetizes the body to a magnetization $\boldsymbol{M}$. The volume of the magnetic material is denoted by υ and the permeability of free space is $\mu_0 = 4\pi 10^{-7}$ T·m/A. At fields low enough such that $|\boldsymbol{M}| < m_s$, the magnitude of the torque can be computed as[82]

$$|\boldsymbol{T}| = \frac{\mu_0 \upsilon |n_r - n_a|}{2 n_a n_r} |\boldsymbol{H}|^2 \sin(2\theta) \tag{3.2}$$

where n_a and n_r are the demagnetization factors, and θ is the angle between $\boldsymbol{H}$ and the axis of symmetry. The maximum torque applied by a μ-actuator, that is 100 μm long and 50 μm wide, is calculated as $|\boldsymbol{T}|_{max} = 1.06 \times 10^{-9}$ N·m. When we applied $|\boldsymbol{T}|_{max}$ in the digital twin of a particular fiber network, the actuator rotated 2.75º instead of the empirically recorded rotation of 88° (Figure 3.13a-b). As described above, this discrepancy is due to the overestimation of network stiffness in our model. As indicated by the indentation data shown in Figure 3.8e and Figure 3.8f, the force calculated by the computational model was higher than the measured value for the actual samples. We recapitulated the experimentally recorded deformation by scaling the input torque to the same extent, i.e. by taking $|\boldsymbol{T}|_{max} = 3.15 \times 10^{-8}$ N·m(Figure 3.13c).

3.5 Actuation of the engineered matrices

The samples were placed inside the workspace of the magnetic manipulation system in a way that the μ-actuators were aligned along the direction of the external homogenous magnetic field (Figure 3.14a). We call this initial configuration corresponding to a state of zero magnetic

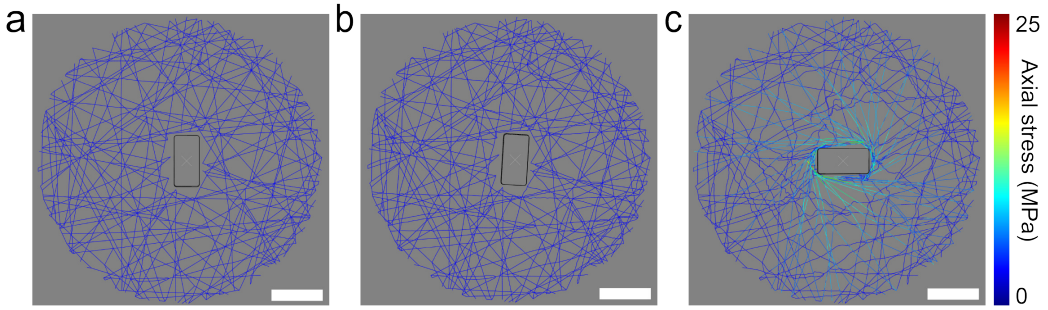

Figure 3.13 – Simulated stress using magnetic torque as the input. a) Equilibrium configuration. b) The stress map upon application of $|T|_{max} = 1.06 \times 10^{-9}$ N·m. The μ-actuator rotates by 2.75°. c) The stress map upon the application of the scaled torque, $|T|_{max} = 3.15 \times 10^{-8}$ N·m. The μ-actuator rotates by 88°. Scale bars, 100 μm.

torque the equilibrium state. The μ-actuator synchronously rotates with the external field to minimize the magnetic dipole interactions and lower the energy (**Movie S2**). There exists a field rotation frequency, known as step-out frequency, above which the applied torque is not strong enough to keep the actuators synchronized with the field. Our μ-actuator followed the driving field even at the maximum speed that the system could generate, therefore it is not necessary to consider step-out in our experiments(**Movie S3**). On the other hand, the fiber network serves as a spring, applying forces to resist the rotation of the μ-actuator. This restoring spring force increases with increasing angular displacement and, once the torque applied by the system is balanced by the spring force, where additional field rotation does not further rotate the μ-actuator or lead to more matrix deformation. For the chosen physical properties of the fibers, μ-actuators, and magnetic manipulation system, this angle was recorded as 90° ± 6°. Decreasing the density or stiffness of the fibers and increasing the shape anisotropy or volume of the μ-actuator would naturally lead to a higher maximum displacement angle.

The rotation of the μ-actuator applies spatially inhomogeneous load-sharing in the network, leading to tensile or compressive mechanical stresses, depending on the fiber orientation and local connectivity. As a result, some of the fibers were stretched while others buckled due to compression (Figure 3.14). Fibers attached to the left-top and right-bottom corners of the μ-actuator were pulled due to the rotation, which led to formation of aligned fiber bundles that were under tension. The overall deformation of the network was measured using

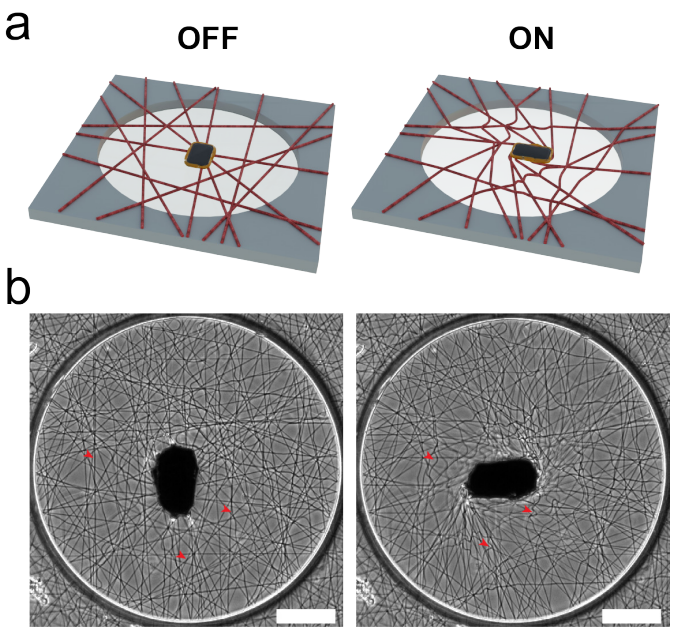

Figure 3.14 – Actuation creates tension lines and buckling on the fiber network. a) As soon as the network is placed within the magnetic manipulation system, a torque clamp is activated for the μ-actuator. Any deviation on the orientation of the μ-actuator would generate a restoring magnetic torque. The orientation of the μ-actuator is dynamically modulated to apply a local deformation to the fiber network. b) A representative fiber network in the equilibrium configuration. (Right) Fiber network during the application of a magnetic torque that lead to 89º rotation of the μ-actuator. Red arrows point to fiber elements that display buckling upon actuation. Scale bars, 100 μm.

fluorescent microbeads encapsulated inside the DexMA fibers, serving as fiducial markers(**Movie S4**). We applied the same mechanical load to the digital twin by rotating the rigid plate in the model to the equilibrium orientation of the μ-actuator (Figure 3.15a). We defined points in the computational model that corresponded to the exact empirical positions of the fluorescent microbeads to compare the displacement of the fibers during the actuation. Figure 3.15b shows representative plots displaying the trajectories of the beads. The particle tracking velocimetry data is also shown as displacement vectors, drawn from the initial to the final position of the marker points (Figure 3.15c). As an important remark, unlike experiments, the digital twin can provide high-resolution information on the deformation because the positions of all the points on the network along with stresses and strains of the individual fibers could be traced in the simulations (Figure 3.15d).

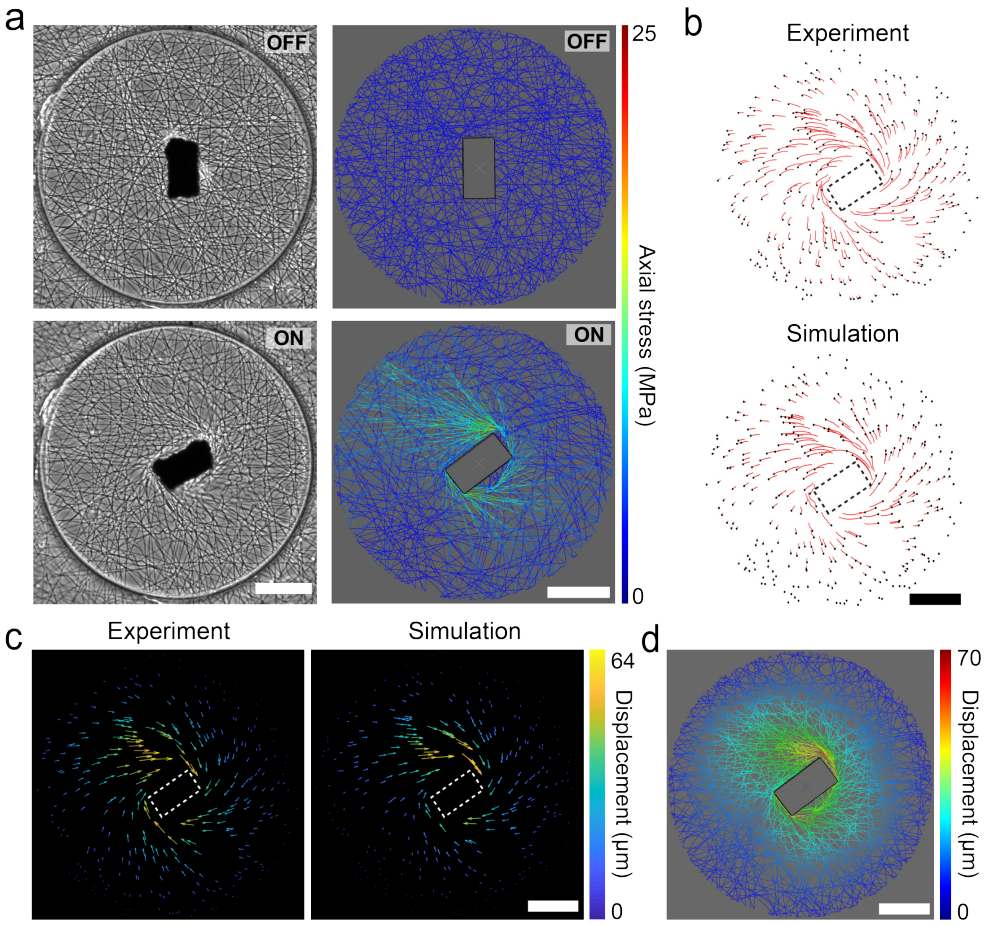

Figure 3.15 – Experimental and computational investigation of the actuation paradigm. a) Phase-contrast images showing the operation of the μ-actuator. The magnetic field is rotated by 90o from the equilibrium configuration. A digital twin of the fiber network shown on (right) is manipulated to the same degree. The simulation results report the stress on the fibers along with the strain. b) The deformation is quantified by tracking fluorescent beads randomly distributed on the fiber network (top). The trajectories of points at the positions of the fluorescent beads are calculated by the computational model (bottom). c) The motion of the nodes introduced in (b) are displayed as a vector field for the experiment (left) and the digital twin (right). d) The displacement of all the nodes within the network are calculated using the digital twin. Scale bars, 100 μm.

The results showed that the digital twin accurately predicted the deformation of fibers in response to the motion of the μ-actuator. Notably, reeling of the surrounding fibers due to the rotation of the μ-actuator recapitulated the fiber recruitment resulting from cell generated forces (Figure 3.16). A single endothelial cell pulls the adjacent fibers up to 50 μm before making new connections or migrating forward while the rotation of the μ-actuator by 90°

resulted in 70 µm displacement of the nearby fibers.

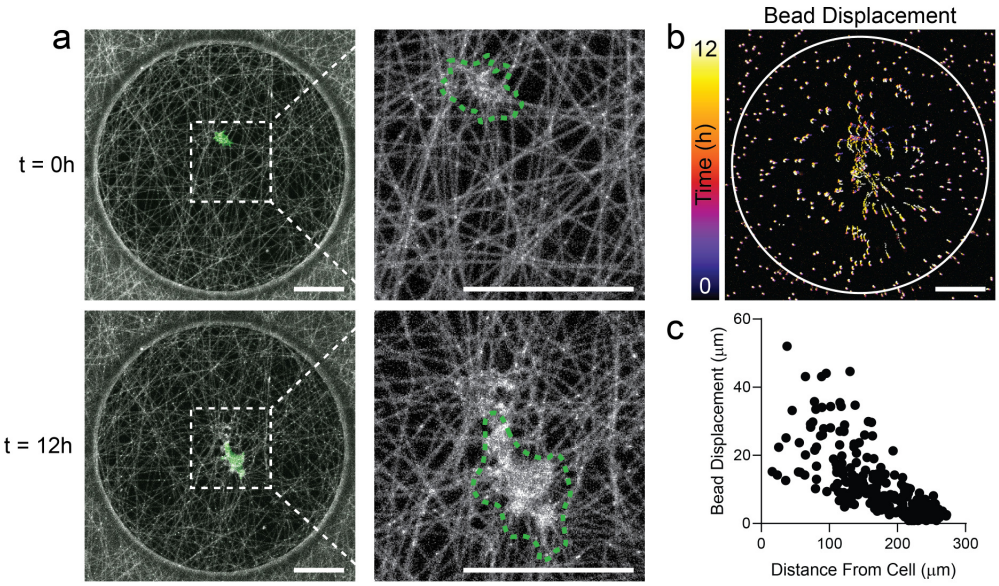

Figure 3.16 – Cell force-mediated fiber reorganization. a) A single endothelial cell was seeded within a fiber network and imaged for 12 hours; F-actin(green), DexMA fibers (grey). Dashed boxes indicate locations of higher magnification images depicting fiber recruitment underneath the cell body (dashed green outline). b) Temporally color-coded overlay of fluorescent beads embedded within fibers over 12 hours following endothelial cell seeding and c) quantification of bead displacement distance as a function of its distance from the cell centroid. Scale bars, 100 m.

3.5.1 Reliability of the actuation scheme

The deformation generated by the microactuator is reversible and repeatable. We have performed experiments to demonstrate the reversibility. We oscillated the microactuator from vertical position to clock-wise 90° and measured the deformation on the network via tracking beads encapsulated inside fibers. Figure 3.17a shows the deformation at 90° after the first oscillation as a bright-field image and tracking bead trajectories (color code is the displacement of the beads), above and below respectively, while Figure 3.17b and Figure 3.17c shows deformation after 10th and 100th. The results prove that the mechanical signal generated by the microactuator is identical even after 100th actuation.

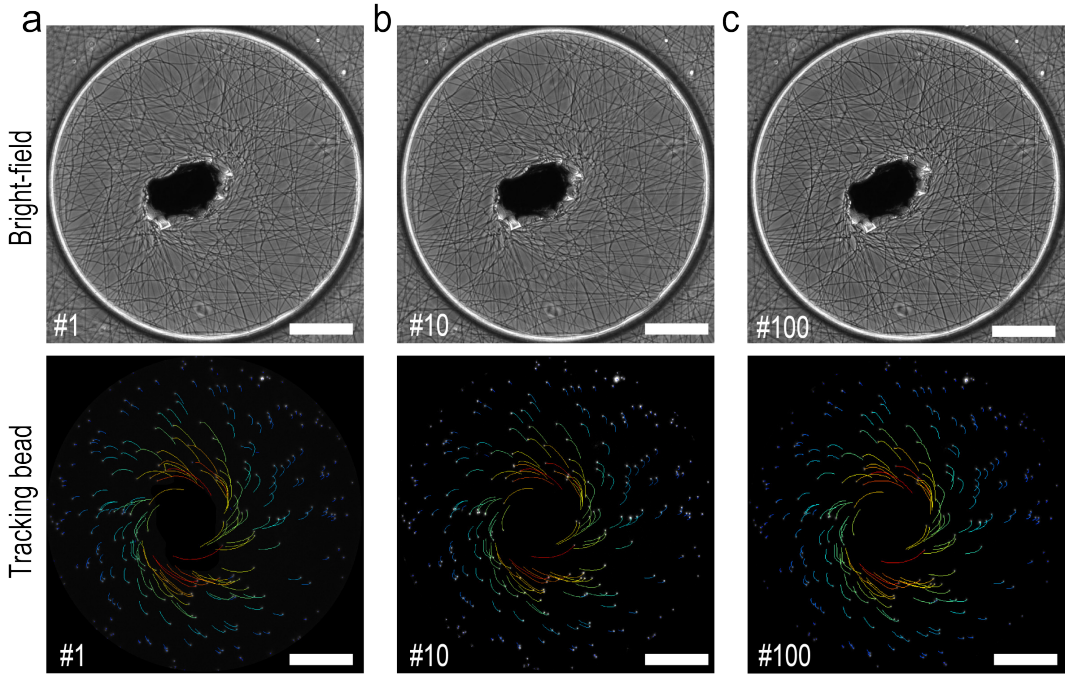

Figure 3.17 – Repeatability of the mechanical actuation. a) Bright field image of an actuated fiber network (up) and the resulting bead displacement (bottom) during the first actuation cycle. b) Bright field image of an actuated fiber network (up) and the resulting bead displacement (bottom) during the 10th actuation cycle. c) Bright field image of an actuated fiber network (up) and the resulting bead displacement (bottom) during the 100th actuation cycle. Scale bars,100 µm

3.5.2 The importance of accurate modelling of network topology

The computational framework could be used to interrogate the combinatorial effects of network topology and actuation protocol (e.g. the number, distribution, size, and shape of actuators) on the deformation of the network. As a proof-of-concept example, we fixed the configuration of the actuator and simulated the deformation for two extreme network topologies, i.e. fibers aligned uniaxially and patterned as a regular grid. The simulation results clearly showed that, depending on the network topology, a cell might experience very different mechanical loads for the same input torque and µ-actuator configuration (Figure 3.18a-b). As a further inquiry on the importance of network topology, we removed only a few connections from a representative network while keeping everything else intact. The stress changed significantly at certain locations upon actuation, corroborating with the previous results

(Figure 3.18c-d). Taken together, these demonstrations showed that replicating the exact topology of the network in computational simulations is essential for the accurate prediction of deformation and associated stress in discrete fibrous substrates.

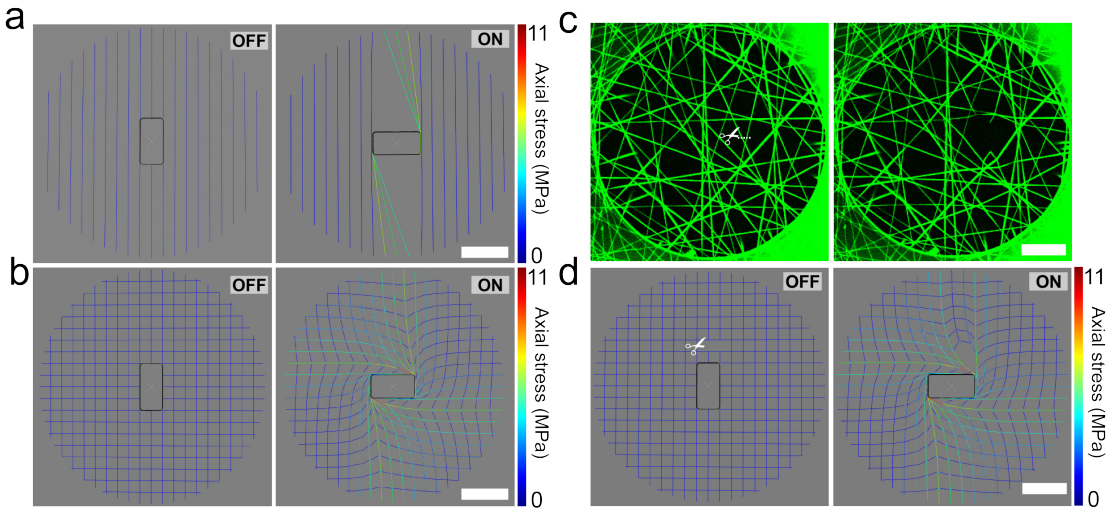

Figure 3.18 – Computational analysis of the effect of fiber architecture on the distribution of stress. a) Fiber network with vertically aligned fibers before (left) and during (right) actuation. b) Fiber network with a regular grid architecture before (left) and during (right) actuation. The extreme example shows how certain areas of the network is not stimulated in the absence of proper connections among the fibers. c) Fluorescent images of a fiber network going through laser microsurgery. The scissor icon points to the disrupted link. d) Removal of two links from the network shown in (b) leads to shielding of stress beneath the disrupted links. Scale bars, 100 μm.

3.5.3 Actuation of collagen matrices

Even though we do not use bulk collagen gels in our platforms, we have ability to actuate bulk collagen gels via μ-actuators. As a proof of concept demonstration, we integrated a magnetic actuator into a thin film of reconstituted collagen I gels with varying densities (from 0.5 mg/mL to 2 mg/mL). The actuator can faithfully follow the external magnetic field, generating torque, and deforming the bulk gel (Figure 3.19). We observed alignment of collagen fibers around the actuator, as a manifestation of tension propagation. We would like to point out that it is quite challenging to create a discrete fiber network model for such bulk gels and, as a result, previous work only focused on the development of continuum coarse-grain models, which

can only estimate bulk stress [83].

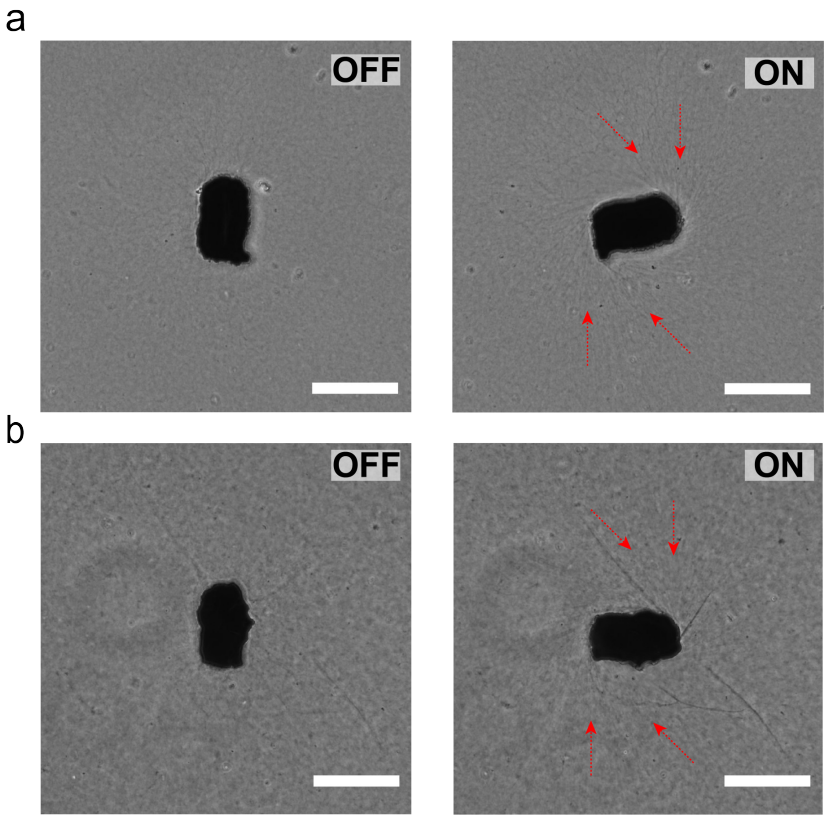

Figure 3.19 – Magnetic actuation in collagen matrices. Bright field images of a μ-actuator embedded inside a thin film of (a) 0.5 mg/ml and (b) 1 mg/ml collagen gel. Red arrows higlights regions where collagen fibers are aligned due to the tension applied by the actuator. Scale bars, 100 μm.

3.6 Experiments with living cells

3.6.1 Fibroblast migration is guided by induced matrix alignment

We started our biological investigation by asking the following question: Can we influence cell migration in our platform with the strain generated by the μ-actuator? To this end, we seeded fibroblasts on fibers that were functionalized with cell-adhesive peptide RGD as illustrated in Figure 3.20a. 3T3 fibroblasts adopted a spindle shape possessing thin, elongated processes that terminated in branched protrusions, resembling their morphology on type I collagen matrices (Figure 3.20b). The system can be operated under a torque clamp without consuming power.

When the adherent cells changed the orientation of the μ-actuator by pulling on the fibers at the equilibrium state, a magnetic torque whose magnitude depended on the misalignment angle acted to restore the orientation of the μ-actuator(**Movie S5**). While maintaining the initial orientation, the μ-actuator occasionally translated along with the connecting fibers. This experiment showed that the forces applied by the magnetic system to the network is comparable to the forces applied by the cells.

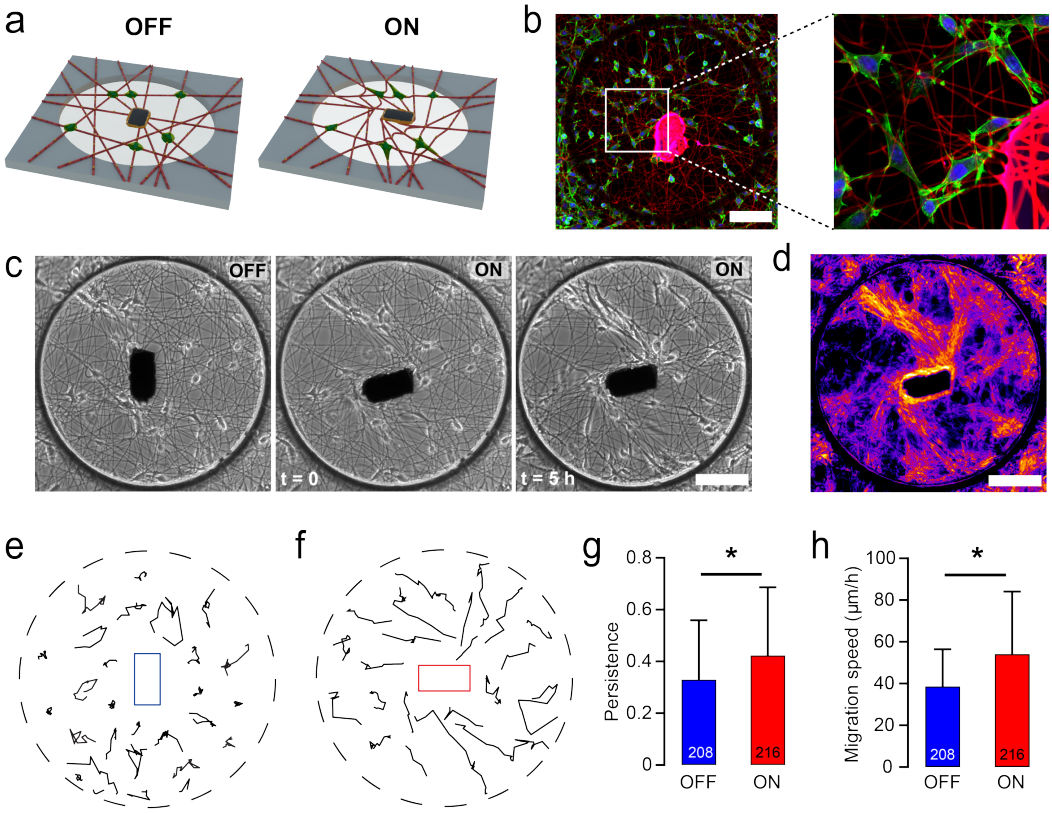

Figure 3.20 – Local matrix alignment by the μ-actuator influences cell migration speed, directionality, and persistence. a) Schematics illustrating the local actuation of the fiber network seeded with fibroblasts (green). b) Fibroblasts adhere to the RGD-coupled fibers, spread, and migrate. Cells were counter-stained for F-actin (green) and nuclei (blue) with phalloidin and Hoechst 33342, respectively. The glue polymerized around the μ-actuator shows autofluorescence in the red channel. c) Temporal sequence of phase-contrast images shows the increasing density of fibroblasts migrating along the aligned fibers. d) Heat map of the overlay of micrographs taken every 15 min for 6 hours highlight the cell trajectories. Representative fibroblast migration tracks over a 6h time course on (e) non-actuated and (f) actuated fiber networks. Key characteristics of cell migration such as (g) persistence and (h) migration speed increases with the local actuation. All data presented as mean s.d. and * indicates a statistically significant comparison with $p < 0.05$ (two-way analysis of variance). Scale bars, 100 μm.

Physical features of the ECM such as rigidity and geometry influence cell morphology, polarization, and cell motility[84], [85]. This process can emerge as a result of the local deformations and remodeling of the fibrillar ECM. We mechanically loaded the networks by rotating the magnetic field 90° in clockwise direction at 0.1 rad/sec. Fibroblasts seeded in the vicinity of the μ-actuator moved to the aligned fibers within 2 hours and constrained their motion along these lines of tension during the remainder of imaging (Figure 3.20c,**Movie S6**). Overlaying phase-contrast images of the samples highlighted deterministic trajectories that followed the same multicellular activity pattern in all the actuated wells (Figure 3.20d). Increasing local fiber alignment led cells to adopt an elongated uniaxial morphology and migrate with enhanced speed and persistence compared to the control case where the fiber networks were left in the equilibrium state (Figure 3.20e-h). We have recently shown that cells stretch matrix fibers to store elastic energy and subsequent adhesion failure at the cell's trailing edge can trigger a sudden matrix recoil and rapid cell translocation [54]. This distinct mode of migration, which we termed slingshot migration, was displayed more frequently on aligned matrices. We recorded a 21.9 % higher occurrence of slingshot migration on actuated matrices(**Movie S7**), supporting the critical role of aligned fibers and matrix-borne forces in this phenomenon.

3.6.2 Initiation of calcium signaling via mechanical loading

The rotation of the μ-actuator not only modifies ECM alignment but also presents active mechanical cues by stretching constituent cells. Cells can detect and transduce mechanical forces into biomechanical signals using a variety of mechanosensitive proteins. Of particular interest, stretch-activated ion channels respond to membrane tension by altering their conformation between an opened and closed state, facilitating mechanically gated ion flux into cells [86]. Among different anions and cations, intracellular signaling initiated by calcium (Ca^{2+}) passage has been shown to play a key role in mechanotransduction of non-muscle cells [87]–[89]. We used fluorescence video microscopy and a Ca^{2+} indicator to monitor signal transduction in cells during the course of actuation. Epithelial cells were cultured on the substrate at a relatively low density to ensure that forces were transmitted through the fibers and not through

cadherin junctions. Cells that reside along the direction of tension were clearly stretched in the course of actuator rotation (Figure 3.21a-b). We recorded up to 10-fold increase in fluorescence intensity of the Ca^2+ indicator above the baseline value within 1 to 5 seconds after force application which returned to the baseline within 20 to 30 seconds. Notably, the signal initiated at the pole of the cell nearest the μ-actuator, and propagated through the rest of the cell body (Figure 3.21c-e,(**Movie S8**)). We postulate that the spatiotemporal propagation of the signal was due to the release of Ca^{2+} from the intracellular stores in response to the influx of extracellular Ca^{2+} across the plasma membrane stemming from matrix stretch.

3.6.3 Plasticity of epithelial tissues during external loading

Epithelia cells are one of main components of organs as they cover and have vital functionalities for the organs, such as digestion, respiration and wound healing[90]. It is shown that epithelial cell layers are reactive to mechanical signals in addition to chemical and biological signals [91]. Response and adaptation of epithelial cells to mechanical signals also affect the organ functionalities and it is crucial to understand principles of their adaptation capabilities to these signals. In the literature, either freely growing epithelia monolayers [92] are investigated, or large-scale stretching [88] are applied to study epithelial monolayer dynamics. However, adaptation capabilities of the monolayers to local and cell scale forces are still missing, which makes the mechanical principles of their adaptation unclear. Since we have the capability to generate local forces with our actuator, while the fibre network recapitulates the connective tissue attached to epithelia layers in the body, we have started to elaborate our studies on epithelia layers. We have designed experiments where we locate the actuator in the middle of the network, rotate it 90°, maintain it for 24 hours and remove the magnetic field (Figure 3.22a). We have observed three main angles throughout the experiment to characterise their adaptive capabilities, where $\alpha 2$-$\alpha 1$ can be defined as adaptation angle and $\alpha 3$ as plasticity angle (Figure 3.22b). After the first set of experiments with 24 hours of actuation with 90 degrees of rotation, we have extended our experiments by changing the duration of the actuation and amount of force we are applying, 48 hours of actuation with 90 degrees (Figure 3.22c) and

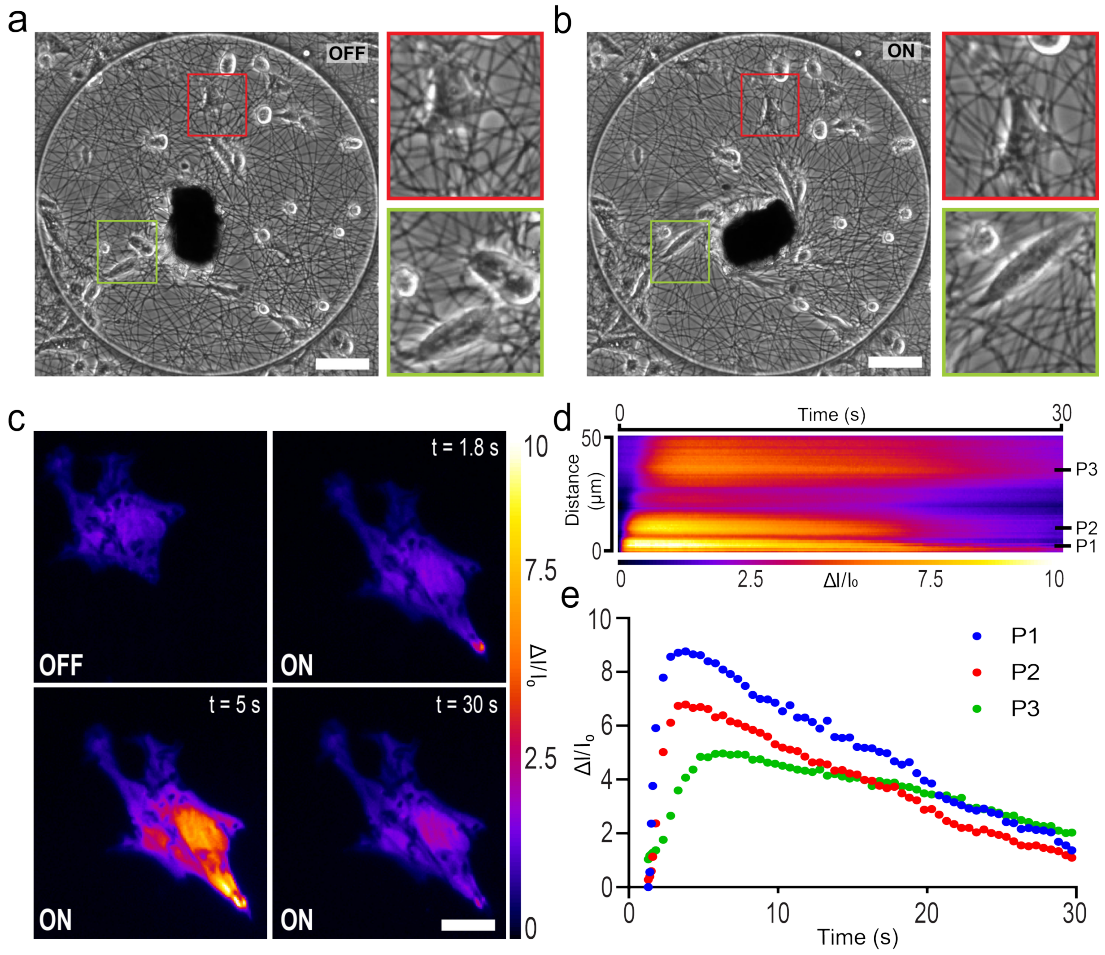

Figure 3.21 – Mechanical loading of epithelial cells through fibers activates stretch-activated ion channels. a) Bright-field image of a fiber network seeded with epithelial cells. Two single cells are magnified (red and green boxes) to clearly show the effect of actuation. b) The network shown in (a) is actuated as the magnetic field is rotated by 90o from the equilibrium configuration. Insets show the tensile loading of the cells. Scale bars, 100 µm. c) Time-lapse images of Ca2+ indicator shows the initiation, propagation and decay of the intracellular signal. Scale bar, 20 µm. d) Kymograph capturing the spatiotemporal propagation of the Ca2+ signal on the central line of the cell presented in (c). The line starts from the tip of the cell (bottom right of the image) and ends at the other end of the cell. e) The normalized intensity of the fluorescence signals are recorded from three different points inside the cell. Locations of these points are indicated on the kymograph shown in (d).

24 hours of actuation with 45° (Figure 3.22d), respectively. In both of the cases, adaptation and plasticity angle shows significant differences. We are now designing new experiments to understand what these differences mean in terms of multicellular adaptation, where we are going to use blocker drugs to inhibit the proliferation of the cells as proliferation might be one

of the critical adaptation mechanisms.

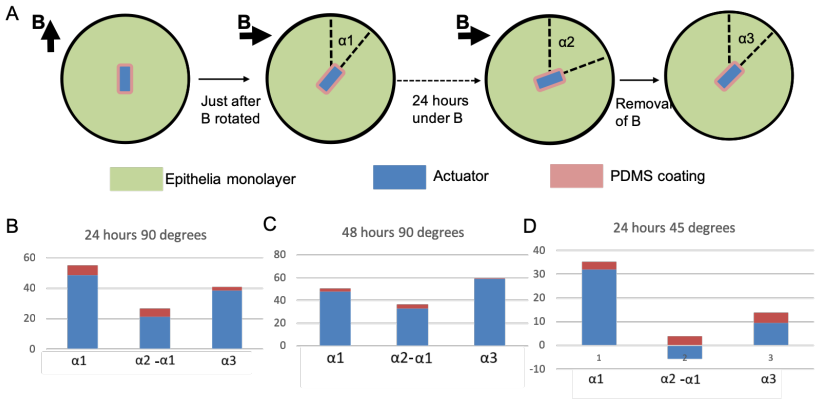

Figure 3.22 – Epithelial plasticity. (a) Experimental pipeline with epithelial cells. B is the external magnetic field applied by Halbach array with the arrow showing direction (b) $\alpha 1$, $\alpha 2$-$\alpha 1$, and $\alpha 3$ for 90° of rotation and keeping the magnetic field at 90° for 24 hours (c) $\alpha 1$, $\alpha 2$-$\alpha 1$, and $\alpha 3$ for 90° of rotation and keeping the magnetic field at 90° for 48 hours (d) $\alpha 1$, $\alpha 2$-$\alpha 1$, and $\alpha 3$ for 45° of rotation and keeping the magnetic field at 45° for 24 hours

3.6.4 The influence of mechanical loading on the polarity of the nucleus

Deformation of nucleus plays an important role on the nucleus translocation, which regulates the response of the cell against deformation. It is reported that the nucleus behaves as a mechanical sensor and mechanical stretching of the nucleus due to cellular deformation opens the stretch-activated pores on the nucleus membrane [93], [94]. Activation of the pores initiates cascaded protein activity to augment actomyosin contractility for motility. We have showed that the constant mechanical stress (Figure 3.23a), applied on the sparsely seeded epithelial cells, change their nucleus shape in an hour (Figure 3.23b). We have characterized the nucleus shape change with the percentage change of eccentricity. We have observed that the eccentricity increased (Figure 3.23c).

3.7 Discussion

Actuation based on the application of magnetic torque has several advantages over alternative techniques. Optomechanical actuation, which is particularly appealing considering the spatial

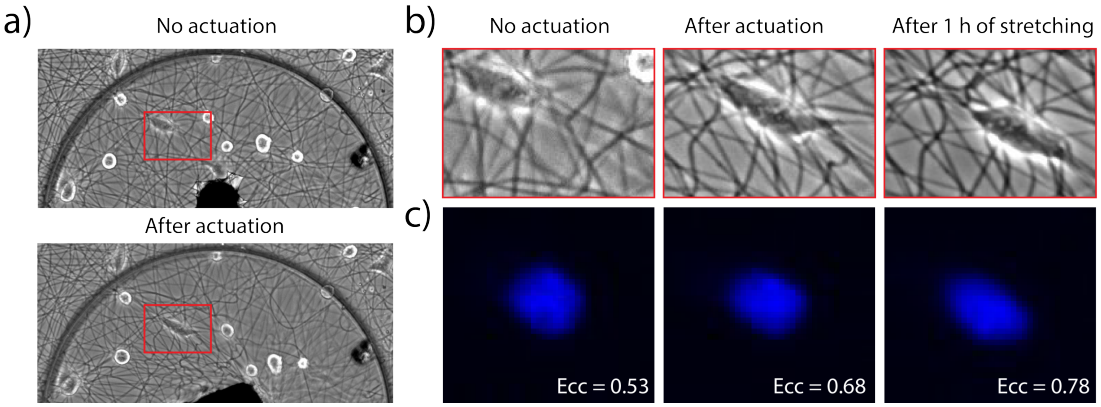

Figure 3.23 – Nucleus shape adaptation to actuation. (a) Actuation of the sparse epithelial cells. Left, before actuation. Right, after actution. (b) Temporal sequence of zoomed-in epithelial cell, indicated in the red box in a. (c) Temporal sequence of DAPI labelled cell nucleus presented in b.

and temporal resolution of laser illumination [13], [14], [71], [95], is limited in throughout because simultaneous illumination of multiple distributed actuators is not possible in existing systems. Furthermore, continuous illumination is required in order to apply forces, which raises issues regarding local heating and power consumption. Our technology not only addresses these issues, but also generates significantly higher deformation on matrices through rotation and reeling of fibers (Table 3.1). We have also fabricated thermoresponsive actuators and examined their capability to deform the matrix. We obtained 37 µm of maximum displacement on the fiber network, while we can create 70 µm displacement with magnetic µ-actuators.

It is possible to increase the amount of displacement of 70 µm via µ-actuator. To be able to generate higher maximum deformation with the same magnetic manipulation system, the aspect ratio of the µ-actuator could be increased. If the experiment requires the generation of the same level of deformation using a smaller µ-actuator, the actuator could be manufactured from a material with higher magnetization.

The simulated value of the indentation force was an order of magnitude higher compared to the measurements made in a hydrated state. We made three basic assumptions in the construction of the model: i) the loading state does not change after the swelling process, ii)

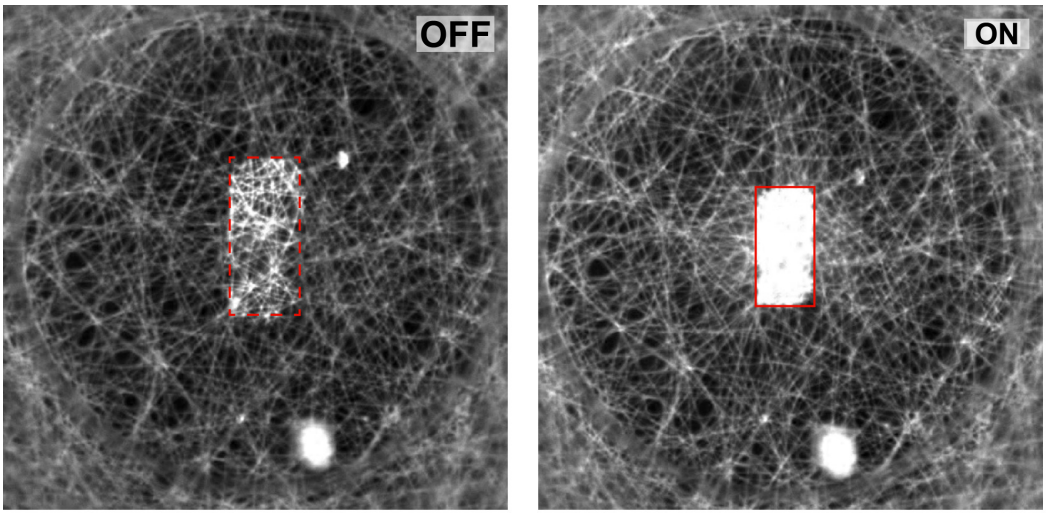

Figure 3.24 – Actuation of thermo-mechanical NIPAM actuators. (Left) The actuator in OFF mode is located in the middle of the fiber network and shown with red dashed line. (Right) The actuator is actuated with laser, shown with red line, and generated 37 37 μm of maximum displacement.

there is only one layer of fibers, and iii) all the nodes correspond to stable fiber connections. As shown by the experiments, swelling of fibers led to local buckling due to boundary conditions. In addition, although we applied a process to weld fiber intersections prior to hydration, we recorded that fibers occasionally slid with respect to each other at contact points during experiments. Connectivity has a significant effect on the apparent elastic modulus of a network of randomly aligned fibers. Overestimation of network connectivity and omitting hydration-driven mechanical instabilities led to a stiffer virtual twin of the network at the continuum level compared to the actual specimen. More realistic models of the networks can be generated by i) introducing volumetric fiber swelling to capture the buckling instabilities upon hydration, ii) using a realistic 3D model of the network that is obtained via higher resolution volumetric reconstruction, and iii) incorporating fibers that come in contact with each other without being rigidly bonded.

Ca^{2+} imaging experiments showed that only the cells adhering to fibers directly connected to the corners of the μ-actuator experienced stretch-activated Ca^{2+} flux. The rest of the fibers within the network also bore stress, but potentially not at high enough levels to open stretch-activated ion channels. In addition to the amplitude, the frequency of the mechanical signal

can also play an important role in biological output. Previous work has shown that cyclic stretching of cells cultured on soft substrates induces spreading, stress fiber formation, and proliferation [79]. Notably, several studies reported nuclear translocation of mechanosensitive proteins MRTF-A and YAP under external mechanical loading while the duration, amplitude, and frequency of the chosen loading conditions varied [14], [68], [96]. The rate at which forces are applied also influences force transmission and subsequent signaling [23]. Our platform is capable of generating physiologically relevant dynamic mechanical signals and, in contrast to the existing platforms, is able to do so within a tunable engineered fibrous matrix. Finally, the rotation of the μ-actuator could be dynamically modulated according to the real-time mechanical feedback of cells informed by time-lapse imaging. This novel experimental platform can in the future examine adaptive cellular force responses in homeostasis, pathology, and regeneration.

Actuation Method	**Substrate**	**Tethered(T) vs Untethered(U)**	**Local(L) vs Bulk(B) actuation**	**High-throughput**	**Long-term continuous actuation**	**Fiber recruitment**
Mechanical probing with glass pipette[4], [58]	Glass slide	T	L	No	No	No
AFM Indentation[5], [59]	Glass slide	T	L	No	No	No
Magnetic twisting cytometry[56]	Well plate	U	L	Yes	No	No
Optical tweezer[12]	Well plate	U	L	No	No	No
Shear stress in channels[57]	Collagen gel	U	B	Yes	Yes	No
Stretching substrate with servo motor[65], [67], pressure[68], dielectric elastomer[70]	Elastomer	T	B	Yes	Yes	No
Magnetic nanoparticles[63]	Glass slide	U	L	Yes	No	No
Magnetic micropost[10], [69]	Elastomer	U	L	Yes	Yes	No
Light triggered thermomechanical actuation[13], [14], [71]	Polymer coated glass	U	L	No	No	No
Ferrofluidic droplets[72]–[74]	Embryo	U	L	Yes	Yes	No
Thermal actuation of hydrogel beads[75]	Spheroid	U	L	Yes	No	No
This Work	**Engineered ECM**	U	L	Yes	Yes	Yes

Table 3.1 – Comparison of existing micromanipulation techniques with the presented technology.

4 Background II - Laboratory techniques to study self-organization in insect colonies

Ant and honeybee colonies are ideal experimental models to study physical principles of self-organization. Such principles have been inspiring in the development of swarm robotic systems [97]. These social entities manage to complete several collective tasks such as foraging for a new nest and brood-rearing without centralized instructions [98]. Individual members collect information from their environment and exchange information with their nest-mates using their antenna and pheromones. In addition, they are capable of communicating through physical activities such as the waggle dancing. Analogous to the role of fibre networks in multi-cellular tissues, the spread of information among ants and honeybees depends on the spatial and social structure of the colony. To decipher the physical principles of self-organization in insect societies, it is instrumental to observe the whole colony while keeping track of individual identities. The capability to physically manipulate individuals and characterize the response of the colony would reveal key insights on the nature of local interactions and collective actions.

4.1 Techniques to track members of a colony

There are three major techniques to visually investigate the behavior of groups of insects. Marking the body of individuals with paint [99] or attaching a visually identifiable tag to each animal [100], [101] are two widely accepted techniques to record colony activity while following the identity of individuals. More recently, machine learning based techniques introduced the capability to track individuals without the use of markers [102]–[105].

Figure 4.1a shows several painted ants physically interacting with each other. Labeling ants with paint is relatively straightforward. However, the number of ants that can be simultaneously tracked is limited by the manually generated pattern. Moreover, paint material degrades over time. As an alternative solution, automated video tracking system based on the use of fiducial identification labels has been introduced (Figure 4.1b). Hundreds of individual ants can be tracked over day and night for weeks using infrared illumination. These data sets enable the construction of social interaction networks as will be demonstrated in the next chapter. Tracking individuals with fiducial identification labels was also used in honeybee colonies

[106], [107]. The results obtained from tracking of individuals and their social interactions demonstrated that the individual variability in the honeybee workers cause major differences in their collective behavior.

Deep learning based techniques enabled to track individuals of honeybee colonies without the use of barcodes or other markers (Figure 4.1c). Similar techniques have been applied to track termites, fruit flies, and locusts [105]. Markerless tracking of fruit flies revealed important insight on social cluster formation [108].

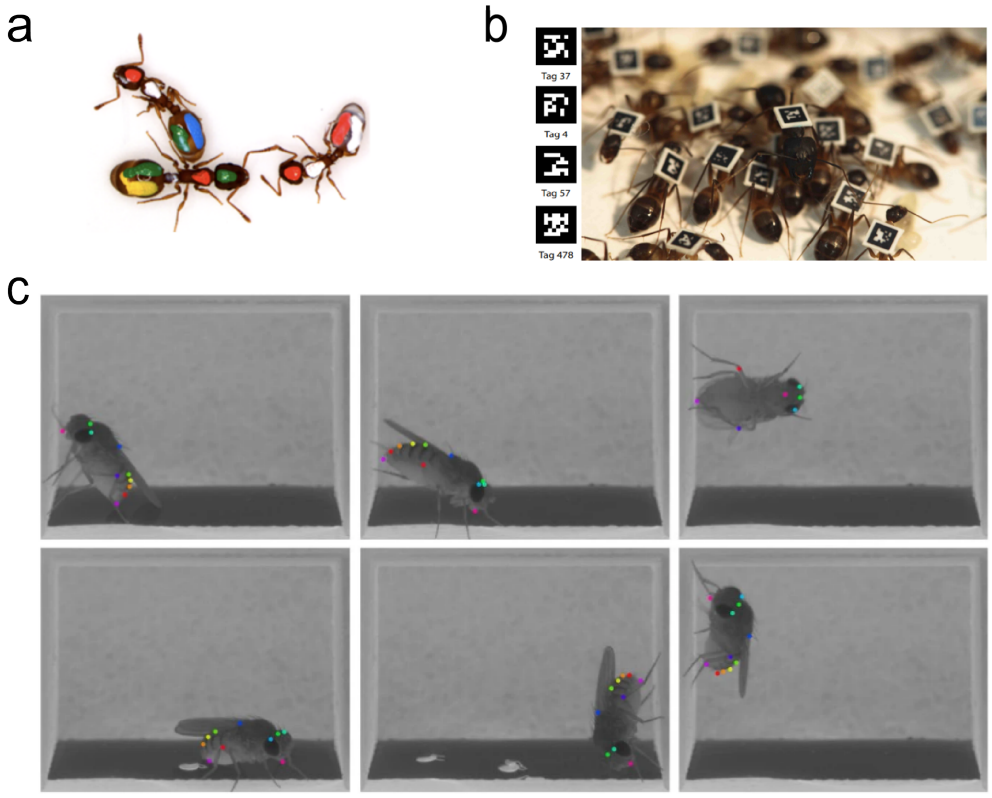

Figure 4.1 – Tracking the individuals in insects. a) The individual ants are tracked by painting their body. Figure adapted from [99]. b) The individual ants and their interaction are automatically tracked via barcodes. Figure adapted from [100]. c) Automated markerless tracking of insects. Figure adapted from [102].

4.2 Physical manipulation of individuals within groups of insects

A number of methods have been introduced to physically interact with insects in a colony or interrupt their physical activity. For example, the waggle dance of the honeybees was disturbed using a small paintbrush [109]. The results indicate that the reduction in the mass change in the hive due to foraging decreases when the waggle dance was interrupted. Another highly relevant work has shown that physical manipulation using an insect-sized magnetic metallic disc could recapitulate a collective behavior stemming from physical interactions among flies [110]. Touching the legs of a fly with the magnet induced a similar effect that was observed when they collided with each other (Figure 4.2).

Robotic devices can be used to manipulate colony behavior [111]. In a very relevant example, robotic devices were developed that generated thermal, mechanical, and fluidic signals on the surface of a honeybee nest [112]. In another work, a bee-sized robot was programmed to imitate the waggle dance [113]. The robot bee managed to make honeybees follow her. Similarly, a robot cockroach was programmed to interact with living cockroaches [114]. The robot managed to initiate a collective behavior, choosing a shelter for the group.

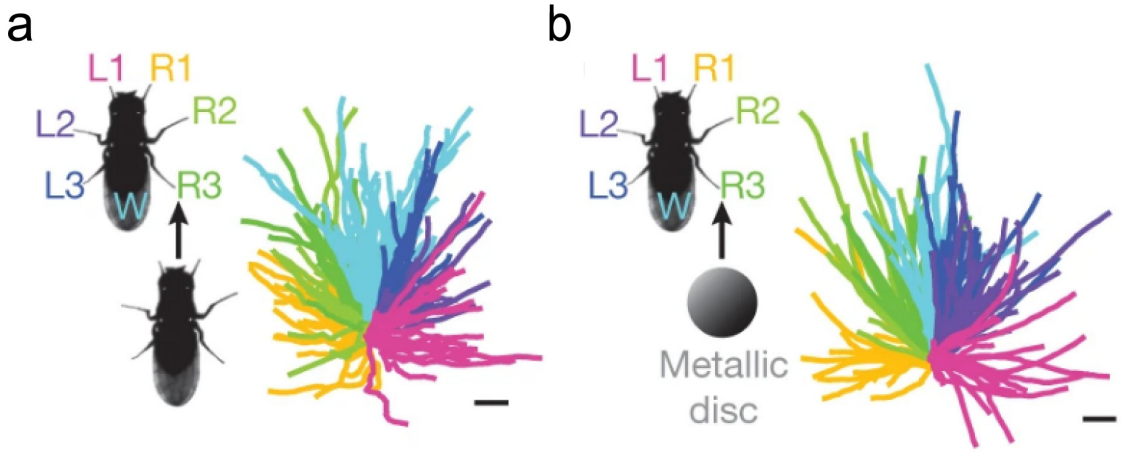

Figure 4.2 – Physical interaction driven collective motion in flies. a) One fly (left) is pushed by another fly (right). The color-coded trajectories show the behavior as a result of this mechanical interaction. Scale bar, 1 mm. b) The same fly (left) is pushed by a metallic disc manipulator (right). A similar kinematic behavior is observed. Scale bar, 2.5 mm. Figure adapted from [110].

4.3 Thermoregulation in ant colonies

Ants exchange information, transport resources, and nurture brood through physical sensation and contact [98]. Physical sensation may involve detection of temperature changes inside the nest, the spread of a pathogenic agent, or a wake-up call from a fellow ant. Experimental evidence has shown that the speed and extent of transmission of signals depend on the spatiotemporal dynamics of the triggering event. Thermoregulation is important for the proper development of offspring and metabolic regulation of adults [115]–[117]. Ants collect information on the ambient temperature with their sensors and initiate collective transport of brood as well as migration to more favorable regions. The existing literature is limited to the quantification of the thermal limits above which colonies collapse.

There is another line of work which has been instrumental in the development of our analysis pipeline. Ants show organizational immunity to pathogens which involves dynamic changes in interaction patterns for the separation of infected members from first class members such as the queen [118]. Extensive modelling work has been conducted to explore the dynamics of disease spreading in social networks [119]–[123]. These studies showed that the topology of the interaction network and the state of special individuals called “super-spreader” are critical aspects. Super-spreaders are on top of the chain due to their superior network centrality measures such as degree, betweenness, and centrality [121].

As demonstrated in the next chapter, introducing thermal signals with high temporal and spatial resolution give us the opportunity to discover further insights about adaptive self-organization in ant colonies.

5 A programmable temperature regulation system to study principles of self-organization in ant colonies

Ant colonies work together to care for their brood. One of the important physical condition that ensures proper development is the ambient temperature. Ants can measure the temperature of their surrounding physical environment and move the brood to protect them from harsh conditions, a process that is part of a larger thermal regulation mission. We have developed ThermoReg, an autonomous temperature regulation system, for spatiotemporally controlled manipulation of temperature of the nest floor. Using this novel system, we explore the dynamics of brood translocation. The results show that only a subgroup of the colony perform brood transport, and this group of ants show adaptive response to different thermal signals. Finally, we present data that suggest that there is no colony level decision making and ants seem to be driven by individual preferences and state.

This chapter is adapted from the following manuscript:

Uslu, F.E.*, McGregor, S.*, Keller, L., and Sakar, M. S. "Investigating individual and social aspects of thermoregulation in ant colonies" (in preparation).

Author contribution

Uslu, F.E. designed, engineered and validated the temperature regulation system, **Uslu, F.E.** and McGregor, S. performed the experiments, analyzed the data, and interpreted the results.

5.1 Introduction

Ants have spread out and conquered almost every available land surface, asserting themselves as the most ecologically dominant species by biomass second only to humans. One of the critical factors for this ecological success is division of labour [124], a ubiquitous, defining feature of the eusocial insects, whereby work is split up into a number of discrete tasks performed by separate individuals. Ant colonies may contain over a million individuals and yet, despite the complexity involved with organising such a vast workforce, emergent colony level behaviours such as colony construction or brood care occur in the absence of any centralised control. Instead individuals organise themselves within a complex and plastic work environment according to a simple set of rules, relying on local information and independent decision making without any knowledge of a global goal [98], [125], [126].

Within colonies, individuals exhibit spatial fidelity in zones dependent on their task [127], [128]. In turn this gives rise to segregation within the social environment, whereby ants in close proximity to each other are more likely to interact than with ants performing different, spatially discrete tasks. As physical interaction is important for the exchange of information it stands to reason that the social network, reflecting differences in spatial fidelity and organisation, highly correlates with division of labour in ant colonies [100], [129]. Consequently, the location of task-specific stimuli, such as the location of brood, will influence the spatial distribution of workers and will regulate the colony social network, which may, in turn, influence division of labour.

The location of brood within ant colonies is dependent on background ambient temperature [130], which may fluctuate with daily and seasonal changes in solar radiation [131]. Ants demonstrate highly sensitive thermosensation and the ability to adapt to background ambient temperatures [132] using sensory organs present in their antennae. A physical temperature sensor structure was first identified and described for the ant Camponotus rufipes [133] which described the existence of both background ambient temperature detection over a wide range (14^{o}C), and a second, precise thermal measurement within a narrow band (1.6^{o}C)

that matched the temperature preference for the brood, which suggests that ants should be capable of quick and accurate detection of the optimal temperature for brood and laboratory studies have demonstrated that this is the case, with ants responding to thermal gradients by re-allocating brood in accordance with their temperature preference [134]. Heyman et al. investigated how ants plan their trajectory to transport brood inside nest. They have found that ants evaluate multiple factors, such as self-referenced memory of multiple locations and chemical cues, to transport the brood. It has been showed that the ants reevaluate the importance of the information to type as a response to the information changes [135]. We aim to utilize the thermo-sensitive abilities of Camponotus floridanus to apply thermal signals with high temporal and spatial resolution, within an experimental setting, to investigate the process and mechanisms of adaptive self-organisation in ant colonies.

5.2 Automated tracking system

The identity, orientation and location of each ant were recorded twice a second using the automated ant tracking system developed by Mersch et al., 2013 [100]. In addition, modifications made by Stroeymeyt et al., 2018 [136] to the lighting system were also utilised as they provided enhanced tag detection (Personal observation). This system detects fiducial markers from the ARTag library (0.8mm tags; [137]) which were printed on paper and cut to size. As the weight of the smallest worker in our study was 4.03mg and the weight of each tag was 0.34mg, the approximate load was at most 8.4 % of body weight. As ants are known to carry loads significantly heavier than their own body weight [138] this should not encumber the ants. Additionally behavioural analysis in previous studies utilising the same tag application [100], [129], [136] finds that tagged ants exhibit behaviour typical of untagged ants and this study concurs with those findings.

Within the tracking systems ants had access to a nest and foraging area. The floor of the nest, on top of which walls were placed, is creating a rectangular nest area. These walls were coated with fluon to prevent ants from escaping. This nest area was then connected via an opaque

tunnel to a foraging arena of the same dimensions but with a floor consisting of a cut sheet of foam (Kramer-Krieg SA, Switzerland) as used in Mersch et al., 2013 [100]. Within the foraging arena ants were provided ad libitum with water and 10 % sugar-water though cotton-stoppered plastic reservoirs and artificial ant diet provided on a small plastic tray. Reservoirs were refilled every other day at 17:00 UTC throughout the experiment. During preliminary trials it was found that brood transporters would also transfer flies that were provided as food and that were deposited near the brood pile. As this occasionally resulted in erroneous records of brood transport when observed flies were not included as a food source for this experiment.

As an integrated feature to the camera recording, the tracking PCB has the light condition control in the tracking box. It can create the daylight conditions or infrared light for the individual ant recognition during the night. The tracking PCB also manages the thermal and humidity conditions of the air in the tracking box depending on the experimental requirements. These values are measured via temperature and humidity sensors located on the tracking PCB. If the tracking PCB detects low humidity values through the sensor, it commands to pump humified air through the fan in the back. In parallel, the temperature is regulated via resistive heat generators located at the rear inside of the tracking box.

The individual ants is recognized via fiducial identification labels by the camera. Figure 5.1 shows a screenshot from an experiment where we have stimulated the ant colony to transport the broods to top stripe. The barcodes are depicted on two ants who are physically interacting (dashed box in Figure 5.1). The tracking system records the spatial coordinates at every time point and identify the interactions between the ants.

5.3 Temperature regulation system

We developed a robotic temperature regulation system (ThermoReg) that allows us, for the first time, to directly control the position of the brood pile within an ant colony by subtly altering fine thermal gradients under the nest surface floor, while simultaneously, gathering precise behavioural data for all individuals within the colony using automated visual tracking. The

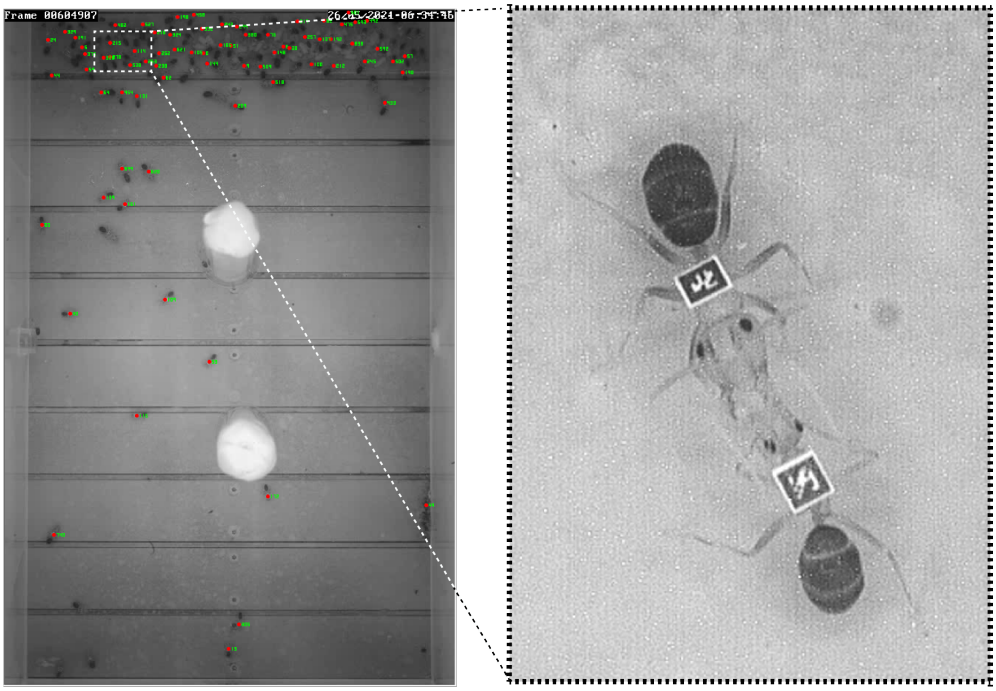

Figure 5.1 – A screen shot from an experiment. The ants reside on the nest comprising of 10 stripes, separated with insulating plastic rods. Two white objects in the nest are towers for additional water supply. The green numbers are the ID numbers of the ants detected by the camera. Ants in the white dashed box is shown with their identification tags.

complete platform consists of tracking box out of insulating foam material, a PCB including light sources, camera, air temperature control and the temperature regulation system that is located underneath of the tracking box as it stands for nest surface (Figure 5.2a). Firm insulation is achieved to prevent any disturbance from outside (Figure 5.2b-c). While the experiment room (outside of the tracking box) is kept at 19 degrees, the tracking box conserves the programmed thermal conditions inside the box. The tracking PCB controls the camera recording of the individual ants through host computer interface. The recording command is sent via the computer, and the tracking PCB collects the data and saves as video files in every 0.5 seconds into the host computer.

The interface is made out of aluminum stripes mounted on top of 60 Peltier elements patterned as a 6 x 10 matrix. By serially connecting 6 Peltier elements that are located underneath each stripe, we created 10 independently addressable zones (Figure 5.3). The Peltier elements are located on top of the aluminum heat sink, which has engraved cooling channels and

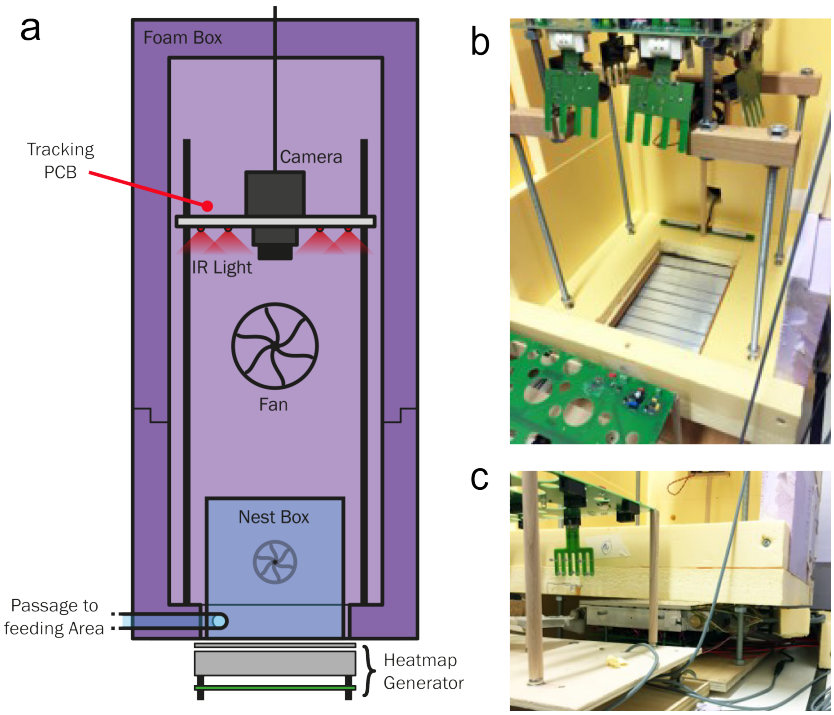

Figure 5.2 – Experimental setup to manipulate the floor temperature. a) Ant incubation box, out of hard foam, is shown along with the ThermoReg. Fans are used for climate control in the box. Camera is located on the top inside the box, embedded to a PCB which controls the illumination and thermal properties of the air in the box. The passage to feeding area is displayed on the left bottom side. The feeding area is also covered with the same incubation box, including camera, thermal and illumination control. b) A photo of the inside of the incubation box without the nest box. 10 stripes, which generates independent temperatures, is shown. c) The ThermoReg, the surface where ants reside as their nest, is integrated from the bottom of the incubation box.

integrated PCB. PCB controls the current sent to the Peltier elements. The cooling channels are fed by a cooling pump, which has capacity to pump the water up to the heat sink while thermally regulating the water according to the programmed temperature.

Peltier elements (CP60240, CUI Inc) work as a heat pump using the Peltier effect. When an electron passes through an element it has to change its energetic level at each junction of the different metallic conductors and semiconductors, which as a consequence releases or absorbs heat (Figure 5.4).

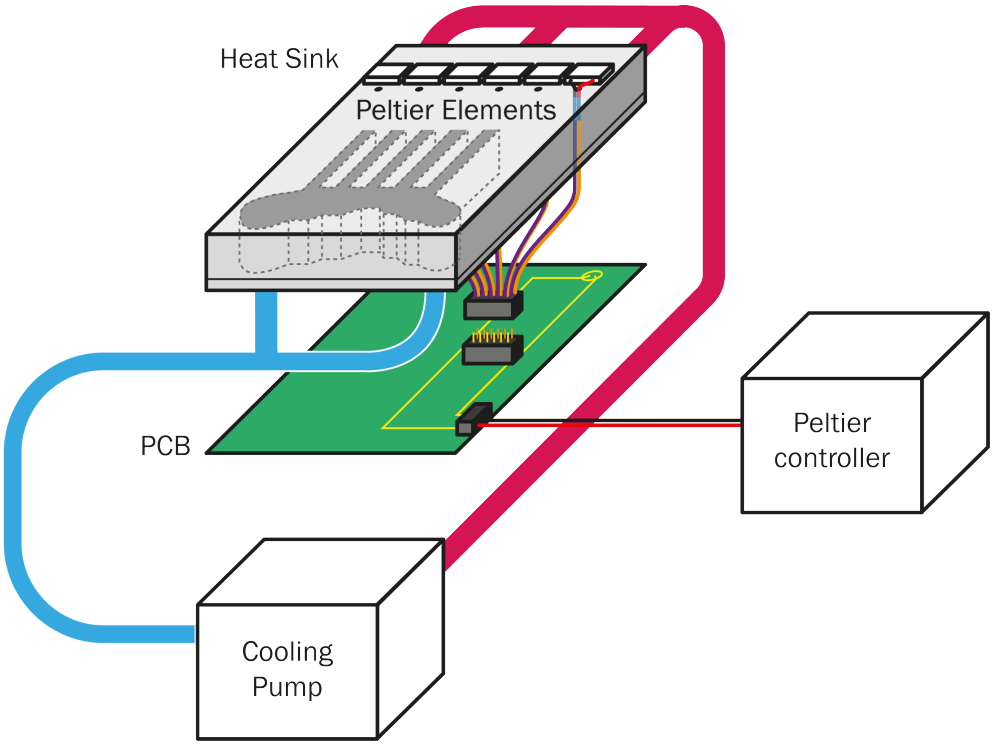

Figure 5.3 – The schematic of heatmap generator. There are six peltier elements underneath each of ten aluminum stripes. The peltier elements are connected to the peltier controllers through custom designed PCB. There is a cooling channel system inside the heat sink. A cooling pump is feeding the heat sink with cold water via two inlets and the warmed water is returned via three outlets back to the cooling pump.

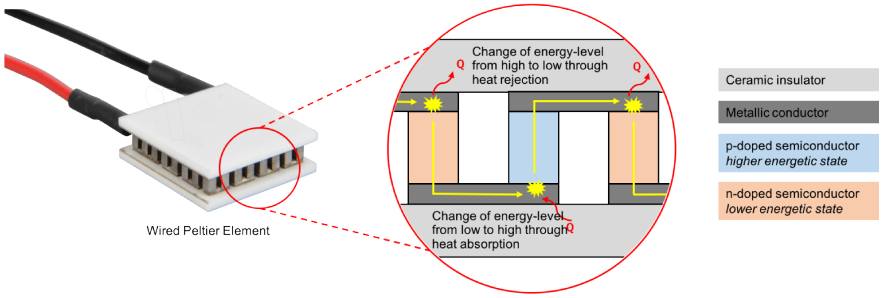

Figure 5.4 – Working principle of the peltier element.

The heat flux $\dot{Q}_{Peltier}$ passed through an element due to the Peltier effect can be expressed as:

$$\dot{\boldsymbol{Q}}_{\boldsymbol{Peltier}} = (\Pi_A - \Pi_B) I \tag{5.1}$$

where $\Pi_{A,B}$ are the Peltier coefficients of the conductors and I the current passed through the

element. The heat flux direction is invertible by inversing the current as it is proportional to I. To find the equation for the overall heat flux from the cold to the hot side we consider the contributions of Joule heating $\dot{Q}_{Joule} = RI^2$ and Fourier's law $\dot{Q}_{Fourier} = -\kappa \nabla T$ as well. The overall equation therefore is:

$$\dot{\boldsymbol{Q}}_{\boldsymbol{cold \rightarrow hot}} = \dot{Q}_{Peltier} + \frac{1}{2}\dot{Q}_{Joule} - \dot{Q}_{Fourier} = (\Pi_A - \Pi_B) I + + \frac{1}{2} R I^2 - \kappa \frac{T_{hot} - T_{cold}}{e} \tag{5.2}$$

where T_{hot}, T_{cold} are the temperatures of the hot and cold side of the Peltier element and the factor of one half in front of the Joule heating term is due to its symmetric dissipation. This symmetric dissipation is also the reason why we need a heat sink under the Peltier elements even if we want to heat the nest. Indeed, the heat transferred from one side to the other by the Peltier effect is smaller than the heat produced by Joule heating. Peltier elements can generate up to $75°C$ temperature difference between heat sink and nest surface.

A total of 5 PID control units together regulate the current that flow through clustered Peltier elements (Figure 5.5a). They are located outside of the tracking box. Each controller (TEC-1122-SV, Meerstetter Engineering) generates signals to control two independent stripes. The controllers are connected to Peltier element through the PCB underneath the heatsink. 2 temperature sensors located in the ThermoReg provide feedback to the controller. Temperature can be modified with an increment of as small as $0.01°C$. This value defines the precision of the control scheme.

The cooling water is circulated by a refrigerated pump (Arctic A10, ThermoFisher Scientific). The circulated cold water absorbs the heat generated by the Peltier elements (Figure 5.5b). The pumping unit is programmable and it automatically adjusts the water temperature and circulates the water. Circulation of stable cooling water prevents any accumulation of heat in the heat sink, which may cause failure of the Peltier elements. As an important remark, experiments can last for several weeks.

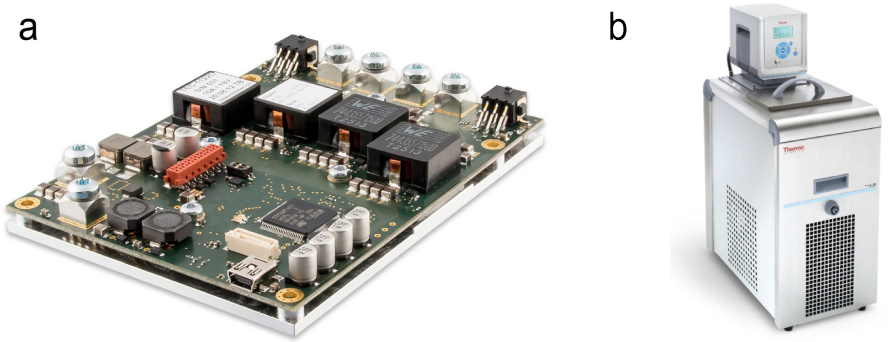

Figure 5.5 – Peltier element controller and refrigerated circulator. a) The controllers are adjusting the current to control the commanded temperature. There are two different sensors connected to the Peltier controller to have feedback temperature. b) The refrigerated circulator has capacity to pump the water to heatmap generator and also adjust the temperature of the water.

Heatsink Design

The ThermoReg consists of multiple layers of hardware. The top layer consists of ten aluminum stripes (276 x 23.5 x 5 mm) and insulating thin stripes (243 x 5 x 2 mm), which serve as the nest floor (Figure 5.6a). The top side of the aluminum stripes are painted with matte yellow color to maximize the detection quality of the ID labels. The stripes are fixed to the heatsink with insulating screws from two edges. The aluminum stripes includes two layers (Figure 5.6b). The object sensor is attached to the bottom surface of the upper layer of the aluminum stripes with a thermally conductive glue. This sensor reports the temperature of the respective stripe to the control unit. Thermally conductive gel prevents losses associated with the heat transfer (Figure 5.6c and Figure 5.8).

The heatsink is manufactured by milling an aluminum block. The top layer is thicker (400 x 276 x 30 mm) and contains the grooves for the 60 Peltier elements, cable passages, and the cooling channels (Figure 5.7a). The bottom layer is thinner (400 x 276 x 10 mm) and works as a lid to cooling channels (Figure 5.7b). To block any cooling water leakage, O-rings are used at every cable passage between two layers of heatsink (Figure 5.7c).

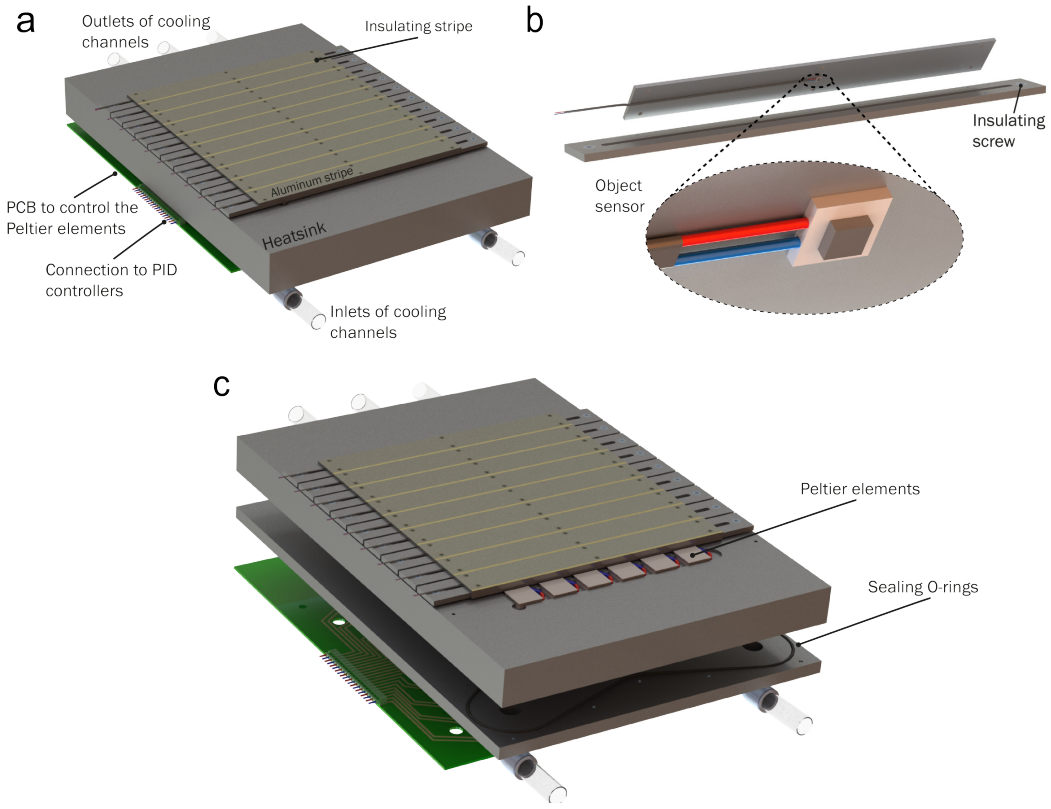

Figure 5.6 – The heatsink. a) The heatmap generator consists of 10 stripes painted with pale yellow color to provide high quality tag detection. The main body of the generator is out of aluminum with the internal cooling channels. The cooling channels are fed with two inlets and three outlets, connected to the cooling pump. PCB underneath the heat sink is to connect the Peltier elements to the Peltier element controllers. b) The aluminum stripe consists of two thin layers and the object sensor is fixed in-between layers with conductive glue. Object sensor is connected to the Peltier element controller. c) The layers of the heat map generator. One of the ten stripes are removed to show six Peltier elements underneath. The heat sink is out of two layers.

The electrical circuitry is located underneath the heatsink via grooved legs. PCB includes 10 serially connected circuits for each aluminum stripe. The serial circuits are completed with Peltier elements located on top of the heatsink.

Design and optimization of the cooling channels

60 Peltier elements generates significant amount of heat to be extracted via heatsink. Accumulation of heat might cause failure of the Peltier elements. Moreover, the temperature distribution inside the cooling water must be homogeneous. Homogeneity will ensure that

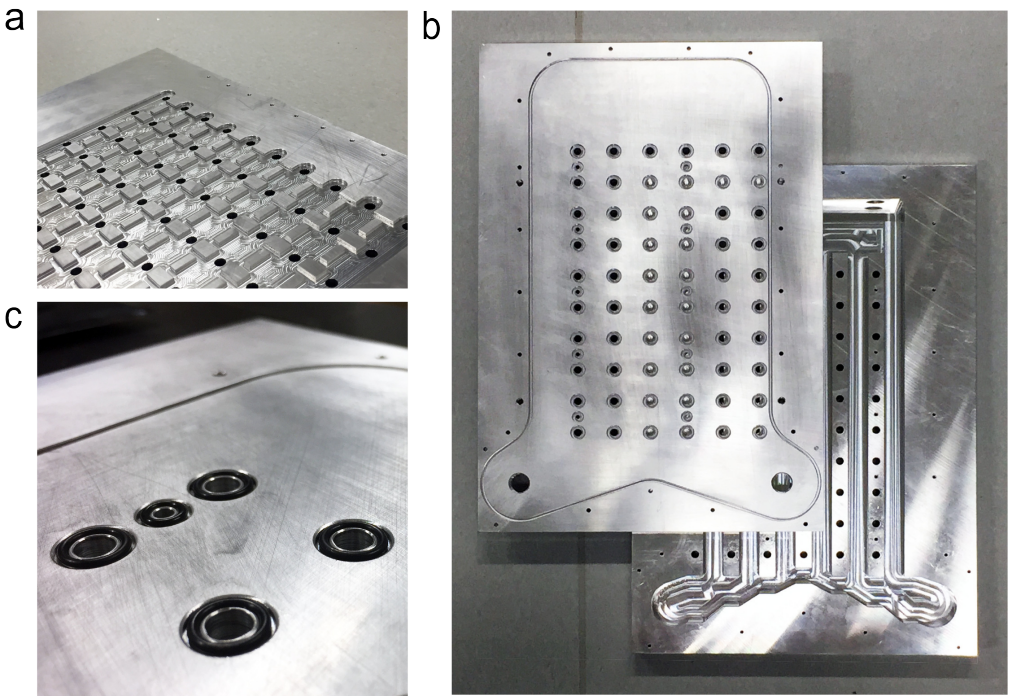

Figure 5.7 – Manufacturing of the heat sink. a) CNC milling is used as manufacturing method and the grooves for the peltier elements are shown. The holes are created as the passage of the cables of the peltier elements to PCB. b) Interior surface of the heat sink is shown. Cooling channels are designed to homogenously distribute the water to each line. c) O-Rings are used to avoid the cooling water leakages to the electronic parts.

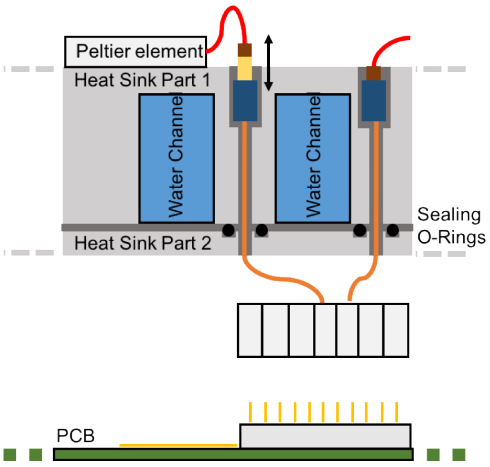

Figure 5.8 – A cross section of the heat map generator is shown. Cabling of the Peltier elements are passing through body in-between cooling channels. To prevent any water leakage, o-ring sealings are used in-between two layers of the heat sink. The cabling of the Peltier elements are collected on the connector and connected to the PCB, which is connected to the Peltier controllers.

Peltier elements show expected performance and we can achieve homogeneous temperature over each aluminum stripe. One of solutions is to pass the cooling channel parallel to the heating channels (Figure 5.9a). As the cooling water is warming up due to absorption of heat from the Peltier elements, they would not perform the same way. To overcome this challenge, we decided to pass the cooling channels orthogonal to the aluminum stripes (Figure 5.9b). Even though the cooling water is not same underneath different Peltier channels, each Peltier channel can be calibrated regarding to the corresponding cooling water temperature.

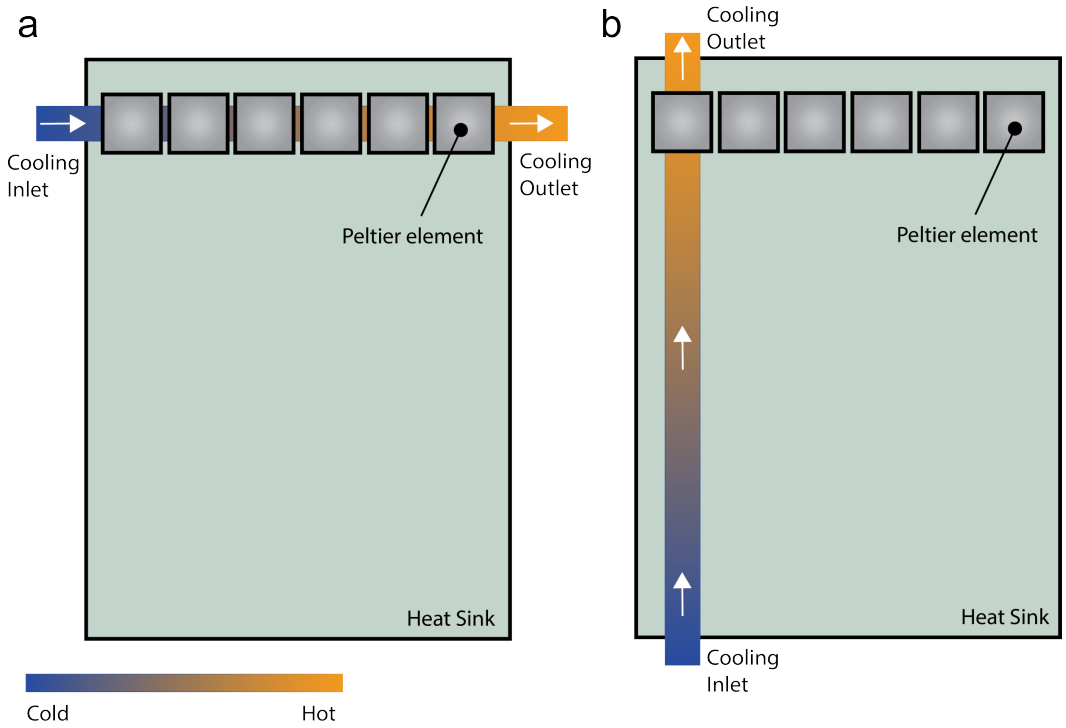

Figure 5.9 – Cooling channel orientation effect on a Peltier channel.a) A cooling channel, passing parallel to the Peltier channel, is depicted. This design cause inhomogeneous cooling under serially connected Peltier channel. As the Peltier elements of the channel are serially connected, it is impossible to regulate the Peltier elements individually. b) A cooling channel, passing orthogonal to the Peltier channel, is depicted. Even though the cooling water temperature is changing as it progress inside the device, each Peltier channel experience similar heat absorption, which makes the cooling performance homogeneous and sustainable.

After determining the orientation of the channels, we have focused on the inlet and outlet designs. One strategy is to locate the inlet orthogonal to the horizontal surface of the cooling pad. Another strategy is to locate the inlet lateral to horizontal surface of the cooling pad with a ladder-like structure towards the last cooling channel. By adapting and merging two strategies,

we have designed an orthogonal inlet with ladder-like structure and lateral outlet from the side. This configuration did not generate homogeneous velocity in the cooling channels (Figure 5.10a). We have iterated the design and changed the outlet to be parallel to the cooling channels (Figure 5.10b). After an unsatisfying result, we have designed two symmetrical lateral inlet with ladder-like structure in addition to the three outlets, which are parallel to cooling channels. Furthermore, we increased the number of channels to eight (Figure 5.10c). This strategy has improved the homogeneity, and after several more design iterations along these lines, we came up with the following configuration shown in Figure 5.10d. This final version provides a homogeneous distribution of cooling water velocity throughout the heat sink.

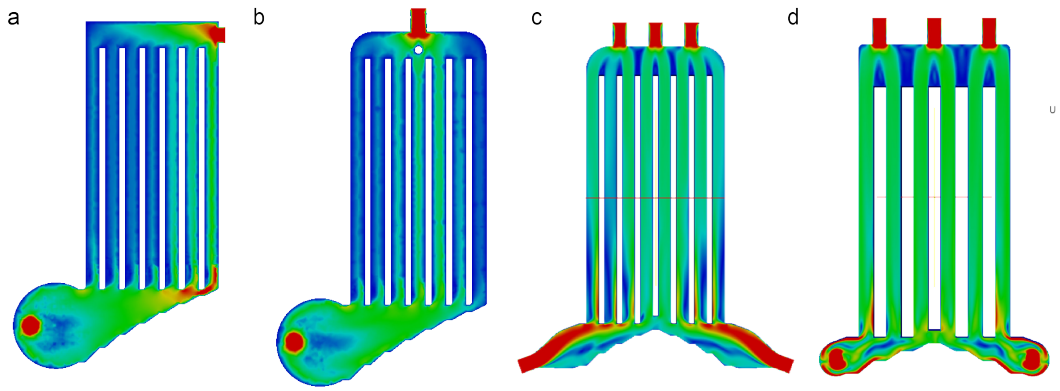

Figure 5.10 – Optimization iterations of cooling channel

We chose a rectangular and not circular section for the water channels to enhance the heat exchange from the Peltier element to the water. Rectangular geometry requires less aluminum material in-between and a bigger exchange surface. Moreover, rectangular channels are easier to manufacture via milling. All the numerical simulations were run on SimScale, a cloud based finite element simulation software with the parameters and boundary conditions shown in Table 5.1.

Material	Water
Viscosity Model	Newtonian
Turbulence Model	k-omega SST
Steady-state or transient	Steady-state (after 1000s)
Wall boundary condition	No slip
Inlet boundary condition	$0.0004 m^3/s$
Outlet boundary condition	$0.0004 m^3/s$
Post-processing	cut through middle (velocity scale: 0 - 0.8 m/s)

Table 5.1 – Finite element simulation parameters and boundary conditions for cooling channel optimization

5.4 Results

5.4.1 Detecting the preference of the ant colony for brood translocation

ThermoReg system gave us a unique opportunity to selectively change the temperature of different regions on the nest arena. On one side, the temperature on the nest floor can be modulated within seconds. On the other side, we can maintain the same temperature over weeks. In this work, we focused on the temperature levels at which the colony decides to transport their brood to a different and favorable location. This translocation event is well-defined and allow us to perform quantitative analysis on colony behavior. All replicates were performed using colonies of the Florida carpenter ant Camponotus floridanus. Incipient colonies were collected from Upper Sugarloaf Key (24.6583º N, 81.5271º W) and Long Key (24.4859º N, 80.4926º), Florida Keys, USA during April, 2017. Colonies were reared at constant temperature (26ºC) and humidity (65 %) and a 12h:12h L:D cycle. Water was provided ad libitum and they were fed once a week with a reservoir of 10 % sugar water, flies, and an artificial ant diet [139].

To identify what temperature the ants would prefer to keep their brood, we set a temperature gradient on the nest arena prior to introducing the colony and the brood into the nest arena. The lowest temperature was set to 21ºC at the bottom of the nest and to 30ºC at the top of the nest, respectively. In addition to the recordings from the on-board thermocouples, the temperature values were measured with sensitive instruments before running experiments to

ensure precision. We performed 3 different experiments with the same colony. Ants deployed their brood at 27ºC, 28ºC, 29ºC at different trials (Figure 5.11). We maintained the same temperature profile for 12 hours. We did not observe any change further brood transport event after they reach the steady state. We chose 27ºC as the preferred temperature value for the remaining experiments.

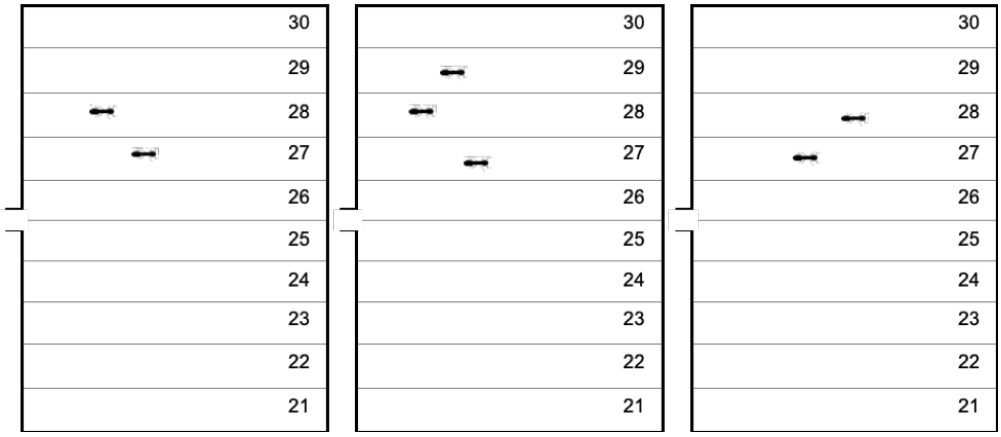

Figure 5.11 – The position of the brood at the equilibrium state on a nest floor with graded temperature profile. Ant symbols depict the individual ants and brood piles residing in nest.

5.4.2 Dynamics of brood transport

Next, we periodically regulated temperature of the floor so that the ant colony is stimulated to transport their brood twice a day over a week. For each experimental replicate, 400 workers were selected from a colony with 200 foragers taken from the foraging arena and 200 nurses taken from inside the nest surrounding the queen. These workers were then assigned randomly between two groups (henceforth sub-colonies) each comprising 100 foragers and 100 nurses. One of these sub-colonies was designated as control and the other as treatment. After tagging, both sub-colonies were transferred into an experimental arena along with 100 brood (comprising 50 larvae and 50 pupae; eggs were excluded as their small size makes their transport by a worker difficult to detect) inside a tracking system [100] comprising a nest and foraging area. Both were maintained at 65% humidity however the nest remained in darkness throughout the experiment (illumination for tracking was provided by timed infra-red lighting) whereas the foraging arena experienced a day-night cycle of 12h:12h (06:00 to 18:00 UTC,

replicating the husbandry conditions the ants were reared in.

Before the beginning of each experiment, the surface of the nest arena was cleaned with ethanol to remove any chemical residue such as pheromones. The top stripe was set to 27°C, and the rest of the stripes were set to 23°C. In all cases a 0.5°C/s temperature change ramp was utilised. We refer to the low temperature as as the background temperature. Ants were expected to avoid lower temperature and transport the brood to the higher temperature, which was found to be their preference for the brood. The experiment started with the initiation period where the colony was given 20 hours to translocate the brood to the top stripe of the nest arena (Figure 5.12a). On the first day of the experiment, the temperature of the bottom stripe was raised to 27°C while the temperature of the top stripe was reduced to 23°C. The brood translocation started 15.14 ± 15.18 min (n=6, N=36) after the temperature change and ended within 74.46 ± 33.91 min (n=6, N=36).

Figure 5.12b shows a schematic of an instant of brood translocation. The image shows two different ants that grabbed the brood with their mouth during brood transport(see **Movie** to watch an example of brood translocation where the preferable stripe is randomly changed). This is the primary mechanism by which the ants carried their brood. Therefore, they must make physical contact with the brood in a certain pose in order to initiate the transport event. A representative trajectory of transporter ants is shown in Figure 5.12c. In the evening event, the conditions were switched so that the brood was transported from the bottom stripe to the top stripe.

One of the important findings of these experiments is that only a subset of ant colony participates in the transport process. The average number of ants involved the whole transport experiment was measured as 20.79 for colony 1 and 13.86 for colony 2 (Figure 5.13). This data indicates that the number of ants that transport brood depend on the composition of the colony. Note that the total number of ants and brood items were identical. If we process all the data, the average number of transporter ants per brood translocation event is 17 ± 5.26 (n=6, N=36). We did not observe a progressive change in the number of ants getting involved

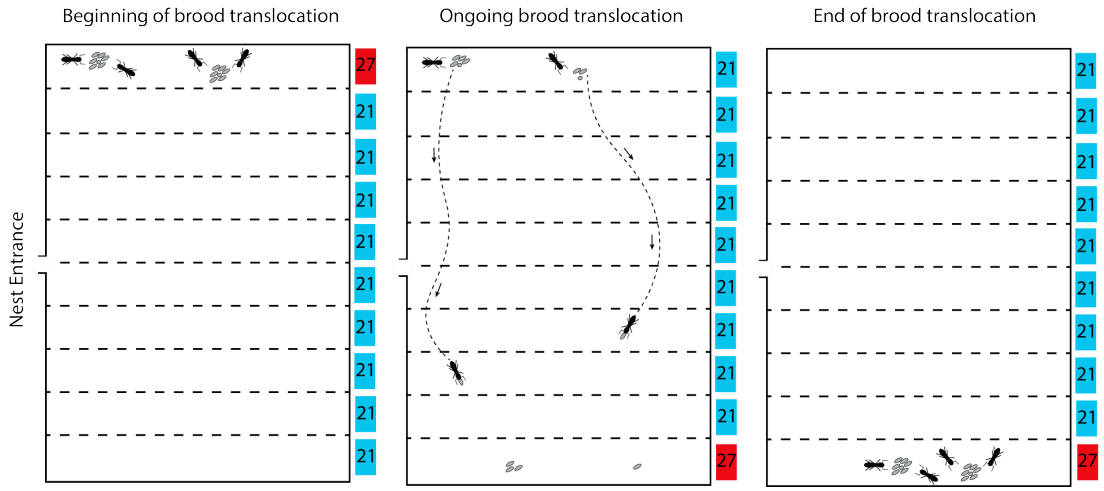

Figure 5.12 – Three critical steps of brood translocation. Brood translocation experiment is started by locating the ants to foraging arena and setting the preferable temperature to top stripe of the nest arena while the rest unprofitably cold. 12 hours of period is attributed to the ant colony to relocate the brood to preferable warm spot inside the nest arena. Gray ellipse structures represent the brood and four ants represent the whole group of ants in the colony. To start the brood translocation, the warm stripe is switched to bottom stripe of the nest arena. This thermal signal stimulates the ants to transport the brood to preferable warm spot. Two different ants, who transport the brood, is depicted in the middle representation. When all the brood is transported, ant colony settle the brood to the new preferable spot in the nest arena.

with the brood transport. Therefore, there is no evidence that indicates a learning curve or optimization of resources.

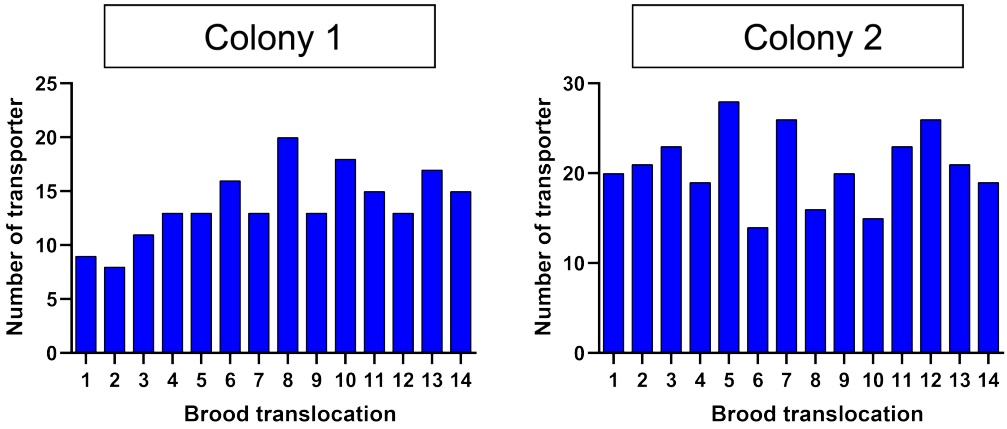

Figure 5.13 – Number of transporters throughout consecutive brood translocation events from two different colonies. In each experiment, 14 brood translocations are triggered via thermal stimulation of robotic heatmap generator. Number of transporters for two different colonies are represented throughout 14 brood translocations.

We asked whether an ant that participated to a transport event consistently performed brood transport in other trials. Figure 5.14 shows the results of three consecutive brood translocation events. The individual ants are depicted as circles with ID numbers so that the identity of the any is revealed. Notably, most of the ants did not attend all the brood translocation events. We occasionally see ants that participated in 2 out of 3 trials. For example, Ant8 carried brood in the first two trials and Ant4 carried brood during the last two trials. Figure 5.15 shows the number of times an individual transporter carried brood over many trials. The frequency at which an ant will contribute to transport greatly varies within a colony. Taken together, there is a subset of ants in the colony who participate in brood transport, and different ants may get involved in the process in different trials.

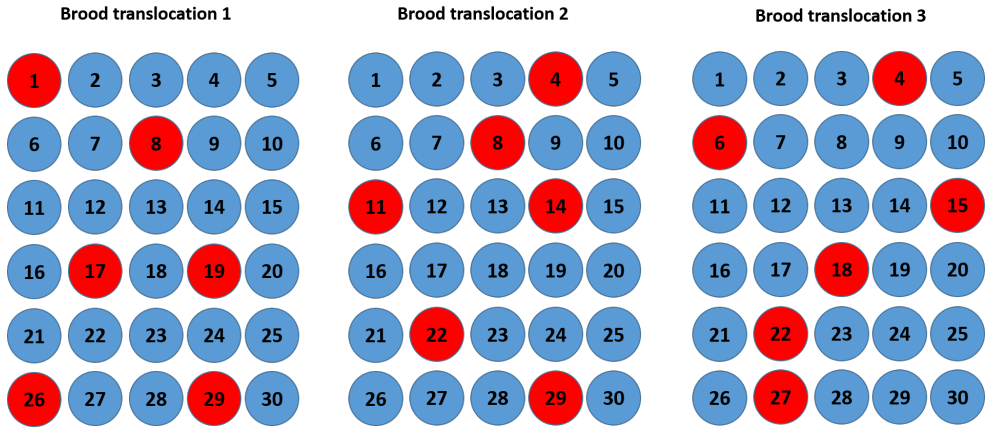

Figure 5.14 – Schematic of attendance of ants to the brood translocation throughout three brood translocations. The colony is presumed to have 30 ants in this schematic. The number of the circles show the IDs of the individual ants. The ants who attends to brood translocation is depicted with red circles while the ones who do not attend to brood translocation is showed with blue circles.

We next counted how many brood an individual carries at each trial. Figure 5.16 presents the data of attendance over 14 independent trials. Ant1 carried brood only during the 11th trial, and transported only one brood. On the other hand, Ant2 attended 10 trials, and transported multiple brood items in each trial. We show only four ants in the graph for clarity. The same variation has been observed for all ants. Figure 5.17 shows that most ants that are involved in the transport process transport only one brood. On the other hand, a single ants can carry as many as 24 brood items in a given trial.

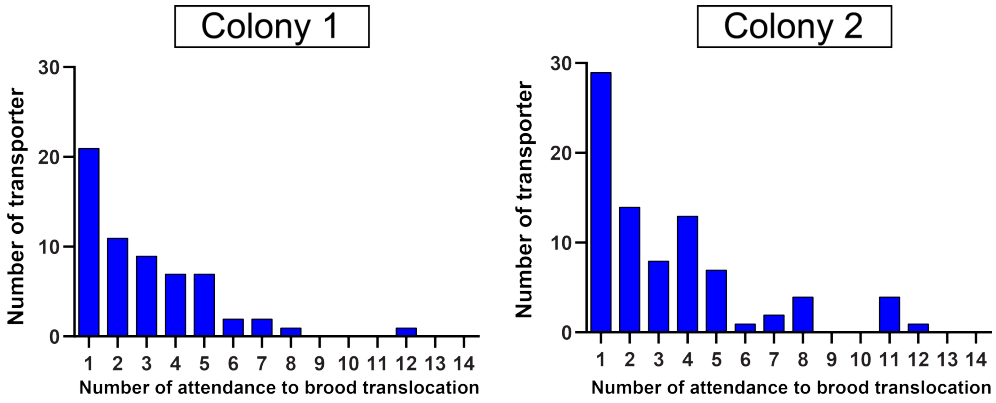

Figure 5.15 – Frequency of the attendance to brood translocation in two different colonies. Frequency is presented for two different colonies.

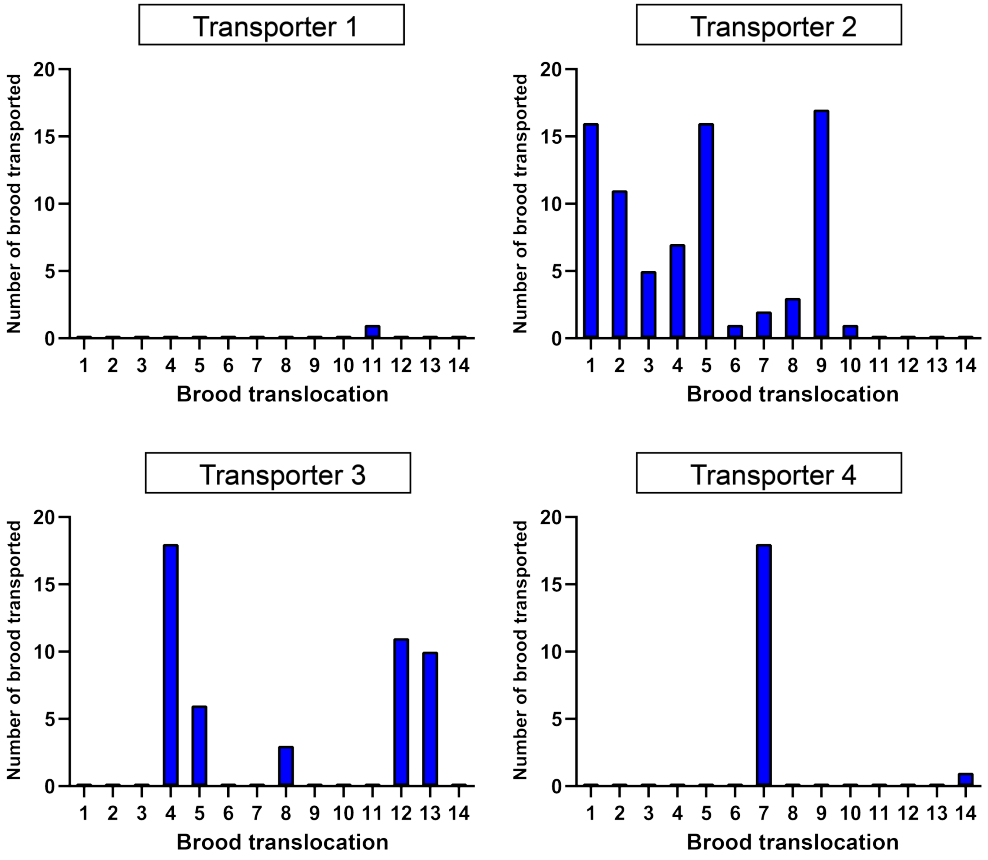

Figure 5.16 – Attendance frequency and the number of broods transported by four transporter ants. The number of broods for four transporters is presented. The data also demonstrates the frequency of attendance to 14 brood translocation events.

5.4.3 First comers are more likely to transport more brood items

To learn more about the dynamics of brood transport, we have asked the following question.

Does the order at which ants start to carry brood play a role in the number of brood they

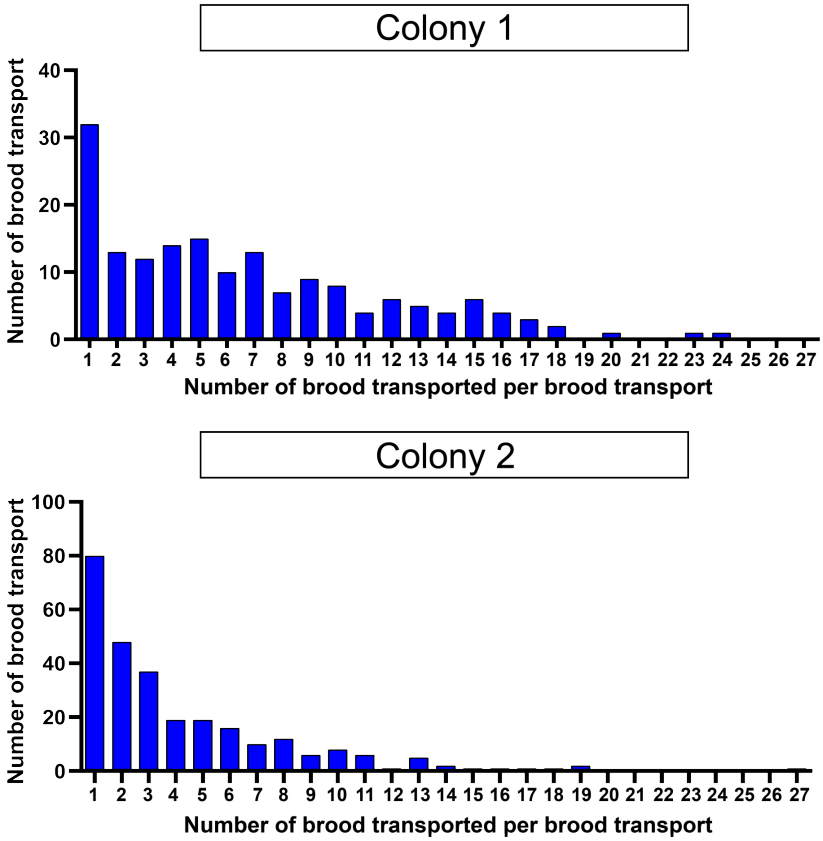

Figure 5.17 – The number of brood transport versus the number of broods transported in two different colonies.

transport? The result showed that the number of brood items transported by a given ant depends on when they decide to participate in the process (Figure 5.18). There are multiple reasons behind this trend. First, the number of brood an any can carry may depend on capacity. The more talented or motivated an ant is the earlier she starts to move brood, and as a result, the more brood she transports. The second explanation is that it is all about timing. All ants that participate in the transport process are equally capable of moving brood but, for some reason, they are not activated at the same time. The number of brood to be transported decreases over time, which gives the late comers less number of items to transport.

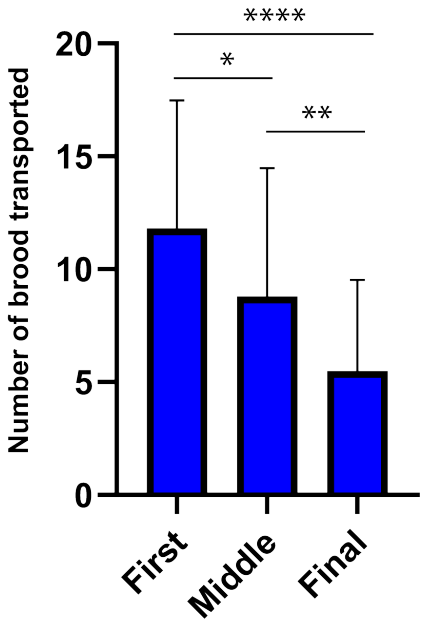

Figure 5.18 – Number of brood transported by first, middle, and final transporter.

5.5 Targeted removal of brood transporters

We designed an experiment where we sequentially remove ants from the colony without disrupting their state. As before, for each experimental replicate, 400 workers were selected from a colony with 200 foragers taken from the foraging arena and 200 nurses taken from inside the nest surrounding the queen. These workers were then assigned randomly between two groups (henceforth sub-colonies) each comprising 100 foragers and 100 nurses. One of these sub-colonies was designated as control and the other as treatment. In all replicates the initial temperature setup was 27°C at the top stripe and 23°C at the rest of the nest which in all cases initialised the brood at top stripe within the experimental arena.

Ants were allowed to acclimate to the new experimental setup for one night after which we started automated tracking until the end of the experiment (a total of 13 days). Each day at 07:00 UTC the temperature profile of the experimental arena was altered such that the top stripe was changed from 27°C to 23°C and the bottom stripe was changed from 23°C to 27°C. For the following 160 minutes (until 09:30 UTC) the ants were remotely observed using

peer-to-peer screen sharing accessing the tracking feed in real-time, and all brood transport events were recorded. If an ant picked up a brood item and transferred it from its current location at the top stripe to bottom stripe it was scored as a successful brood transport and the ants individual ID and frame reference for the brood transport was recorded. At 11:00 UTC the temperature profile was again changed such that the top stripe returned to 27°C and bottom stripe returned to 23°C. Once again, ants were remotely observed for 160 minutes, and brood transport was recorded as before with ants transporting the brood from bottom stripe to top stripe being scored as successful brood transports.

At 15:00 UTC ants identified as brood transporters in the treatment subcolony were gently collected from the experimental arena using a pair of featherweight entomology forceps having first removed the front cover of the tracking system. To minimise light disturbance to the colony, removal was performed with the assistance of a low level red-light headtorch. As a human observer is unable to decipher the 0.8mm ARTags without computer aid, a remote feed of the tracking system was streamed to an iPhone in real-time to target the ants identified for removal. In the control subcolony an equal number of ants were also removed from the experimental arena by randomly selecting tags from a list excluding brood transporters. Ants that were removed were then transferred to one of two husbandry boxes, one for the treatment subcolony and one for the control. This procedure was repeated consecutively over 10 days. On the tenth day, rather than removing ants, all ants retained in husbandry boxes up to this point were returned to their original respective experimental arena. For the next three days the process described above was repeated however ants were no longer removed in the afternoon.

5.5.1 Task allocation in the context of brood transport

To assess the statistical significance of the effect of removal (treatment/control) over time (days 1 – 10) on the time taken to move brood, a two-way repeat measures analysis of variance model was constructed. Figure 5.19 illustrates the average time taken to move half the brood, per treatment, day for each of the six replicates.

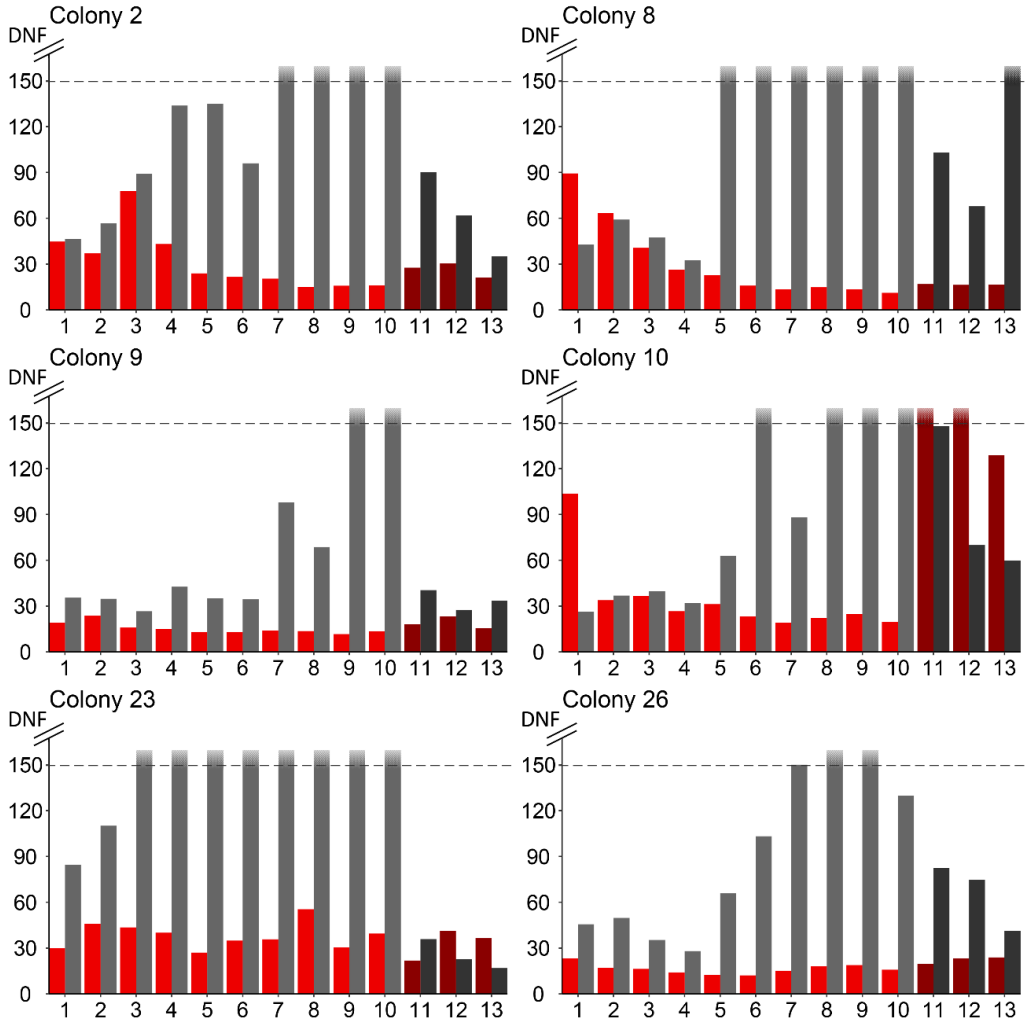

Figure 5.19 – The average time taken to move half the brood per subcolony for each day of the experiment. The average time taken to move half the brood is on the y-axis and day is on the x-axis. Data for control subcolonies are shown in red, treatment in grey. Data for days 11,12 and 13, following the return of removed ants, are also illustrated with control indicated with dark red and treatment in dark grey. Across all six replicates brood translocation was completely knocked out in treatment subcolonies on days where the bar stretches across the horizontal dashed line. Additionally, brood movement was reinstated in all control subcolonies following the reintroduction of removed brood transporters at the end of day 10.

If brood had not been transported during a brood translocation event the time taken was recorded as 150 minutes, the length of the brood translocation event. All models were written in the Rstudio IDE for R utilising construction syntax available in the package Rstatix. Prior to model selection the effect of observation window was initially included in a 3-way repeat measures analysis of variance and a significant effect was reported ($F(1,5) = 28.546$, $p = 0.003$)

such that brood are moved consistently faster during the second brood translocation event(See Figure 5.20). However, as this effect does not vary significantly per day ($F(9,45) = 1.139$, $p = 0.356$) nor between both treatment and control subcolonies ($F(1,5) = 1.010$, $p = 0.361$), it was excluded from the model and we decided to average the time taken to move brood across both of the two brood translocation events for all subsequent models herein. Regardless of whether the data is averaged across both brood translocation events or not, the results are consistent.

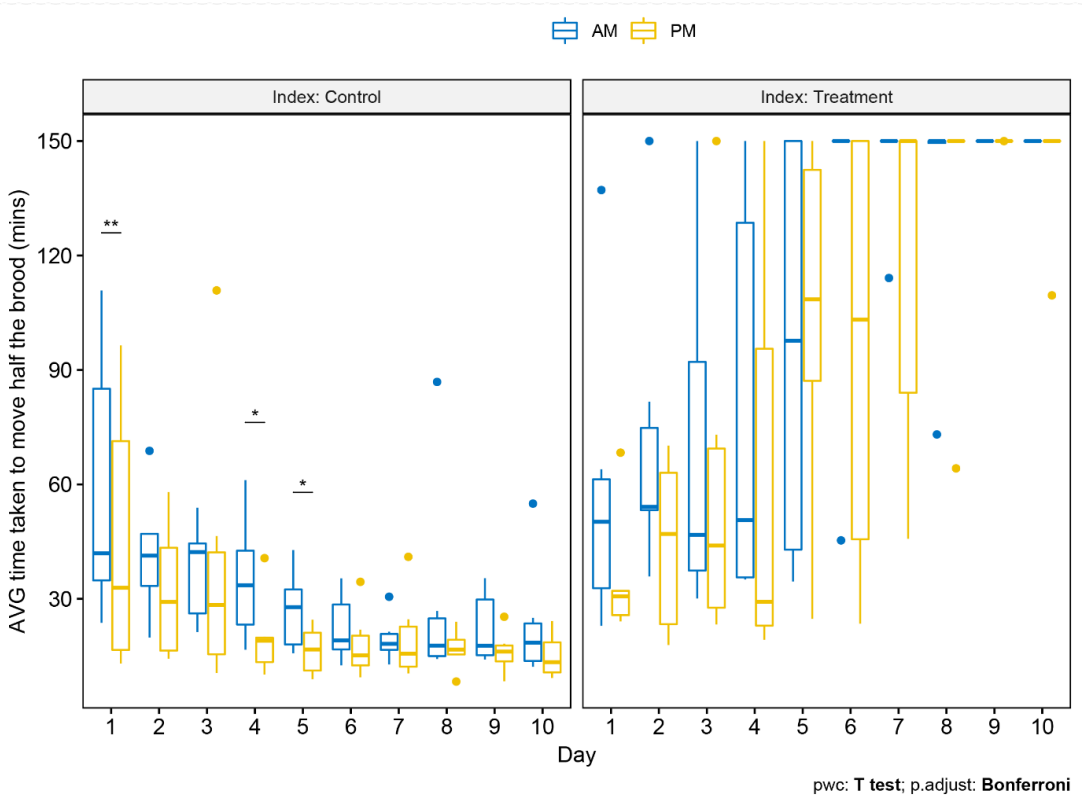

Figure 5.20 – Pairwise comparisons between brood translocation events conducted at 07:00 UTC (blue bars) and 11:00 UTC (yellow bars) between control and treatment.

We found a statistically significant effect of both treatment ($F(1,5) = 96.138$, $p < 0.0001$) and day ($F(9,45) = 5.714$, $p < 0.0001$) and their interaction ($F(9,45) = 13.931$, $p < 0.0001$), with the time taken to move brood diverging significantly between treatment and control by day 6 and remaining significantly different until day 10 (pairwise comparison reported in Table 5.2).

Additionally, there was a significant difference between the average time taken to move brood

Day	**group1**	**group2**	n_1	n_2	**t-statistic**	df	p.adj	Significance
1	Control	Treatment	6	6	0.244355936638121	5	0.817	ns
2	Control	Treatment	6	6	-2.08302108880014	5	0.092	ns
3	Control	Treatment	6	6	-1.61923353905079	5	0.166	ns
4	Control	Treatment	6	6	-2.24708886457623	5	0.074	ns
5	Control	Treatment	6	6	-3.99597858333104	5	0.01	*
6	Control	Treatment	6	6	-5.47646723085114	5	0.003	**
7	Control	Treatment	6	6	-9.54759223967445	5	0.000213	***
8	Control	Treatment	6	6	-8.56385777416739	5	0.000358	***
9	Control	Treatment	6	6	-44.7294160057872	5	1.05e-07	****
10	Control	Treatment	6	6	-25.7767540868814	5	1.64e-06	****

Table 5.2 – Pairwise comparisons with Bonferroni adjustment. The time taken to move brood is not significantly different until day 5, at which point the divergence in time taken to move brood becomes increasingly significant until the end of the experiment. We also repeated this analysis, varying the independent variable to account for the time taken to move all the brood irrespective of the maximal brood moving rate, however the results were consistent

between days 8, 9 and 10 (see Figure 5.21) and days 11, 12 and 13 in the treatment condition ($W = 476.5$, $p < 0.005$, Wilcoxon rank sum test) but not in the control condition ($W = 245$, $p = 0.15$).

5.5.2 Brood transportation dynamics

Within the control condition, 36.9 % of ants moved a brood item at least once and 28 % of ants moved brood more than once. More than half of all brood transports were performed by just 7 % of ants (see Table 5.3) In contrast just 21 % of all ants in the treatment condition moved brood. Subsequent results only pertain to the control condition as ants in the treatment were removed when identified as brood transporters.

Unsurprisingly, the number of brood moved by a transporter over the course of the experiment is correlated with the number of brood translocation events during which the transporter was active ($\beta = 4.647$, $SE = 0.045$, $t(1163) = 103.212$, $p < 0.0001$), however the average number of brood transported by a given ant also increases with the number of observation window that ant was recorded as performing brood movement ($\beta = 0.157$, $SE = 0.017$, $t(429) = 9.407$, $p < 0.0001$; Figure 5.22). In addition, the maximal number of brood transported by a given ant

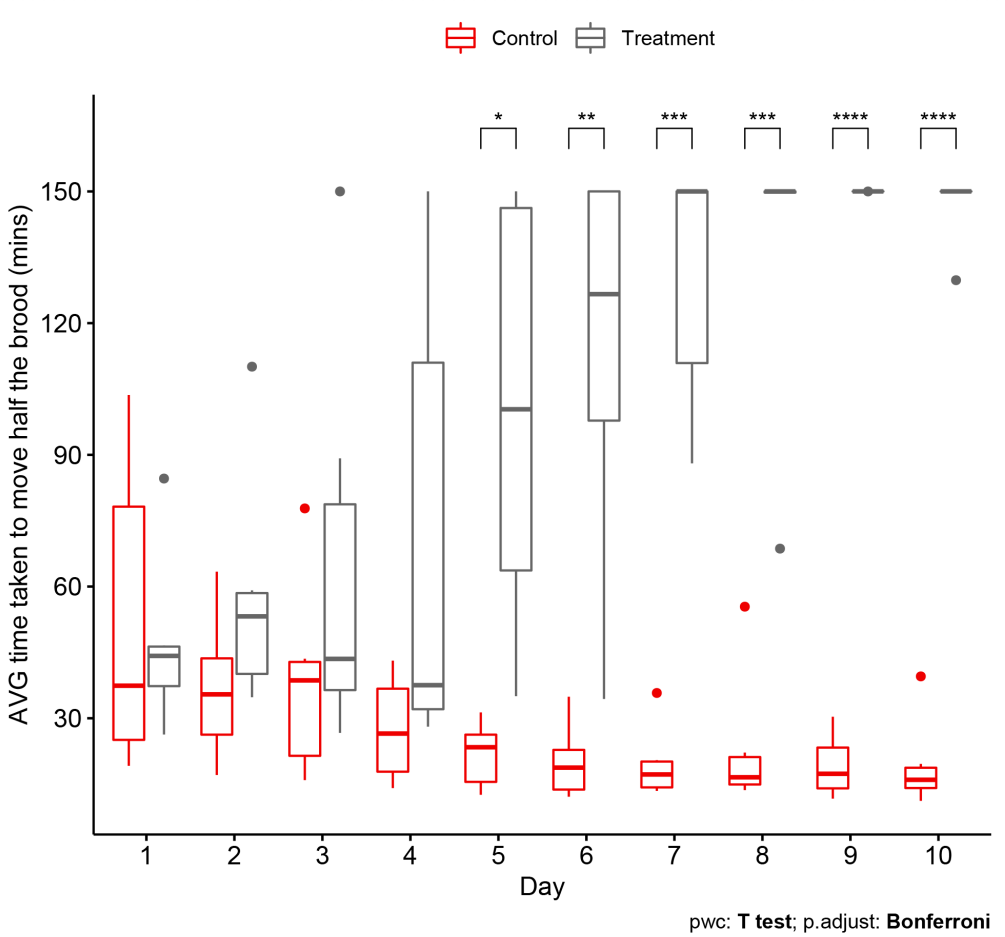

Figure 5.21 – Pairwise comparisons between control and treatment sub-colonies per day for average time taken to move half the brood. Control data in red, and treatment data in grey. Significance denoted by stars at the top of the plot.

was also significantly greater for ants that transported brood more frequently, compared to ants which transported brood infrequently ($\beta = 0.235$, SE = 0.01, $t(429) = 23.31$, $p < 0.0001$; Figure 5.23).

5.5.3 Social Network Analysis

Tracking data collection is automatic, and pipelines for social and spatial analysis are automated and therefore are not subject to bias with regard to the construction of social networks.

Colony identifier	No. of ants performing >50 % total brood transports throughout experiment
2	17
8	18
9	13
10	7
23	21
26	12

Table 5.3 – Number of ants transporting more than half of all recorded brood transport during the 13 days experimental period per colony. This data is only available for the control condition as ants in treatment were removed once brood transport was performed.

For each replicate, the social network of our control and treatment subcolonies was constructed using physical interactions between ants. These interactions were inferred using the geometric algorithm detailed in Mersch et al, 2013 whereby a trapezoid is calculated for each ant using individual measurements of antennae reach and body length [100]. The same procedure for obtaining morphological measurements was used for these measurements. We adopted a conservative approach whereby any overlap between the trapezoids of two individuals was registered as a physical interaction and the length of the interaction was disregarded. As such we do not discriminate between potentially distinct forms of interaction. These contact records were then used to construct a weighted network whereby each ant is designated as a node and each edge represents a single interaction. Social networks were constructed each day over the 13-day experimental period using tracking data spanning the 9-hour period prior to the first temperature change at 7:00 UTC. As such the social network is unaffected by any organisational changes that take place as the result of temperature change which might confound the analysis.

We used facetNet [140] as implemented in Richardson et al, 2021, to evaluate our social network structure as it provides a number of key advantages when analysing dynamic social networks that change over time [129]. First, facetNet uses soft community detection which allows a node to belong to more than one community. Second, facetNet outputs a continuous score that quantifies a nodes affiliation to each of the communities detected, and thirdly it permits temporal continuity in the community structure whereby prior node affiliation at time

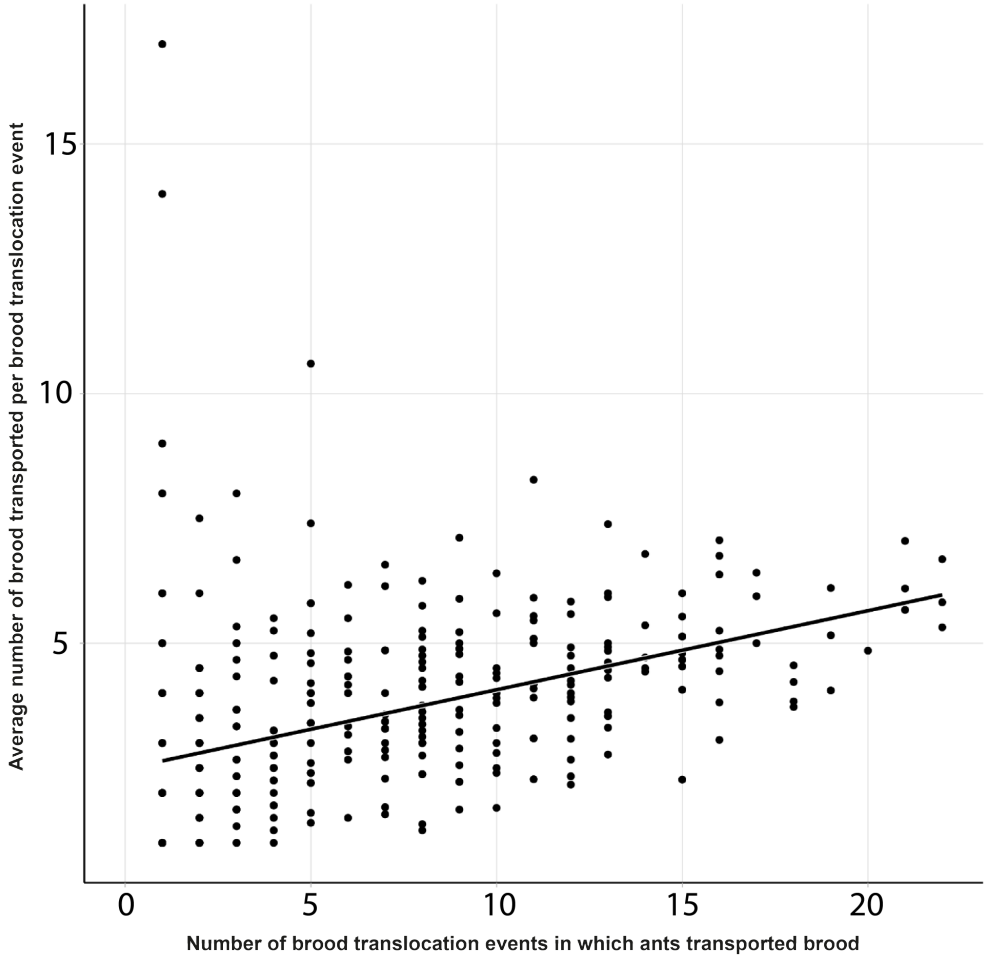

Figure 5.22 – Average number of times an ant participates in brood movement (as measured by the number of brood translocation event in which it performed brood transport) is significantly positively correlated with the average number of brood moved per brood translocation event.

t - 1 can have a weighted influence on node affiliation at time t. In our analyses of community structure, we allowed facetNet to determine the best supported number of communities. Across all six colonies the modularity (in short, the ratio of within community interactions compared to between community interactions) is maximised for two communities which supports the premise of two fundamental communities within our colonies [129].

To perform community detection on our social networks, all interactions between individual ants $i, j \in (1, \ldots, n)$ are recorded in a standard interaction matrix. The observed probability for

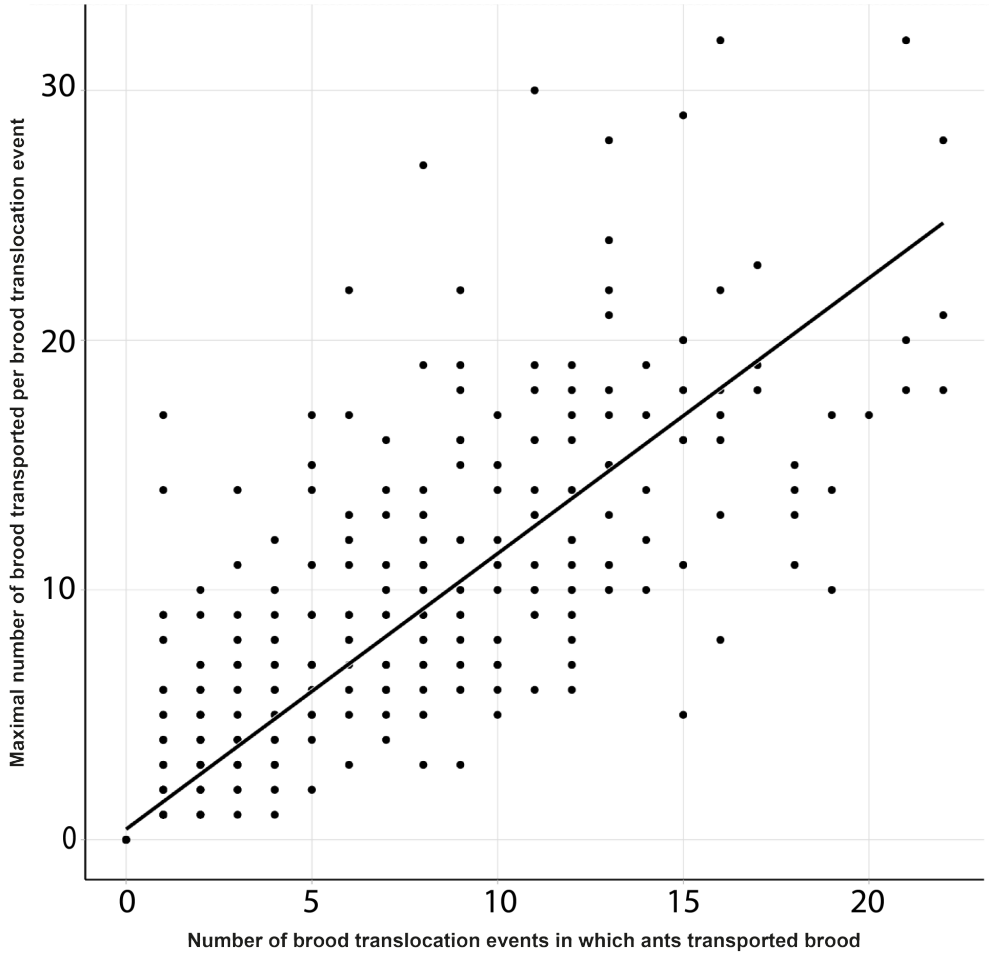

Figure 5.23 – Maximal number of times an ant participates in brood movement (as measured by the number of brood translocation event in which it performed brood transport) is significantly positively correlated with the maximal amount of brood transported by any one ant.

an interaction $W_{i,j}$ is evaluated with the joint distribution $W_{i,j} \approx p_{i\to k}.p_k.p_{j\to k}$ which evaluates the probability of observing an interaction between ants i and j within the community $k \in (1,\ldots,m_c)$. The number of communities m_c must be designated prior to the implementation of facetNet, however we first evaluated modularity allowing for 2,3,4 or 5 potential communities we found that modularity was optimised when $m_c = 2$ as in Richardson et al, 2021. Subsequently all iterations of facetNet assumed two communities. Therefore, for a given ant (i) its affiliation (A) to a given community (k) is calculated as $A_{i\to k} = p_{i\to k}.p_k / (\sum_k^{m_c} p_{i\to k}.p_k)$.

Ants are typically characterised according to their task performance and with most within-nest activities pertain to nursing and most outside-nest activities relate to foraging. As such, it is usual to assign nurse and forager labels to communities detected in ant colonies [100], [129]. In order to perform a similar assignment with our data, for each social network generated, a two-hour video was observed, both within the nest and the foraging arena four hours prior (03:00 UTC) to the temperature change outlined in 'Experiment Protocol' above. Throughout this observation period the first 3 ants to demonstrate foraging behaviour (defined as antennation of and/or consumption of a water or food resource) and the first 3 ants to demonstrate nurse behaviour (defined as antennation of and/or physical interaction with a brood) were recorded. Subsequently, the community to which our identified nurses belong (k_N) that have the highest affiliation score is designated as the nurse community.

To similarly confirm the identity of the forager community the same evaluation is performed independently whereby the community to which our identified foragers belong k_F that has the lowest affiliation score is designated as the forager community, and social maturity is calculated accordingly and compared. As we assume the presence of two communities, social maturity varies from 0 – 1 and in all cases, ants identified as foragers shared a community identity with one another and returned social maturity values >0.5. By comparison this community identity was different to that which was always shared by ants identified as nurses which always returned social maturity values of <0.5.

Additionally, it is possible to assign a temporal weight to the model using the parameter $\alpha(\in (0,1))$, whereby an individuals a-priori affiliation influences its future affiliation. This process smooths comparison of networks over time but can lead to erroneous affiliation of ants to communities should community membership be highly dynamic. As our experiment manipulates social organisation through targeted removal of individuals it was expected that social organisation would change and so only a weak influence of was permitted ($\alpha = 0.8$) whereby a value of 1 completely negates any *apriori* affiliation and a value of 0 effectively solidifies community membership.

5.5.4 Certain ant morphology and social maturity are required to be a brood transporter

We first tested for the effect of social maturity and morphology on likelihood to perform brood movement, using the entire dataset. For each ant an image was selected where the ant was at rest. The number of pixels from the tip of the mandibles to the tip of the gaster was used as a reference for body length and the number of pixels from eye to eye was used as a reference for headwidth. We found that body length was not a significant predictor ($\beta = -0.011$, SE = 0.029, z(38426) = -0.377, $p < 0.0001$), however headwidth ($\beta = -0.116$, SE = 0.024, z(38426) = -4.813, $p < 0.0001$) and social maturity ($\beta = -0.899$, SE = 0.021, z(38426) = -41.941, $p < 0.0001$) are significantly correlated. However, as the effect of the treatment condition may have affected the usual function of brood transport models were run separately for both control and treatment for comparison purposes. In the control, body length ($\beta = 0.077$, SE = 0.036, z(19054) = 2.151, p = 0.032), headwidth ($\beta = -0.131$, SE = 0.04, z(19054) = -3.223, p = 0.001) and social maturity ($\beta = -0.862$, SE = 0.026, z(19054) =-32.729, $p < 0.0001$) are significant correlates of brood transport behaviour, whereas in treatment only social maturity correlated with brood movement ($\beta = -0.108$, SE = 0.044, z(9686) = -22.857, $p < 0.0001$). The observation that morphological variables significantly correlate with brood transport in the control condition but not treatment led us to investigate the relationship between headwidth and body length. This relationship is well documented in ants and is referred to as diphasic allometric with a smaller proportion of ants having a larger-than-expected headwidth relative to body length being referred to as majors, and the majority of ants with more modest scaling being referred to as minors. Figure 5.24a depicts how the measurement is performed while an example of minor ant and major ant is presented in Figure 5.24b and Figure 5.24c, respectively. Figure 5.25 reveals that, when plotting these relationships for ants in control and treatment separately, brood transporters are primarily confined to the cluster of ants referred to as minors, and this is more visible in the control data than for treatment. In light of these observations, we re-analysed the data, excluding the majors to see if morphological measurements still correlated with brood transport. Subsequently, in the control data set only social maturity ($\beta = -2.601$,

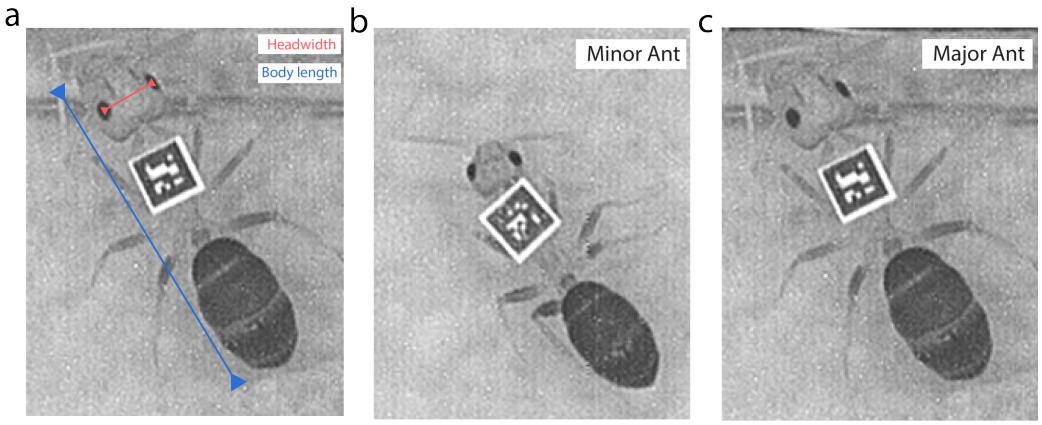

Figure 5.24 – Minor and major ants in terms of morphology. a) Red line shows how the headwidth is measured, as a distance between eyes. The blue line depicts ho the body lenght is measured. b) An example of minor ant is presented. c) An example of major ant is presented.

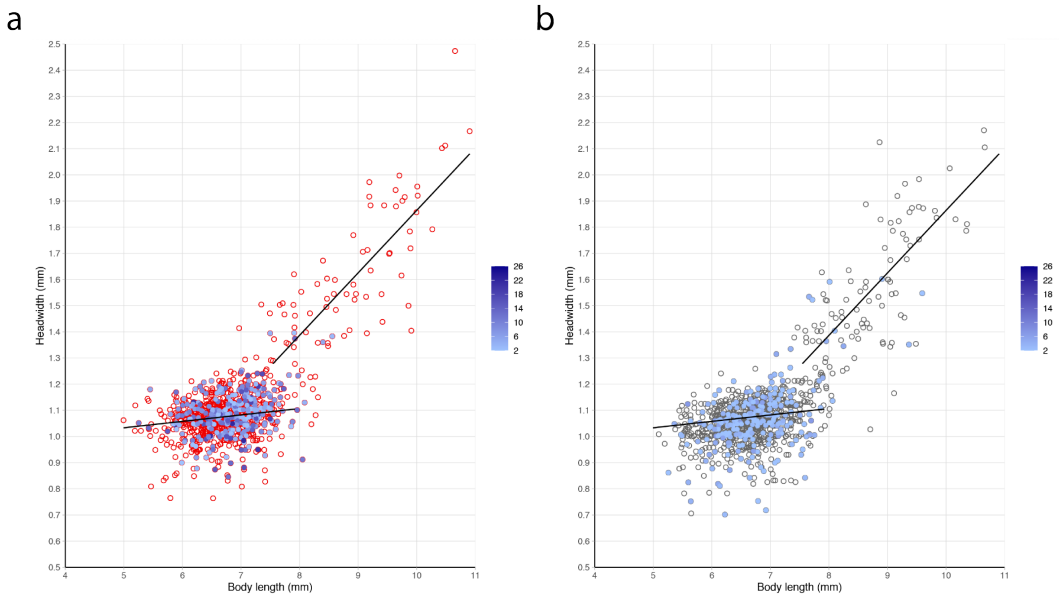

Figure 5.25 – Distinctive allometric scaling relationships within C. floridanus colonies. Graphs are colour coded such that red open circles indicate ants within the control condition that did not move brood (a), and grey open circles indicate ants within treatment that did not move brood in the treatment condition(b). Blue dots indicate ant that performed brood movement, with the intensity of the blue indicating the number of times an ant participated in moving brood in observation windows. Relatively few ants that move brood can be found within the 'major' ants, those that exhibit a higher allometric relationships between headwidth and body length (upper regression lines on both graphs).

SE = 0.08, z(18598) = -32.620, $p < 0.0001$) aligning it with the model for treatment. With the exclusion of major workers from our data set the morphological variables of headwidth and

body length do not significantly correlate with performance of brood transport suggesting there is no morphological specialisation within minors. On the other hand, it appears as if, at least under control conditions, majors are unlikely to perform brood movement which may be the result of their extreme allometric headwidth scaling.

5.5.5 Majority of the brood transporters are nurses

Next questions, we seek for, are: are the brood transporters solely belong to any subgroup of the colony such as nurse or forager? Can the task allocation of an ant be a criteria to become a brood transporter? The first measure we have checked is the social maturity (Figure 5.26). Figure 5.26 presents the social maturity values versus number brood transport events (Figure 5.26a for control, Figure 5.26b). As Social maturity value of nurses is less than 0.5, the result point out that the majority of the brood transporters are nurses.

Another indication to detect whether an ant is a nurse or forager is to construct the social interaction network. We have constructed the social interaction networks and detected the two separate groups of nurses and foragers. Figure 5.27 social interaction networks from the first four day of a control experiments. The blue cluster is nurse and the yellow cluster represents the foragers. The three red filled dots represent the foragers, detected by observation to validate the fact that the yellow cluster is foragers. The ants with red circles around are the brood transporters and they are mostly located in the forager cluster. Social interaction networks corroborate the findings of social maturity results such that the majority of the brood transporters is nurse, as 78.83 ± 14.13 % (n=60) and 73.07 ± 22.19 % (n=49) of the brood transporters in control and treatment experiments, respectively.

5.6 The colony shows adaptive response to different thermal contrast

We have consistently used 27^{o}C as preferable temperature and 21^{o}C as the background temperature. To check whether ants make a differential measurement, we adjusted the background

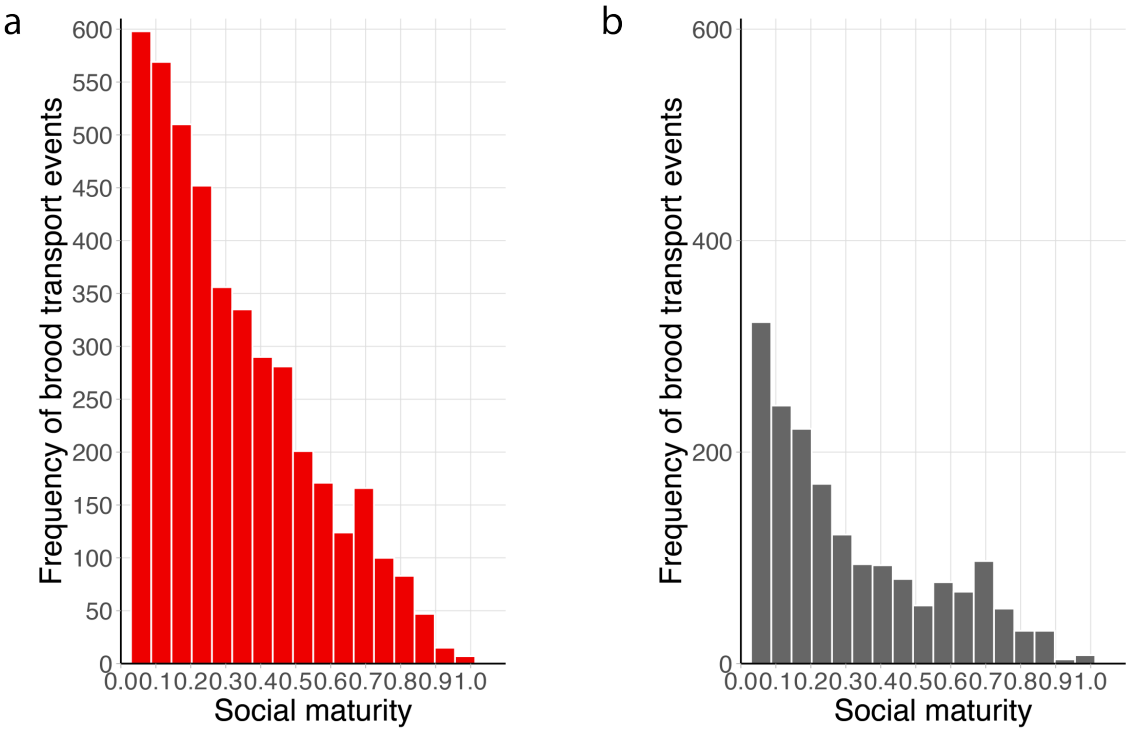

Figure 5.26 – Social Maturity as a criteria to be a brood transporter. a) The plot presents the social maturity values of the brood transporters in control of removal experiment for a colony. b) The plot presents the social maturity values of the brood transporters in treatment of removal experiment for a colony.

temperature to 21°C, 22°C, 23°C, and 24°C in four different experiments. The duration of the brood transport monotonically increased as the background temperature increased (Figure 5.28a). When we group the duration from four different background temperatures as short and long (Figure 5.28b), we detected that the number of brood transporters corresponding to short and long translocation events are significantly different. More ants attended to the transport event when the background temperature was cooler (Figure 5.28c). This data suggests that the sensing capabilities of ants that transport brood are not same. Warmer background temperature only stimulates the most sensitive brood transporters.

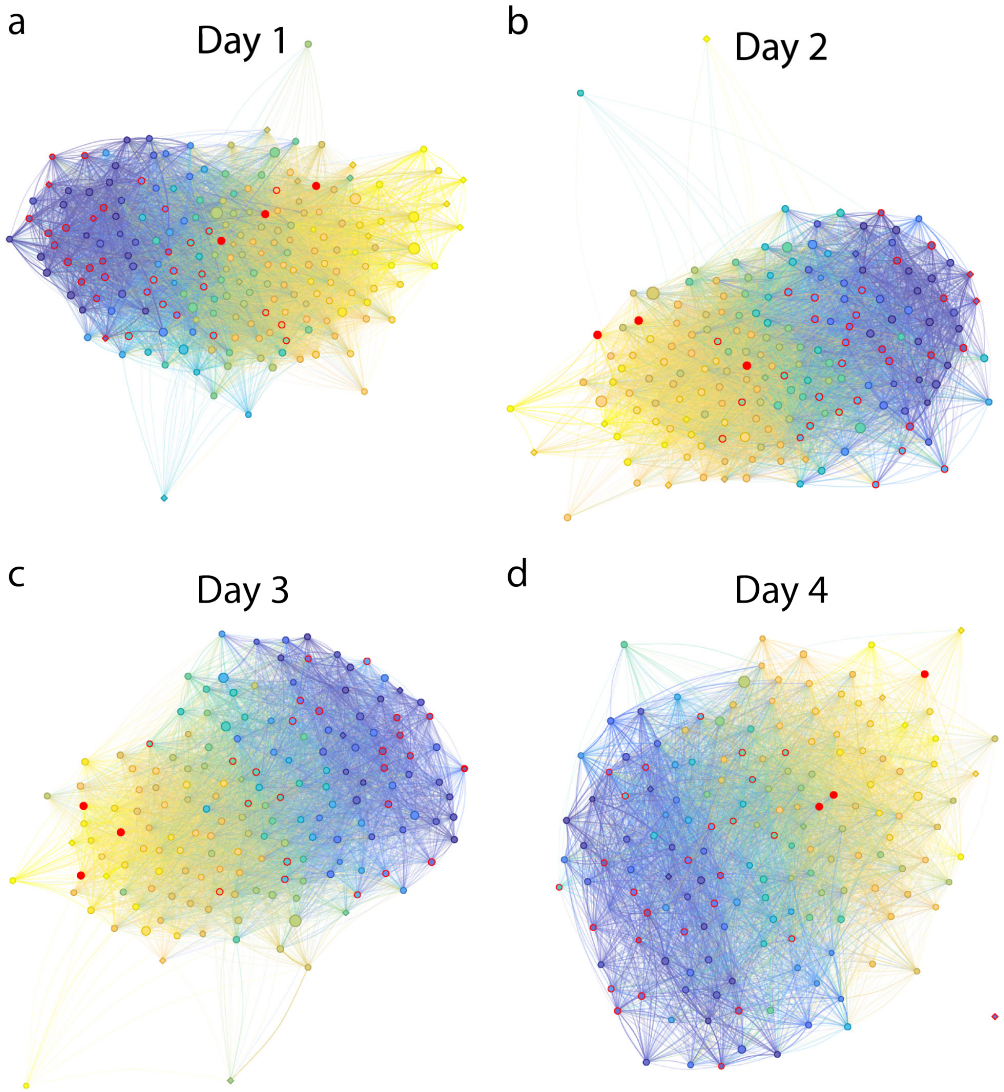

Figure 5.27 – Social Interaction networks showing nurse (blue) and forager (yellow) clusters with the brood transporters. The social interaction networks from first four days of control experiment of a colony. The red dots are the foragers who are detected by human observation to confirm that yellow cluster is foragers. The brood transporters are detected with red circles. a)Day 1, b)Day 2, c)Day 3, d)Day 4.

5.7 Collective decision making and consensus

So far, we provided only a single choice to the colony by setting one stripe at their preferred temperature. One way of exploring whether the colony exchanges information and seeks a consensus is to provide multiple options. To this end, we have located the ants into the foraging arena after setting the top and bottom stripes at 27°C. These regions are selected to

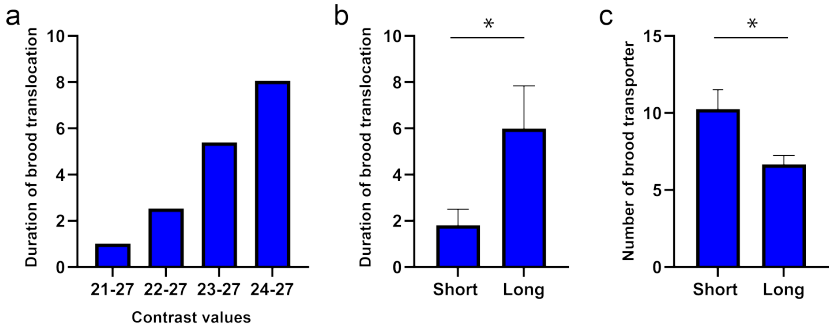

Figure 5.28 – Adaptive response of ant colonies to changing thermal signals.a) Duration of brood translocation is changing with different background temperature as a thermal signal to trigger the brood translocation. b) Duration of brood translocation is grouped into two. c) The number of brood transporter in the translocation event corresponding to two duration group in (b) is presented.

be equally distant to the nest entrance. We then let the colony move into their nest with their brood. The colony carried their brood to both stripes, and did not reach a consensus on one of those optionsFigure 5.29. This suggests that the brood translocation is driven by the individual initiative and ants do not exchange information to collectively select a target location.

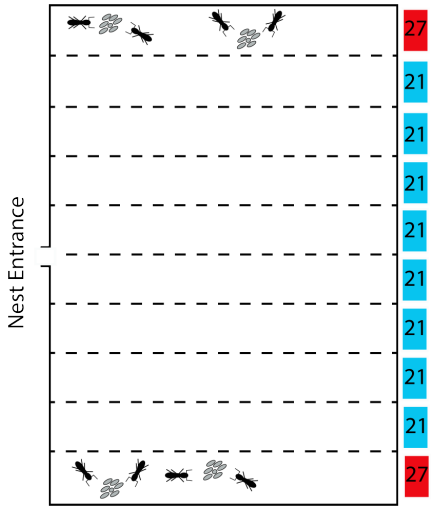

Figure 5.29 – Translocation in the case of multiple preferable options.

5.8 Discussion

In this chapter, a temperature regulation system (ThermoReg) is introduced for initiation of the translocation of the brood pile through application of a physical stimulus, temperature. By utilizing ThermoReg, we identified the preferable temperature levels for the brood. Next, we stimulated the colony to transport their brood to predefined locations. One of the important findings is that there is a subgroup of ants who participates in the transport events. Moreover, the identity of individuals change from one event to another.

The frequency of the attendance of brood transporters to consecutive translocation events did not show any trend and demonstrated a stochastic nature. On the other hand, the ant that transport the first brood in a given event transports the most number of brood at the end of the trial. This result suggests that the thermal sensitivity of the ants varies among individuals, and the transporter with higher sensitivity is more likely to initiate brood transportation. As a next step, we wanted to investigate the identity of those individuals who participate in brood transport.

We designed controlled experiments where we removed the individual transporters after every translocation event. We discovered that the colony completely abandons thermoregulation of their brood after a certain number of ants are removed from the colony. Then, we discovered that the brood transporters have a certain morphology that puts them into a category called minor ants. We calculated social maturity of individual ants and generated the social interaction maps of the colony. These data sets unveiled that the majority of the brood transporters are nurses. After learning the identity and morphological criteria to be brood transporter, we have designed experiments to explore the response of the colony to changing thermal signals. The total duration of transport event changes depending on the background temperature, indicating an adaptive response. Lastly, we have offered the colony two symmetrically located stripe to check if they would reach a concensus. Ants moved their brood to both stripes, indicating that reaching a consensus is not part of the thermoregulation response.

6 Conclusion and Future Outlook

Adaptive self-organization has been instrumental in shaping nature throughout evolution and will play an important role in the future of life on earth. Novel imaging and analysis methods allow the study of many cells and organisms, and it is the right time to introduce robotic platforms that apply physiologically relevant signals. We believe that the technological advancements that are introduced in this thesis will allow us to guide biological self-organization for building novel systems. Finally, research in this domain will reveal principles that can be applied for building bioinspired self-organized engineered systems.

6.1 Major Contributions

I proposed a methodological approach that combines quantitative imaging with robotic manipulation and computational modelling to investigate the principles of biological self-organization. I built two novel robotic manipulation platforms that are interfaced with fibrous tissues and ant colonies. The main features of the presented platforms are as follows.

- **Local and non-invasive manipulation**. This feature is accomplished by fabricating cell-sized microactuators and using Peltier elements.
- **Precise and programmable manipulation**. The magnetic actuation system applies torque that spans the whole physiologically relevant spectrum with high temporal and

spatial precision. ThermoReg generates physiologically relevant temperature values with high resolution and stability. The torque and temperature values can be programmed and automatically applied over days and weeks.

- **Tracking of all the subunits of the ensemble**. The individual cells are tracked using a fully motorized microscope, and time-lapse bright-field and fluorescence imaging. Individual ants and their interactions with each other are followed by the automated video tracking system thanks to the use of ID tags.

- **Measuring the propagation of external signal**. Imaging does not provide information on the forces acting on the fibers. A FE-based digital twin calculates these forces for a given actuation signal and ECM architecture. In the second platform where the brood translocation is investigated, the temperature assigned for the nest surface is monitored by the system.

Along with the technological contributions, the thesis presents novel findings on the mechanobiology of connective tissue cells and thermoregulation in ant colonies. I present compelling data that supports my argument that such platforms can be used to study self-organization across scales.

6.2 Future Outlook - Technical Improvements

6.2.1 Applying higher resolution manipulation

In both systems, the platforms have ability to apply manipulation with higher resolution, which means to create more local manipulation than the current version of the platforms. Manipulation with higher resolution in wireless actuation of mechanically tunable fibrous material can be achieved by either decreasing the size of the micro actuator or increasing the size of the fiber network, while keeping the size of the micro actuator in original dimensions. The disadvantage of decreasing the size of the micro actuator is to loss important amount of volume of nickel sheet, which will entail a huge reduction in the resultant magnetic torque.

To overcome this drawback, a strategy would be to switch to permanent magnetic micro metal sheet as material of the micro actuator while decreasing the size. The toxic effect of the permanent magnetic materials against the cells should be scrutinized accordingly.

For ThermoReg platform, there are two candidate strategies to increase the resolution of the manipulation. The first strategy is to decrease the size of the Peltier elements. This yields the increase in number of independent parallel temperature zones. The second strategy is the control of the each Peltier element individually. With the size of the Peltier elements on the current platform, individual control will give approximately 20 mm x 20 mm resolution while the ant body length and brood is more than 10 mm. By combining the first and second strategies, decreasing the size of Peltier elements and individual control, the resolution (20 mm x 20 mm) can be improved much more.

6.2.2 Closed-loop control of micro actuator

Further improvement can be achieved by designing the closed-loop version of the magnetic micro actuator. Closed-loop control may improve the accuracy of the torque applied, in case the material of the micro actuator is a soft magnetic material such as nickel. As the magnetic domains and the resultant orientation of global magnetization of the micro actuator are prone to align with external magnetic field, the external magnetic field needs to keep the angle between the easy axis of the actuator and the field constant. Towards this goal, the position and orientation of the micro actuator can be obtained from microscopy images via an image-processing algorithm. The torque can be calculated by coupling the orientation data with external magnetic field orientation, obtained from rotational positioner. In case of a change in the orientation of the actuator, external magnetic field can be accurately adapted to keep the same torque or to any programmed level.

6.2.3 Modeling cells in FEM

The finite element model is utilized to map the propagation and resultant strain and stress created deformation by the micro actuator on fiber network. In addition to mapping the deformation characteristics, alternative functionality of the model would be the planning/prediction of the actuation. Before an experiment, the resultant deformation and stress maps can be created with different actuator position, number and size to obtain the intended deformation and stress. Another level of improving the model is to incorporating the biological cells to fiber network. As we can, now, program the position of cells in experiment, we can also position them in the model with actuator to calculate the deformation on cell as well as the deformation of fiber network. The cells can be incorporated in two different methods. The first method is to model the cells as circular rigid shell as modeling the micro actuator. The circular rigid shells can rotate and reel fibers as the cells perform. Depending on the external forces, they can also displace with the network. The second method is to model the cells as a deformable sheet. The advantage of this method is being able to realistic viscoelastic material properties of the cell. As the cell is deformable, deformation of the cell can also be added to the output set of the model.

6.3 Future Outlook - Research

In Chapter 3, I presented a platform for the wireless actuation of mechanically tunable fibrous substrates. The rotation of metal piece is controlled by a programmable magnetic actuation system and the digital twin of the substrate calculates the mechanical stresses. The obvious way that mechanical loading can activate intracellular signaling is through ion channels. I showed that Ca^{2+} signaling is triggered within cells that are stretched by the actuator through fibers. The downstream implications of this signal is not known. We have to carefully study how changes in intracellular calcium level modulate the response of the cell. We expect that cellular contractility may change as calcium is involved in myosin activity. The dynamics of nuclear translocation of transcriptional regulators such as YAP and MRTF-A is another

obvious direction to explore. Previous work has repeatedly shown that when cells respond to changes in substrate stiffness or mechanical loading, these transcription factors are involved in the process. The third direction is to study integrin-ECM connection and focal adhesion complexes. They are the mechanosensors that perceive and transmit mechanical signals to the cytoskeleton and the nucleus. Fourth direction is to study Rho signaling. Once we establish the connection from generation of the mechanical signal to the biological response, the characteristics of the signal can be systematically varied. We can tune how fast we rotate the actuator, how much we rotate the actuator, and how long we keep the cells mechanically loaded.

Finite element modelling is used in **Chapter 3** to simulate deformation and mechanical stress generated by the wireless microactuator. The measured and calculated force values were not identical due to some of the assumptions I made. To eliminate the discrepancy, the geometry of the fibers can be reconstituted in three dimensions. The current model uses the projected image of the confocal scan. We can also precisely probe the level of attachment of every fiber intersection. In the existing model, all the fiber intersections are assumed to be a firm attachment. Lastly, I assumed that all the fiber segments (i.e., fiber piece between intersections) have the same diameter,although the segments might have slightly different diameters. These variations can be considered in the model.

In the current work, the synthetic fibers are electrospun from a linearly elastic material. Native tissues are viscoelastic. There are ways of fabricating fibrous substrates with advanced features such as complex rheology and our manipulation paradigm is compatible with these substrates. FE modelling is capable of simulating the deformation of solid structures with nonlinear elasticity.

The wireless microactuators are cut from nickel sheets using laser micromachining. They are firmly attached to the fibrillar substrate. It would be very interesting to create cell-sized microactuators that can move on the substrate and engage with the substrate on-demand. Selective de-activation of assembled actuators is another interesting direction. This could be

done using a laser and a demagnetization process.

In **Chapter 5**, I developed a temperature regulation system for ants that seamlessly interfaces with the tracking system and the environmental chamber. We have explored the dynamics of brood translocation and identity of the brood transporters. The ant colony showed adaptive response to changing thermal signals and did not indicate any sign of consensus for the target of brood translocation. The work is far from being completed. First, we can focus on the physiology of temperature sensing. There are techniques to physically block temperature sensors on select ants to figure out whether they all make measurements or some of them follow the instructions provided by informed individuals. Second, detailed spatial analyses on the dynamics of translocation will help us answer the effect of proximity of a transporter to a brood at the moment of thermal signal change. Spatial analyses is a candidate approach to decipher the stochastic nature of brood transport such as the frequency of attendance of a transporter to a translocation event. It is probable that ants that are close to brood act quickly to move them to a more favorable location. Third, we can work with other ant species to explore how universal the temperature preferences are and whether they all have a subgroup of ants that deal with thermoregulation of brood care.

Automated tracking system enabled us to track all the individual ants and their interactions. Tracking system can not detect the brood, which makes it necessary to manually post process the videos. Machine learning techniques can be used for markerless identification of brood, as discussed in **Chapter 4**. Automated tracking of brood will significantly increase the speed of processing and the throughput of analysis, and completely remove bias.

References

[1] S. Jalal, S. Shi, V. Acharya, R. Y. J. Huang, V. Viasnoff, A. D. Bershadsky, and Y. H. Tee, "Actin cytoskeleton self-organization in single epithelial cells and fibroblasts under isotropic confinement", *Journal of Cell Science*, vol. 132, no. 5, pp. 1–14, 2019.

[2] N. Yamaguchi, T. Mizutani, K. Kawabata, and H. Haga, "Leader cells regulate collective cell migration via Rac activation in the downstream signaling of integrin β1 and PI3K", *Scientific Reports*, vol. 5, pp. 1–8, 2015.

[3] A. Khuong, J. Gautrais, A. Perna, C. Sbaï, M. Combe, P. Kuntz, C. Jost, and G. Theraulaz, "Stigmergic construction and topochemical information shape ant nest architecture", *Proceedings of the National Academy of Sciences of the United States of America*, vol. 113, no. 5, pp. 1303–1308, 2016.

[4] M. J. Sanderson, A. C. Charles, and E. R. Dirksen, "Mechanical stimulation and intercellular communication increases intracellular Ca2+ in epithelial cells", *Molecular Biology of the Cell*, vol. 1, no. 8, pp. 585–596, 1990.

[5] X. Shao, Q. Li, A. Mogilner, A. D. Bershadsky, and G. V. Shivashankar, "Mechanical stimulation induces formin-dependent assembly of a perinuclear actin rim", *Proceedings of the National Academy of Sciences of the United States of America*, vol. 112, no. 20, E2595–E2601, 2015.

[6] J. Y. Tinevez, U. Schulze, G. Salbreux, J. Roensch, J. F. Joanny, and E. Paluch, "Role of cortical tension in bleb growth", *Proceedings of the National Academy of Sciences of the United States of America*, vol. 106, no. 44, pp. 18 581–18 586, 2009.

[7] F. H. C. Crick and A. F. W. Hughes, "The physical properties of cytoplasm: A study by means of the magnetic particle method Part I. Experimental", *Experimental Cell Research*, vol. 1, no. 1, pp. 37–80, 1950.

[8] A. R. Bausch, W. Möller, and E. Sackmann, "Measurement of local viscoelasticity and forces in living cells by magnetic tweezers", *Biophysical Journal*, vol. 76, no. 1 I, pp. 573–579, 1999.

[9] B. D. Matthews, D. R. Overby, R. Mannix, and D. E. Ingber, "Cellular adaptation to mechanical stress: Role of integrins, Rho, cytoskeletal tension and mechanosensitive ion channels", *Journal of Cell Science*, vol. 119, no. 3, pp. 508–518, 2006.

[10] N. J. Sniadecki, A. Anguelouch, M. T. Yang, C. M. Lamb, Z. Liu, S. B. Kirschner, Y. Liu, D. H. Reich, and C. S. Chen, "Magnetic microposts as an approach to apply forces to living cells", *Proceedings of the National Academy of Sciences of the United States of America*, vol. 104, no. 37, pp. 14 553–14 558, 2007.

[11] D. Choquet, D. P. Felsenfeld, and M. P. Sheetz, "Extracellular matrix rigidity causes strengthening of integrin- cytoskeleton linkages", *Cell*, vol. 88, no. 1, pp. 39–48, 1997.

[12] F. Falleroni, V. Torre, and D. Cojoc, "Cell mechanotransduction with piconewton forces applied by optical tweezers", *Frontiers in Cellular Neuroscience*, vol. 12, no. May, pp. 1–11, 2018.

[13] Z. Liu, Y. Liu, Y. Chang, H. R. Seyf, A. Henry, A. L. Mattheyses, K. Yehl, Y. Zhang, Z. Huang, and K. Salaita, "Nanoscale optomechanical actuators for controlling mechanotransduction in living cells", *Nature Methods*, vol. 13, no. 2, pp. 143–146, 2016.

[14] Y. Chandorkar, A. Castro Nava, S. Schweizerhof, M. Van Dongen, T. Haraszti, J. Köhler, H. Zhang, R. Windoffer, A. Mourran, M. Möller, and L. De Laporte, "Cellular responses to beating hydrogels to investigate mechanotransduction", *Nature Communications*, vol. 10, no. 1, pp. 1–13, 2019.

[15] M. Abercrombie and J. E. Heaysman, "Observations on the social behaviour of cells in tissue culture. I. Speed of movement of chick heart fibroblasts in relation to their mutual contacts", *Experimental Cell Research*, vol. 5, no. 1, pp. 111–131, 1953.

[16] C. Carmona-Fontaine, H. K. Matthews, S. Kuriyama, M. Moreno, G. A. Dunn, M. Parsons, C. D. Stern, and R. Mayor, "Contact inhibition of locomotion in vivo controls neural crest directional migration", *Nature*, vol. 456, no. 7224, pp. 957–961, 2008.

[17] S. Vedel, S. Tay, D. M. Johnston, H. Bruus, and S. R. Quake, "Migration of cells in a social context", *Proceedings of the National Academy of Sciences*, vol. 110, no. 1, pp. 129–134, 2013.

[18] A. J. Engler, S. Sen, H. L. Sweeney, and D. E. Discher, "Matrix elasticity directs stem cell lineage specification", *Cell*, vol. 126, no. 4, pp. 677–689, 2006.

[19] C. Carmona-Fontaine, H. K. Matthews, S. Kuriyama, M. Moreno, G. A. Dunn, M. Parsons, C. D. Stern, and R. Mayor, "Contact inhibition of locomotion in vivo controls neural crest directional migration", *Nature*, vol. 456, no. 7224, pp. 957–961, 2008.

[20] X. Trepat and J. J. Fredberg, "Plithotaxis and emergent dynamics in collective cellular migration", *Trends in Cell Biology*, vol. 21, no. 11, pp. 638–646, 2011.

[21] A. Shellard and R. Mayor, "Collective durotaxis along a self-generated stiffness gradient in vivo", *Nature*, vol. 600, no. 7890, pp. 690–694, 2021.

[22] I. Nitsan, S. Drori, Y. E. Lewis, S. Cohen, and S. Tzlil, "Mechanical communication in cardiac cell synchronized beating", *Nature Physics*, vol. 12, no. 5, pp. 472–477, 2016.

[23] P. Pakshir, M. Alizadehgiashi, B. Wong, N. M. Coelho, X. Chen, Z. Gong, V. B. Shenoy, C. McCulloch, and B. Hinz, "Dynamic fibroblast contractions attract remote macrophages in fibrillar collagen matrix", *Nature Communications*, vol. 10, no. 1, pp. 1–17, 2019.

[24] A. J. Hughes, H. Miyazaki, M. C. Coyle, J. Zhang, M. T. Laurie, D. Chu, Z. Vavrušová, R. A. Schneider, O. D. Klein, and Z. J. Gartner, "Engineered Tissue Folding by Mechanical Compaction of the Mesenchyme", *Developmental Cell*, vol. 44, no. 2, pp. 165–178, 2018.

[25] B. M. Baker, B. Trappmann, W. Y. Wang, M. S. Sakar, I. L. Kim, V. B. Shenoy, J. A. Burdick, and C. S. Chen, "Cell-mediated fibre recruitment drives extracellular matrix mechanosensing in engineered fibrillar microenvironments", *Nature Materials*, vol. 14, no. 12, pp. 1262–1268, 2015.

[26] S. Sen, A. J. Engler, and D. E. Discher, "Matrix strains induced by cells: Computing how far cells can feel", *Cellular and Molecular Bioengineering*, vol. 2, no. 1, pp. 39–48, 2009.

[27] A. J. Engler, M. A. Griffin, S. Sen, C. G. Bönnemann, H. L. Sweeney, and D. E. Discher, "Myotubes differentiate optimally on substrates with tissue-like stiffness: Pathological implications for soft or stiff microenvironments", *Journal of Cell Biology*, vol. 166, no. 6, pp. 877–887, 2004.

[28] M. S. Hall, F. Alisafaei, E. Ban, X. Feng, C. Y. Hui, V. B. Shenoy, and M. Wu, "Fibrous nonlinear elasticity enables positive Mechanical feedback between cells and ECMs", *Proceedings of the National Academy of Sciences of the United States of America*, vol. 113, no. 49, pp. 14 043–14 048, 2016.

[29] J. Notbohm, A. Lesman, P. Rosakis, D. A. Tirrell, and G. Ravichandran, "Microbuckling of fibrin provides a mechanism for cell mechanosensing", *Journal of the Royal Society Interface*, vol. 12, no. 108, 2015.

[30] X. Xu and S. A. Safran, "Nonlinearities of biopolymer gels increase the range of force transmission", *Physical Review E - Statistical, Nonlinear, and Soft Matter Physics*, vol. 92, no. 3, pp. 1–10, 2015.

[31] C. Storm, J. J. Pastore, F. C. MacKintosh, T. C. Lubensky, and P. A. Janmey, "Nonlinear elasticity in biological gels", *Nature*, vol. 435, no. 7039, pp. 191–194, 2005.

[32] W. R. Legant, A. Pathak, M. T. Yang, V. S. Deshpande, R. M. McMeeking, and C. S. Chen, "Microfabricated tissue gauges to measure and manipulate forces from 3D

microtissues", *Proceedings of the National Academy of Sciences of the United States of America*, vol. 106, no. 25, pp. 10 097–10 102, 2009.

[33] R. Zhao, T. Boudou, W. G. Wang, C. S. Chen, and D. H. Reich, "Decoupling cell and matrix mechanics in engineered microtissues using magnetically actuated microcantilevers", *Advanced Materials*, vol. 25, no. 12, pp. 1699–1705, 2013.

[34] M. S. Sakar, J. Eyckmans, R. Pieters, D. Eberli, B. J. Nelson, and C. S. Chen, "Cellular forces and matrix assembly coordinate fibrous tissue repair", *Nature communications*, vol. 7, no. 1, pp. 1–8, 2016.

[35] E. Mailand, B. Li, J. Eyckmans, N. Bouklas, and M. S. Sakar, "Surface and bulk stresses drive morphological changes in fibrous microtissues", *Biophysical journal*, vol. 117, no. 5, pp. 975–986, 2019.

[36] A. S. Abhilash, B. M. Baker, B. Trappmann, C. S. Chen, and V. B. Shenoy, "Remodeling of fibrous extracellular matrices by contractile cells: Predictions from discrete fiber network simulations", *Biophysical Journal*, vol. 107, no. 8, pp. 1829–1840, 2014.

[37] P. Ronceray and M. Lenz, "Connecting local active forces to macroscopic stress in elastic media", *Soft Matter*, vol. 11, no. 8, pp. 1597–1605, 2015.

[38] F. Beroz, L. M. Jawerth, S. Münster, D. A. Weitz, C. P. Broedersz, and N. S. Wingreen, "Physical limits to biomechanical sensing in disordered fibre networks", *Nature Communications*, vol. 8, no. May, 2017.

[39] P. Ronceray, C. Broedersz, and M. Lenz, "Fiber networks amplify active stress", no. 2, 2015.

[40] M. C. Kim, Y. R. Silberberg, R. Abeyaratne, R. D. Kamm, and H. H. Asada, "Computational modeling of three-dimensional ECMrigidity sensing to guide directed cell migration", *Proceedings of the National Academy of Sciences of the United States of America*, vol. 115, no. 3, E390–E399, 2018.

[41] F. E. Uslu, C. D. Davidson, E. Mailand, N. Bouklas, B. M. Baker, and M. S. Sakar, "Engineered Extracellular Matrices with Integrated Wireless Microactuators to Study Mechanobiology", *Advanced Materials*, vol. 33, no. 40, 2021.

[42] L. Sapir and S. Tzlil, "Talking over the extracellular matrix: How do cells communicate mechanically?", *Seminars in Cell and Developmental Biology*, vol. 71, pp. 99–105, 2017.

[43] J. D. Humphrey, E. R. Dufresne, and M. A. Schwartz, "Mechanotransduction and extracellular matrix homeostasis", *Nature Reviews Molecular Cell Biology*, vol. 15, no. 12, pp. 802–812, 2014.

[44] F. M. Watt and W. T. Huck, "Role of the extracellular matrix in regulating stem cell fate", *Nature Reviews Molecular Cell Biology*, vol. 14, no. 8, pp. 467–473, 2013.

[45] M. W. Pickup, J. K. Mouw, and V. M. Weaver, "The extracellular matrix modulates the hallmarks of cancer", *Embo Reports*, vol. 15, pp. 1243–1253, 2014.

[46] A. D. Doyle and K. M. Yamada, "Mechanosensing via cell-matrix adhesions in 3D microenvironments", *Experimental Cell Research*, vol. 343, no. 1, pp. 60–66, 2016.

[47] B. Trappmann and C. S. Chen, "How cells sense extracellular matrix stiffness: A material's perspective", *Current Opinion in Biotechnology*, vol. 24, no. 5, pp. 948–953, 2013.

[48] O. Chaudhuri, J. Cooper-White, P. A. Janmey, D. J. Mooney, and V. B. Shenoy, "Effects of extracellular matrix viscoelasticity on cellular behaviour", *Nature*, vol. 584, no. 7822, pp. 535–546, 2020.

[49] Z. Sun, S. S. Guo, and R. Fässler, "Integrin-mediated mechanotransduction", *Journal of Cell Biology*, vol. 215, no. 4, pp. 445–456, 2016.

[50] B. M. Baker and C. S. Chen, "Deconstructing the third dimension – how 3D culture microenvironments alter cellular cues", *Journal of Cell Science*, vol. 125, no. 13, pp. 3015–3024, 2012.

[51] F. Spill, D. S. Reynolds, R. D. Kamm, and M. H. Zaman, "Impact of the physical microenvironment on tumor progression and metastasis", *Current Opinion in Biotechnology*, vol. 40, pp. 41–48, 2016.

[52] L. Li, J. Eyckmans, and C. S. Chen, "Designer biomaterials for mechanobiology", *Nature Materials*, vol. 16, no. 12, pp. 1164–1168, 2017.

[53] C. D. Davidson, W. Y. Wang, I. Zaimi, D. K. P. Jayco, and B. M. Baker, "Cell force-mediated matrix reorganization underlies multicellular network assembly", *Scientific Reports*, vol. 9, no. 1, pp. 1–13, 2019.

[54] W. Y. Wang, C. D. Davidson, D. Lin, and B. M. Baker, "Actomyosin contractility-dependent matrix stretch and recoil induces rapid cell migration", *Nature Communications*, vol. 10, no. 1, pp. 1–12, 2019.

[55] S. Kim, M. Uroz, J. L. Bays, and C. S. Chen, "Harnessing Mechanobiology for Tissue Engineering", *Developmental Cell*, vol. 56, no. 2, pp. 180–191, 2021.

[56] B. Fabry, G. N. Maksym, R. D. Hubmayr, J. P. Butler, and J. J. Fredberg, "Implications of heterogeneous bead behavior on cell mechanical properties measured with magnetic twisting cytometry", *Journal of Magnetism and Magnetic Materials*, vol. 194, no. 1, pp. 120–125, 1999.

[57] W. J. Polacheck, M. L. Kutys, J. Yang, J. Eyckmans, Y. Wu, H. Vasavada, K. K. Hirschi, and C. S. Chen, "A non-canonical Notch complex regulates adherens junctions and vascular barrier function", *Nature*, vol. 552, no. 7684, pp. 258–262, 2017.

[58] D. Riveline, E. Zamir, N. Q. Balaban, U. S. Schwarz, T. Ishizaki, S. Narumiya, Z. Kam, B. Geiger, and A. D. Bershadsky, "Focal contacts as mechanosensors: Externally applied local mechanical force induces growth of focal contacts by an mDia1-dependent and ROCK-independent mechanism", *Journal of Cell Biology*, vol. 153, no. 6, pp. 1175–1185, 2001.

[59] G. T. Charras and M. A. Horton, "Single cell mechanotransduction and its modulation analyzed by atomic force microscope indentation", *Biophysical Journal*, vol. 82, no. 6, pp. 2970–2981, 2002.

[60] G. Bao and S. Suresh, "Cell and molecular mechanics of biological materials", *Nature Materials*, vol. 2, no. 11, pp. 715–725, 2003.

[61] K. L. Laugwitz, A. Moretti, J. Lam, P. Gruber, Y. Chen, S. Woodard, L. Z. Lin, C. L. Cai, M. M. Lu, M. Reth, O. Platoshyn, J. X. Yuan, S. Evans, and K. B. Chien, "Postnatal isl1+ cardioblasts enter fully differentiated cardiomyocyte lineages", *Nature*, vol. 433, no. 7026, pp. 647–653, 2005.

[62] C. M. Franz, A. Taubenberger, P. H. Puech, and D. J. Muller, "Studying integrin-mediated cell adhesion at the single-molecule level using AFM force spectroscopy.", *Science's STKE : signal transduction knowledge environment*, vol. 2007, no. 406, pp. 1–17, 2007.

[63] P. Tseng, J. W. Judy, and D. Di Carlo, "Magnetic nanoparticle-mediated massively parallel mechanical modulation of single-cell behavior", *Nature Methods*, vol. 9, no. 11, pp. 1113–1119, 2012.

[64] M. Tamada, M. P. Sheetz, and Y. Sawada, "Activation of a signaling cascade by cytoskeleton stretch", *Developmental Cell*, vol. 7, no. 5, pp. 709–718, 2004.

[65] S. Jungbauer, H. Gao, J. P. Spatz, and R. Kemkemer, "Two characteristic regimes in frequency-dependent dynamic reorientation of fibroblasts on cyclically stretched substrates", *Biophysical Journal*, vol. 95, no. 7, pp. 3470–3478, 2008.

[66] B. Özkale, M. S. Sakar, and D. J. Mooney, "Active biomaterials for mechanobiology", *Biomaterials*, vol. 267, no. October 2020, 2021.

[67] A. Livne, E. Bouchbinder, and B. Geiger, "Cell reorientation under cyclic stretching", *Nature Communications*, vol. 5, no. May, 2014.

[68] Y. Cui, F. M. Hameed, B. Yang, K. Lee, C. Q. Pan, S. Park, and M. Sheetz, "Cyclic stretching of soft substrates induces spreading and growth", *Nature Communications*, vol. 6, pp. 1–8, 2015.

[69] C. M. Bidan, M. Fratzl, A. Coullomb, P. Moreau, A. H. Lombard, I. Wang, M. Balland, T. Boudou, N. M. Dempsey, T. Devillers, and A. Dupont, "Magneto-active substrates for local mechanical stimulation of living cells", *Scientific Reports*, vol. 8, no. 1, pp. 1–13, 2018.

[70] A. Poulin, M. Imboden, F. Sorba, S. Grazioli, C. Martin-Olmos, S. Rosset, and H. Shea, "An ultra-fast mechanically active cell culture substrate", *Scientific Reports*, vol. 8, no. 1, pp. 1–10, 2018.

[71] A. Sutton, T. Shirman, J. V. Timonen, G. T. England, P. Kim, M. Kolle, T. Ferrante, L. D. Zarzar, E. Strong, and J. Aizenberg, "Photothermally triggered actuation of hybrid materials as a new platform for in vitro cell manipulation", *Nature Communications*, vol. 8, 2017.

[72] F. Serwane, A. Mongera, P. Rowghanian, D. A. Kealhofer, A. A. Lucio, Z. M. Hockenbery, and O. Campàs, "In vivo quantification of spatially varying mechanical properties in developing tissues", *Nature Methods*, vol. 14, no. 2, pp. 181–186, 2017.

[73] A. Mongera, P. Rowghanian, H. J. Gustafson, E. Shelton, D. A. Kealhofer, E. K. Carn, F. Serwane, A. A. Lucio, J. Giammona, and O. Campàs, "A fluid-to-solid jamming transition underlies vertebrate body axis elongation", *Nature*, vol. 561, no. 7723, pp. 401–405, 2018.

[74] M. Zhu, H. Tao, M. Samani, M. Luo, X. Wang, S. Hopyan, and Y. Sun, "Spatial mapping of tissue properties in vivo reveals a 3D stiffness gradient in the mouse limb bud", *Proceedings of the National Academy of Sciences of the United States of America*, vol. 117, no. 9, pp. 4781–4791, 2020.

[75] S. Mok, S. Al Habyan, C. Ledoux, W. Lee, K. N. MacDonald, L. McCaffrey, and C. Moraes, "Mapping cellular-scale internal mechanics in 3D tissues with thermally responsive hydrogel probes", *Nature Communications*, vol. 11, no. 1, 2020.

[76] A. W. Orr, B. P. Helmke, B. R. Blackman, and M. A. Schwartz, "Mechanisms of mechanotransduction", *Developmental Cell*, vol. 10, no. 1, pp. 11–20, 2006.

[77] P. A. Janmey and R. T. Miller, "Mechanisms of mechanical signaling in development and disease", *Journal of Cell Science*, vol. 124, no. 1, pp. 9–18, 2011.

[78] K. A. Jansen, P. Atherton, and C. Ballestrem, "Mechanotransduction at the cell-matrix interface", *Seminars in Cell and Developmental Biology*, vol. 71, pp. 75–83, 2017.

[79] B. D. Hoffman, C. Grashoff, and M. A. Schwartz, "Dynamic molecular processes mediate cellular mechanotransduction", *Nature*, vol. 475, no. 7356, pp. 316–323, 2011.

[80] C. C. Dufort, M. J. Paszek, and V. M. Weaver, "Balancing forces: Architectural control of mechanotransduction", *Nature Reviews Molecular Cell Biology*, vol. 12, no. 5, pp. 308–319, 2011.

[81] O. Chaudhuri, L. Gu, D. Klumpers, M. Darnell, S. A. Bencherif, J. C. Weaver, N. Huebsch, H. P. Lee, E. Lippens, G. N. Duda, and D. J. Mooney, "Hydrogels with tunable stress relaxation regulate stem cell fate and activity", *Nature Materials*, vol. 15, no. 3, pp. 326–334, 2016.

[82] J. J. Abbott, O. Ergeneman, M. P. Kummer, A. M. Hirt, and B. J. Nelson, "Modeling magnetic torque and force for controlled manipulation of soft-magnetic bodies", *IEEE Transactions on Robotics*, vol. 23, no. 6, pp. 1247–1252, 2007.

[83] E. Ban, J. M. Franklin, S. Nam, L. R. Smith, H. Wang, R. G. Wells, O. Chaudhuri, J. T. Liphardt, and V. B. Shenoy, "Mechanisms of Plastic Deformation in Collagen Networks Induced by Cellular Forces", *Biophysical Journal*, vol. 114, no. 2, pp. 450–461, 2018.

[84] P. P. Provenzano, D. R. Inman, K. W. Eliceiri, S. M. Trier, and P. J. Keely, "Contact guidance mediated three-dimensional cell migration is regulated by Rho/ROCK-dependent matrix reorganization", *Biophysical Journal*, vol. 95, no. 11, pp. 5374–5384, 2008.

[85] P. Friedl and K. Wolf, "Plasticity of cell migration: A multiscale tuning model", *Journal of Cell Biology*, vol. 188, no. 1, pp. 11–19, 2010.

[86] S. S. Ranade, R. Syeda, and A. Patapoutian, "Mechanically Activated Ion Channels", *Neuron*, vol. 87, no. 6, pp. 1162–1179, 2015.

[87] B. Coste, J. Mathur, M. Schmidt, T. J. Earley, S. Ranade, M. J. Petrus, A. E. Dubin, and A. Patapoutian, "Activated Cation Channels", *Science (New York, N.Y.)*, vol. 330, no. October, pp. 7–12, 2010.

[88] S. A. Gudipaty, J. Lindblom, P. D. Loftus, M. J. Redd, K. Edes, C. F. Davey, V. Krishnegowda, and J. Rosenblatt, "Mechanical stretch triggers rapid epithelial cell division through Piezo1", *Nature*, vol. 543, no. 7643, pp. 118–121, 2017.

[89] C. Pardo-Pastor, F. Rubio-Moscardo, M. Vogel-González, S. A. Serra, A. Afthinos, S. Mrkonjic, O. Destaing, J. F. Abenza, J. M. Fernández-Fernández, X. Trepat, C. Albiges-Rizo, K. Konstantopoulos, and M. A. Valverde, "Piezo2 channel regulates RhoA and actin cytoskeleton to promote cell mechanobiological responses", *Proceedings of the National Academy of Sciences of the United States of America*, vol. 115, no. 8, pp. 1925–1930, 2018.

[90] L. W. Peterson and D. Artis, "Intestinal epithelial cells: Regulators of barrier function and immune homeostasis", *Nature Reviews Immunology*, vol. 14, no. 3, pp. 141–153, 2014.

[91] M. Vishwakarma, J. P. Spatz, and T. Das, "Mechanobiology of leader–follower dynamics in epithelial cell migration", *Current Opinion in Cell Biology*, vol. 66, pp. 97–103, 2020.

[92] M. Poujade, E. Grasland-Mongrain, A. Hertzog, J. Jouanneau, P. Chavrier, B. Ladoux, A. Buguin, and P. Silberzan, "Collective migration of an epithelial monolayer in response to a model wound", *Proceedings of the National Academy of Sciences of the United States of America*, vol. 104, no. 41, pp. 15 988–15 993, 2007.

[93] A. J. Lomakin, C. J. Cattin, D. Cuvelier, Z. Alraies, M. Molina, G. P. Nader, N. Srivastava, P. J. Saez, J. M. Garcia-Arcos, I. Y. Zhitnyak, A. Bhargava, M. K. Driscoll, E. S. Welf, R. Fiolka, R. J. Petrie, N. S. de Silva, J. M. González-Granado, N. Manel, A. M. Lennon-Duménil, D. J. Müller, and M. Piel, "The nucleus acts as a ruler tailoring cell responses to spatial constraints", *Science*, vol. 370, no. 6514, 2020.

[94] V. Venturini, F. Pezzano, F. C. Castro, H. M. Häkkinen, S. Jiménez-Delgado, M. Colomer-Rosell, M. Marro, Q. Tolosa-Ramon, S. Paz-López, M. A. Valverde, J. Weghuber, P. Loza-Alvarez, M. Krieg, S. Wieser, and V. Ruprecht, "The nucleus measures shape changes for cellular proprioception to control dynamic cell behavior", *Science*, vol. 370, no. 6514, 2020.

[95] B. Özkale, R. Parreira, A. Bekdemir, L. Pancaldi, E. Özelçi, C. Amadio, M. Kaynak, F. Stellacci, D. J. Mooney, and M. S. Sakar, "Modular soft robotic microdevices for dexterous biomanipulation", *Lab on a Chip*, vol. 19, no. 5, pp. 778–788, 2019.

[96] B. W. Benham-Pyle, B. L. Pruitt, and W. J. Nelson, "Mechanical strain induces E-cadherin-dependent Yap1 and β-catenin activation to drive cell cycle entry", *Science*, vol. 348, no. 6238, pp. 1024–1027, 2015.

[97] S. Hauert, L. Winkler, J. C. Zufferey, and D. Floreano, "Ant-based swarming with positionless micro air vehicles for communication relay", *Swarm Intelligence*, vol. 2, no. 2-4, pp. 167–188, 2008.

[98] S. Camazine, J. L. Deneubourg, N. Franks, J. Sneyd, G. Theraulaz, and E. Bonabeau, *Self-organization in biological systems*. Princeton University Press, 2003.

[99] B. Blonder and A. Dornhaus, "Time-ordered networks reveal limitations to information flow in ant colonies", *PLoS ONE*, vol. 6, no. 5, pp. 1–8, 2011.

[100] D. P. Mersch, A. Crespi, and L. Keller, "Tracking individuals shows spatial fidelity is a key regulator of ant social organization", *Science*, vol. 340, no. 6136, pp. 1090–1093, 2013.

[101] A. I. Dell, J. A. Bender, K. Branson, I. D. Couzin, G. G. de Polavieja, L. P. Noldus, A. Pérez-Escudero, P. Perona, A. D. Straw, M. Wikelski, and U. Brose, "Automated image-based tracking and its application in ecology", *Trends in Ecology and Evolution*, vol. 29, no. 7, pp. 417–428, 2014.

[102] A. Mathis, P. Mamidanna, K. M. Cury, T. Abe, V. N. Murthy, M. W. Mathis, and M. Bethge, "DeepLabCut: markerless pose estimation of user-defined body parts with deep learning", *Nature Neuroscience*, vol. 21, no. 9, pp. 1281–1289, 2018.

[103] A. Gosztolai, S. Günel, V. Lobato-Ríos, M. Pietro Abrate, D. Morales, H. Rhodin, P. Fua, and P. Ramdya, "LiftPose3D, a deep learning-based approach for transforming two-dimensional to three-dimensional poses in laboratory animals", *Nature Methods*, vol. 18, no. 8, pp. 975–981, 2021.

[104] K. Bozek, L. Hebert, Y. Portugal, and G. J. Stephens, "Markerless tracking of an entire honey bee colony", *Nature Communications*, vol. 12, no. 1, pp. 1–13, 2021.

[105] T. Walter and I. D. Couzin, "Trex, a fast multi-animal tracking system with markerless identi cation, and 2d estimation of posture and visual elds", *eLife*, vol. 10, pp. 1–73, 2021.

[106] T. Gernat, V. D. Rao, M. Middendorf, H. Dankowicz, N. Goldenfeld, and G. E. Robinson, "Automated monitoring of behavior reveals bursty interaction patterns and rapid spreading dynamics in honeybee social networks", *Proceedings of the National Academy of Sciences of the United States of America*, vol. 115, no. 7, pp. 1433–1438, 2018.

[107] S. H. Choi, V. D. Rao, T. Gernat, A. R. Hamilton, G. E. Robinson, and N. Goldenfeld, "Individual variations lead to universal and cross-species patterns of social behavior", *Proceedings of the National Academy of Sciences of the United States of America*, vol. 117, no. 50, pp. 31 754–31 759, 2020.

[108] L. Jiang, Y. Cheng, S. Gao, Y. Zhong, C. Ma, T. Wang, and Y. Zhu, "Emergence of social cluster by collective pairwise encounters in Drosophila", *eLife*, vol. 9, 2020.

[109] R. Okada, T. Akamatsu, K. Iwata, H. Ikeno, T. Kimura, M. Ohashi, H. Aonuma, and E. Ito, "Waggle dance effect: Dancing in autumn reduces the mass loss of a honeybee colony", *Journal of Experimental Biology*, vol. 215, no. 10, pp. 1633–1641, 2012.

[110] P. Ramdya, P. Lichocki, S. Cruchet, L. Frisch, W. Tse, D. Floreano, and R. Benton, "Mechanosensory interactions drive collective behaviour in Drosophila", *Nature*, vol. 519, no. 7542, pp. 233–236, 2015.

[111] J. Krause, A. F. Winfield, and J. L. Deneubourg, "Interactive robots in experimental biology", *Trends in Ecology and Evolution*, vol. 26, no. 7, pp. 369–375, 2011.

[112] K. Griparić, T. Haus, D. Miklić, M. Polić, and S. Bogdan, "A robotic system for researching social integration in honeybees", *PLoS ONE*, vol. 12, no. 8, pp. 1–17, 2017.

[113] T. Landgraf, H. Moballegh, and R. Rojas, "Design and development of a robotic bee for the analysis of honeybee dance communication", *Applied Bionics and Biomechanics*, vol. 5, no. 3, pp. 157–164, Dec. 2008.

[114] J. Halloy, G. Sempo, G. Caprari, C. Rivault, M. Asadpour, F. T??che, I. Sa??d, V. Durier, S. Canonge, J. M. Am??, C. Detrain, N. Correll, A. Martinoli, F. Mondada, R. Siegwart, and J. L. Deneubourg, "Social integration of robots into groups of cockroaches to control self-organized choices", *Science*, vol. 318, no. 5853, pp. 1155–1158, 2007.

[115] C. A. Penick and W. R. Tschinkel, "Thermoregulatory brood transport in the fire ant, Solenopsis invicta", *Insectes Sociaux*, vol. 55, no. 2, pp. 176–182, 2008.

[116] A. Weidenmüller, C. Mayr, C. J. Kleineidam, and F. Roces, "Preimaginal and Adult Experience Modulates the Thermal Response Behavior of Ants", *Current Biology*, vol. 19, no. 22, pp. 1897–1902, 2009.

[117] C. S. Oms, X. Cerdá, and R. Boulay, "Is phenotypic plasticity a key mechanism for responding to thermal stress in ants?", *Science of Nature*, vol. 104, no. 5-6, pp. 1–7, 2017.

[118] N. Stroeymeyt, B. Casillas-Pérez, and S. Cremer, "Organisational immunity in social insects", *Current Opinion in Insect Science*, vol. 5, no. 1, pp. 1–15, 2014.

[119] M. Salathe, M. Kazandjieva, J. W. Lee, P. Levis, M. W. Feldman, and J. H. Jones, "A high-resolution human contact network for infectious disease transmission", *Proceedings of the National Academy of Sciences*, vol. 107, no. 51, pp. 22 020–22 025, 2010.

[120] E. M. Volz, J. C. Miller, A. Galvani, and L. Meyers, "Effects of heterogeneous and clustered contact patterns on infectious disease dynamics", *PLoS Computational Biology*, vol. 7, no. 6, 2011.

[121] A. Dekker, "Network Centrality and Super-Spreaders in Infectious Disease Epidemiology", in *20th International Congress on Modelling and Simulation*, 2013, pp. 1–6.

[122] S. Pei and H. A. Makse, "Spreading dynamics in complex networks", *Journal of Statistical Mechanics: Theory and Experiment*, vol. 2013, no. 12, 2013.

[123] G. E. Leventhal, A. L. Hill, M. A. Nowak, and S. Bonhoeffer, "Evolution and emergence of infectious diseases in theoretical and real-world networks", *Nature Communications*, vol. 6, pp. 1–11, 2015.

[124] E. O. Wilson, *Success and Dominance in Ecosystems: The Case of the Social Insects*, ser. Excellence in ecology. Ecology Institute, 1990.

[125] J. .-L. Deneubourg, S. Aron, S. Goss, and J. M. Pasteels, "The self-organizing exploratory pattern of the argentine ant", *Journal of Insect Behavior*, vol. 3, no. 2, pp. 159–168, 1990.

[126] A. F. G. Bourke and N. R. Franks, *Social Evolution in Ants*. Princeton University Press, 2019.

[127] N. Pinter-Wollman, S. M. Fiore, and G. Theraulaz, "The impact of architecture on collective behaviour", *Nature Ecology and Evolution*, vol. 1, no. 5, 2017.

[128] M. Lehue and C. Detrain, "What's going on at the entrance? A characterisation of the social interface in ant nests", *Behavioural Processes*, vol. 160, no. December 2018, pp. 42–50, 2019.

[129] T. O. Richardson, T. Kay, R. Braunschweig, O. A. Journeau, M. Rüegg, S. McGregor, P. D. Los Rios, and L. Keller, "Ant behavioral maturation is mediated by a stochastic transition between two fundamental states", *Current Biology*, vol. 31, no. 10, pp. 2253–2260, 2021.

[130] M. Brian, *Social Insects. Ecology and Behavioural Biology*. Chapman and Hall, 1983.

[131] J. C. Cokendolpher and O. F. Francke, "Temperature Preferences of Four Species of Fire Ants (Hymenoptera: Formicidae: Solenopsis)", *Psyche*, vol. 92, p. 32 878, 1985.

[132] M. Ruchty, F. Helmchen, R. Wehner, and C. J. Kleineidam, "Representation of Thermal Information in the Antennal Lobe of Leaf-Cutting Ants", *Frontiers in Behavioral Neuroscience*, vol. 4, no. November, pp. 1–11, 2010.

[133] M. Nagel and C. J. Kleineidam, "Two cold-sensitive neurons within one sensillum code for different parameters of the thermal environment in the ant Camponotus rufipes", *Frontiers in Behavioral Neuroscience*, vol. 9, no. september, pp. 1–13, 2015.

[134] F. Roces and J. A. Núñez, "Brood translocation and circadian variation of temperature preference in the ant Camponotus mus.", eng, *Oecologia*, vol. 81, no. 1, pp. 33–37, Oct. 1989.

[135] Y. Heyman, Y. Vilk, and O. Feinerman, "Ants Use Multiple Spatial Memories and Chemical Pointers to Navigate Their Nest.", eng, *iScience*, vol. 14, pp. 264–276, Apr. 2019.

[136] N. Stroeymeyt, A. V. Grasse, A. Crespi, D. P. Mersch, S. Cremer, and L. Keller, "Social network plasticity decreases disease transmission in a eusocial insect", *Science*, vol. 362, no. 6417, pp. 941–945, 2018.

[137] M. Fiala, "Comparing ARTag and ARToolkit plus fiducial marker systems", *HAVE 2005: IEEE International Workshop on Haptic Audio Visual Environments and their Applications*, vol. 2005, pp. 148–153, 2005.

[138] J. F. Traniello, *Comparative foraging ecology of north temperate ants: The role of worker size and cooperative foraging in prey selection*, English, 1987.

[139] A. Bhatkar and W. H. Whitcomb, "Artificial Diet for Rearing Various Species of Ants", *The Florida Entomologist*, vol. 53, no. 4, pp. 229–232, Mar. 1970.

[140] Y. R. Lin, H. Sundaram, Y. Chi, S. Zhu, and B. L. Tseng, “Facetnet: A framework for analyzing communities and their evolutions in dynamic networks”, *Proceeding of the 17th International Conference on World Wide Web 2008, WWW’08*, pp. 685–694, 2008.

Curriculum Vitae

Fazil Emre Uslu

Lausanne, March 2022

Email: fazil.uslu@epfl.ch **Phone**: +41 78 697 84 12

Address: EPFL STI IGM MICROBS MED 3 2926 (Bâtiment MED) Station 9, CH-1015 Lausanne, Switzerland

Research interest
Microrobotics, self-organization, mechanobiology, finite element analyses, microengineering

Education

EPFL, École polytechnique fédérale de Lausanne — Lausanne, Switzerland
Ph.D. in Mechanical Engineering — May 2022
Advisor: Mahmut Selman Sakar

Koç University — Istanbul, Turkey
M.Sc. in Mechanical Engineering — January 2017
Advisor: Kerem Pekkan

Koç University — Istanbul, Turkey
B.Sc. in Physics — June 2015

Koç University — Istanbul, Turkey
B.Sc. in Mechanical Engineering — June 2015

Awards and Honors
Graduated as Second ranked student (B.Sc.) — June 2015
Ranked second in the graduating class of the Department of Mechanical Engineering in Koç University

Graduated as Top ranked student (B.Sc.) June 2015
Ranked first in the graduating class of the Department of Physics in Koç University

Undergraduate Scholarship 2010-2015
Accepted to Koç University with a full-merit undergraduate scholarship due to the high ranking score on the nationwide University Entrance Examination (ranked 1752 among approximately 1.7 million students)

Journal Papers

Uslu F.E., Davidson C.D., Mailand E., Bouklas N., Baker B.M., Sakar M.S., "Engineered Extracellular Matrices with Integrated Wireless Microactuators to Study Mechanobiology", *Advanced Materials* , 2021.

Huang H.W., **Uslu F. E.**, Katsamba P., Lauga E., Sakar M.S., Nelson B.J., "Adaptive locomotion of artificial microswimmers", *Science Advances* , 2019.

Reiten I., **Uslu F. E.**, Fore S., Pelgrims R., Ringers C., Verdugo C. D., Hoffman M., Kawakami K., Pekkan K., Yaksi E., Jurisch-Yaksi N., "Motile cilia mediated flow improves sensitivity and temporal resolution of olfactory computations", *Current Biology* , 2017.

Uslu F. E., Pekkan K., "Mytilus Galloprovincialis as a Smart Micro-Pump", *Biology Open* , 2016.

Goktas S., **Uslu F. E.**, Kowalski W., Ermek E., Bradley B.K., Pekkan K., "Time-Series Interactions of Gene Expression, Vascular Growth and Hemodynamics during Early Embryonic Arterial Development", *PlosONE* , 2016.

Pekkan K., Chang B., **Uslu F. E.**, Mani K., Chen C.Y., Holzman R., "Characterization of Zebrafish Larvae Suction Feeding Flow Using Micro-PIV and Optical Coherence Tomography", *Experiments in Fluids* , 2016.

Conference Abstracts

Uslu F. E.*, Davidson C.D., Mailand E., Bouklas N., Baker B.M., Sakar M.S., "Wireless micro actuators to apply spatiotemporally controlled mechanical forces to cells on engineered fiber network", International Meeting of German Society for Cell Biology – Life in between, The cell biology of interfaces, Munster, Germany, September 27-29, 2021 (Oral Presentation)

Uslu F. E.*, Davidson C.D., Bouklas N., Baker B.M., Sakar M.S., "Actuated Fibre Networks to Study Physical Principles of Multicellular Organization", American Physical Society (APS) March Meeting 2019, Boston, USA, March 4-8, 2019 (Oral Presentation)

Uslu F. E.*, McGregor S., Keller L., Sakar M.S., "Directed Self-Organisation through Thermoregulation in Ant Colonies", American Physical Society (APS) March Meeting 2019, Boston, USA, March 4-8, 2019 (Poster Presentation)

Uslu F. E., Pekkan K.*, " Flow Dynamics of A Smart Pump: Mytilus Galloprovincialis", American Physical Society (APS) Division of Fluid Dynamics (DFD) 2016, Portland, USA, November 20-22,

2016 (Oral Presentation)

Seyedehsamaneh L., Piskin S., Goktas S., **Uslu F. E.**, Pekkan K.*, "Microstructural Analysis of Early Embryonic Aortic Arch Morphogenesis", Summer Biomechanics, Bioengineering, and Biotransport Conference, Microstructural Analysis of Early Embryonic Maryland, USA, June 29-July 2, 2016 (Oral Presentation)

Uslu F. E.*, Goktas S., Kowalski W., Bradley B.K., Pekkan K., "Characterization of Pulsatile Wall Shear Stress at the Vitelline Artery During Early Embryonic Development" , 11th International Symposium on Particle Image Velocimetry – PIV 2015, Santa Barbara, USA, September 14-16, 2015 (Oral Presentation)

Chen C.Y., **Uslu F. E.***, Pekkan K.*, " Three-dimensional Characterization of Fluid Flows Induced by Micro- Objects in Microfluidics" , 10th International Symposium on Particle Image Velocimetry – PIV 2013, Delft, The Netherlands, July 1-3, 2013 (Poster Presentation)

(* presented by)

Research experience

Graduate Research Assistant at MicroBioRobotic Systems Laboratory, EPFL
Advisor: Professor Mahmut Selman Sakar February 2017 – Present

Development of micro-robotic platform with a micro-actuator to apply mechanical signals to fibrous material:

- Devising methodologies of the micro manufacturing of the micro-actuator and integration on the fibrous material
- Designing and manufacturing robotic magnetic actuation system
- Developing image processing software tools to construct digital twin of fibrous material and finite element model to recapitulate the mechanical stresses on the material applied by the micro-actuator
- Developing image processing software tools to construct digital twin of fibrous material and finite element model to recapitulate the mechanical stresses on the material applied by the micro-actuator
- Characterization of the applied forces on the fibrous material
- Incorporating the biological cells onto the micro-robotic platform which required cell culture practice

Development of robotic device to generate independently regulated temperature zones on a nest floor:

- Design and manufacturing of aluminum chassis, consisting of 60 peltier elements for temperature regulating and embedded water channels to absorb heat from the peltier elements

- Optimization of cooling liquid channels via computational fluid dynamics modelling
- Designing electronic circuit board to control 60 peltier elements
- Integration/assembly of a water temperature regulator and pump to the main chassis

Modelling of a flexible hydrogel filament of a microrobot inspired from bacteria

Graduate research assistant at Biological and Cardiovascular Fluid Mechanics Laboratory
Advisor: Professor Kerem Pekkan 2012 – 2017

- Studying biological flows (cardiovascular flows, suction feeding, olfaction) by PIV (Particle Image Velocimetry)
- Conducting micro-PIV experiments for investigating fluid mechanics patterns on biological microfluidics

Undergraduate research assistant at Advanced Materials Laboratory
Advisor: Professor Demircan Canadinç 2010 – 2012

- Assisting material behavior experiments on the shape memory alloys in micro scales

Industry experience

Part-time RD Engineer
Baykar Defense Aviation Company, Istanbul, Turkey Sep 2014 - Jan 2015
Computational Fluid Dynamics (CFD) Analyst for aerodynamics analyses of Tactical UAV.

Summer Intern
Baykar Defense Aviation Company, Istanbul, Turkey Jun 2014 - Sep 2014
Worked for modeling of engine parameters for simulator of Tactical UAV.

Summer Intern
OTOKAR Automotive and Defense Industry, Sakarya, Turkey July 2013 - Aug 2013
Worked at manufacturing line of armored vehicles and buses.

Certificates and Trainings

- Cellular Imaging Techniques Workshop (24-29 April 2016) organized by IBG-Izmir and University of Oxford, Izmir, Turkey
- LaVision PIV Seminar (3-7 November 2015), Gottingen, Germany

Teaching experience

Graduate teaching assistant at École polytechnique fédérale de Lausannenne (EPFL)
ME-221 (Dynamical Systems) in Spring 2020 and Spring 20211
ME-412 (Experimental Methods in Engineering Mechanics) in Fall 2019
ME-475 (Multi-body simulation) in Spring 2017 and Spring 2018
Bachelor thesis project mentor in Spring 2017, Spring 2018 and Spring 2019

Undergraduate student tutor at KOLT (Koç University Office of Learning and Teaching) Center, Koç University
MECH 100 (Introduction to Mechanical Engineering) and MATH 204 (Differential Equations) in Spring 2015
MECH 201 (Statics and Mechanics of Materials) and MATH 204 in Fall 2014
MECH 100 in Spring 2014
MECH 201 and MATH 204 in Fall 2013

Skills

Design: Siemens NX, SolidWorks, Catia, AutoCAD
Software: Java, C++, Python, MATLAB
Modelling: Abaqus FEA, Ansys, Comsol Multiphysics
Organization/Presentation: Adobe Illustrator, MS office
Language Skills: Turkish (Native), English (Fluent), French (B1/B2)